Cell

Modulation of FGF pathway signaling and vascular differentiation using designed oligomeric assemblies

Graphical abstract

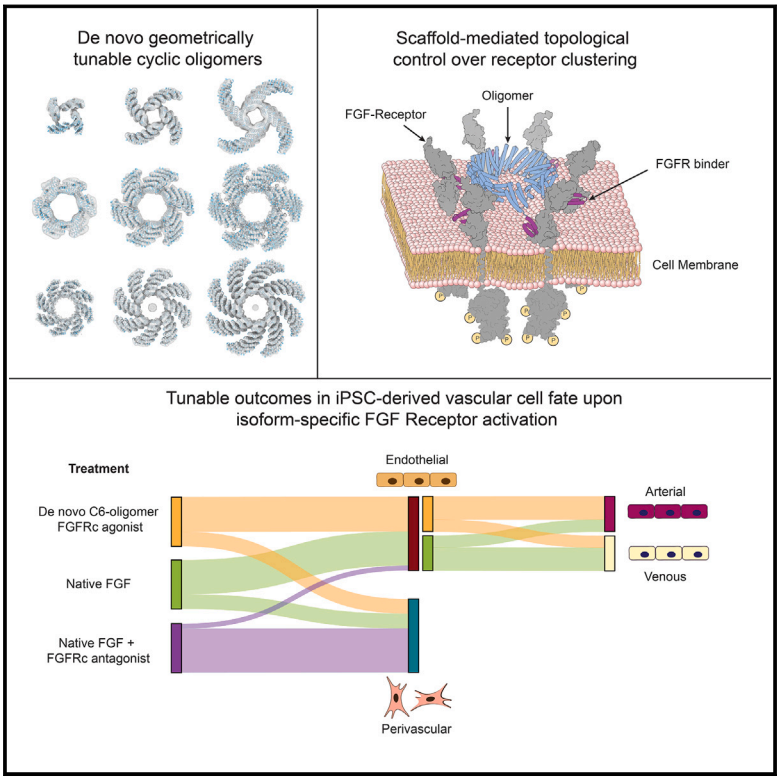

Highlights

- *De novo* designed cyclic oligomers with tunable geometric properties
- Oligomeric FGFR-binding modules induce geometry- and valency-dependent signaling
- Modulation of FGFR isoform activity controls cell fate during vascular development
- FGFR c-isoform activation favors arterial fate, while b-isoform favors perivascular fate

Authors

Natasha I. Edman, Ashish Phal, Rachel L. Redler, ..., Gira Bhabha, Hannele Ruohola-Baker, David Baker

Correspondence

hannele@uw.edu (H.R.-B.), dabaker@uw.edu (D.B.)

In brief

De novo designed synthetic agonists against the c-isoform of the FGF receptor are used to specifically control cellular fate in a vascular endothelial cell differentiation model.

Edman et al., 2024, Cell *187*, 3726–3740
July 11, 2024
https://doi.org/10.1016/j.cell.2024.05.025

CellPress

CellPress
OPEN ACCESS

Cell

Article

Modulation of FGF pathway signaling and vascular differentiation using designed oligomeric assemblies

Natasha I. Edman,[1,2,3,4,20] Ashish Phal,[5,6,20] Rachel L. Redler,[7,20] Thomas Schlichthaerle,[1,2,20] Sanjay R. Srivatsan,[2,4,8] Devon Duron Ehnes,[1,5] Ali Etemadi,[1,2,9] Seong J. An,[10] Andrew Favor,[1,2] Zhe Li,[1,2] Florian Praetorius,[1,2] Max Gordon,[1,5] Thomas Vincent,[5,6,11] Silvia Marchiano,[5] Leslie Blakely,[5] Chuwei Lin,[8] Wei Yang,[1,2] Brian Coventry,[1,2] Derrick R. Hicks,[1,2] Longxing Cao,[1,2] Neville Bethel,[1,2,12] Piper Heine,[1,2] Analisa Murray,[1,2] Stacey Gerben,[1,2] Lauren Carter,[1,2] Marcos Miranda,[1,2] Babak Negahdari,[9] Sangwon Lee,[10] Cole Trapnell,[8,13,14] Ying Zheng,[5,6,15] Charles E. Murry,[5,6,15,16,17] Devin K. Schweppe,[8] Benjamin S. Freedman,[5,6,11,13,16,18] Lance Stewart,[1,2] Damian C. Ekiert,[7,19] Joseph Schlessinger,[10] Jay Shendure,[8,12,13,14] Gira Bhabha,[7] Hannele Ruohola-Baker,[1,5,6,8,21,*] and David Baker[1,2,12,*]

[1]Department of Biochemistry, University of Washington, Seattle, WA 98195, USA
[2]Institute for Protein Design, University of Washington, Seattle, WA 98195, USA
[3]Molecular and Cellular Biology Graduate Program, University of Washington, Seattle, WA 98195, USA
[4]Medical Scientist Training Program, University of Washington, Seattle, WA 98195, USA
[5]Institute for Stem Cell and Regenerative Medicine, University of Washington, Seattle, WA 98109, USA
[6]Department of Bioengineering, University of Washington, Seattle, WA 98195, USA
[7]Department of Cell Biology, New York University School of Medicine, New York, NY 10016, USA
[8]Department of Genome Sciences, University of Washington, Seattle, WA 98195, USA
[9]Medical Biotechnology Department, School of Advanced Technologies in Medicine, Tehran University of Medical Sciences (TUMS), Tehran, Iran
[10]Department of Pharmacology, Yale University School of Medicine, New Haven, CT 06520, USA
[11]Division of Nephrology, Department of Medicine, University of Washington School of Medicine, Seattle, WA 98109, USA
[12]Howard Hughes Medical Institute, University of Washington, Seattle, WA 98195, USA
[13]Brotman Baty Institute for Precision Medicine, Seattle, WA 98195, USA
[14]Allen Discovery Center for Cell Lineage Tracing, Seattle, WA 98109, USA
[15]Center for Cardiovascular Biology, University of Washington, Seattle WA 98109, USA
[16]Department of Laboratory Medicine and Pathology, University of Washington, Seattle, WA 98195, USA
[17]Department of Medicine/Cardiology, University of Washington, Seattle WA 98195, USA
[18]Kidney Research Institute, University of Washington School of Medicine, Seattle, WA 98109, USA
[19]Department of Microbiology, New York University School of Medicine, New York, NY 10016, USA
[20]These authors contributed equally
[21]Lead contact
*Correspondence: hannele@uw.edu (H.R.-B.), dabaker@uw.edu (D.B.)
https://doi.org/10.1016/j.cell.2024.05.025

SUMMARY

Many growth factors and cytokines signal by binding to the extracellular domains of their receptors and driving association and transphosphorylation of the receptor intracellular tyrosine kinase domains, initiating downstream signaling cascades. To enable systematic exploration of how receptor valency and geometry affect signaling outcomes, we designed cyclic homo-oligomers with up to 8 subunits using repeat protein building blocks that can be modularly extended. By incorporating a *de novo*-designed fibroblast growth factor receptor (FGFR)-binding module into these scaffolds, we generated a series of synthetic signaling ligands that exhibit potent valency- and geometry-dependent Ca^{2+} release and mitogen-activated protein kinase (MAPK) pathway activation. The high specificity of the designed agonists reveals distinct roles for two FGFR splice variants in driving arterial endothelium and perivascular cell fates during early vascular development. Our designed modular assemblies should be broadly useful for unraveling the complexities of signaling in key developmental transitions and for developing future therapeutic applications.

INTRODUCTION

Clustering of cell surface receptors can enhance and sustain activation in response to an extracellular signal, and there is considerable interest in technologies to manipulate receptor clustering.[1–6] Designed protein assemblies have previously been used to drive receptor clustering using naturally occurring receptor-binding domains,[7–9] and geometrically tunable dimeric

ligands have been used to probe the influence of dimerization geometry on signaling output.[10–13] Higher-order receptor assemblies are thought to function in a variety of signaling systems[14–16]; a tunable oligomeric scaffold presenting receptor-binding domains would facilitate studies into the effect of angstrom-level topology on receptor output. Previous design efforts have generated oligomers with a variety of cyclic symmetries,[17–20] but these proteins were not easily modifiable to produce distinct receptor-binding configurations.

Fibroblast growth factor (FGF) receptors (FGFRs) are tyrosine kinases that play critical roles in embryonic development and cancer. The pathway is complex and highly regulated, with four FGF receptor genes and two isoforms generated by alternative splicing of exon 8 vs. exon 9, which alter the third immunoglobulin (Ig)-like domain (D3), generating receptor isoforms IIIb and IIIc (referred to as "b" and "c," respectively, throughout the text).[21–23] Although D3 is part of the FGF-binding region, and the receptor isoforms have different affinities for the various FGF ligands, the contribution of the two isoforms to proper tissue differentiation is not fully understood.[24] The c-isoform is amplified in many solid carcinomas and hence may be a target for cancer therapy.[22]

Here, we describe the *de novo* design of geometrically tunable cyclic oligomers to overcome the limitations of current scaffolding systems and the use of these synthetic scaffolds with an FGFR c-isoform-specific-designed minibinder[21] to probe and manipulate vascular differentiation.

RESULTS

De novo oligomer design

Cyclic oligomers (Cx, with "x" denoting valency) were designed using a set of 18 designed helical repeat proteins (DHRs), each consisting of four identical repeats of a two-helix module and with high-resolution crystal structures or small-angle X-ray (SAXS)[25,26] spectra consistent with the corresponding design models (Table S1; Figure S1A). We docked each DHR into C4, C5, C6, C7, and C8 cyclic oligomeric assemblies and evaluated them using the protein-backbone-based residue-pair transform (RPX) metric, which assesses interface designability (Figure S1B).[20,27] For the top-scoring docks, the residue identities and conformations at the homo-oligomeric interface were optimized using RosettaDesign to favor oligomer assembly. We filtered for designs with a high solvent-accessible surface area (SASA > 700 Å^2), favorable free energies of assembly ($\Delta\Delta G$ between −35 and −70), high shape complementarity (sc > 0.65), and interfaces with fewer than 2 unsatisfied hydrogen bonds.[28,29] A total of 109 designs were selected for structural characterization: 15 tetramers, 16 pentamers, 24 hexamers, 24 heptamers, and 30 octamers. A second set of designs using a computational library of 1,526 5-helix concave scaffolds (5HCS)[30,31] were docked with C2 symmetry, and from 3,747 C2 oligomers, 14 designs were selected for further analysis (Figure S1C).

Design characterization

Synthetic genes encoding the 109 designs of symmetry C4 or higher were synthesized, expressed as protein in *Escherichia coli*, and purified using immobilized metal affinity chromatography (IMAC). Of the 60 designs that were soluble, 28 had single monodisperse peaks on size exclusion chromatography (SEC). Of these, ten designs were found to have a single oligomeric state by both SAXS[32–34] and SEC with multi-angle light scattering (SEC-MALS). Five of the successes were tetramers, four were hexamers, and one was an octamer. From the 14 C2 designs, 3 (C2-58, C2-CDX, and C2-Y2D) had soluble expression, were confirmed to have a monodisperse peak on SEC, and had a correctly assembled oligomeric state verified by SAXS and SEC-MALS (Figure S2; Table S2).

The varied topology of the repeat protein building blocks enabled us to create oligomers with distinct arm orientations. The starting scaffold DHR71 generated 5 successful designs (C4-71, C4-717, C6-71, C6-714, and C8-71), with a variety of interface geometries that permitted this building block to assume 3 distinct valencies. C4-71 and C4-717, for example, contain changes in different sets of residues that result in distinct oligomer geometries. In contrast, the designs C4-71, C6-71, and C8-71 employ a similar backbone region as the oligomeric interface, yet adopt different oligomeric states (Figure S3). C4-181 utilizes DHR18 as the single-chain building block and is docked together at the C-terminal helices, yielding an inner cavity diameter of 45.6 Å (C-terminal distance of opposing chains, Figure 1A). C4-717 is tightly docked together at the C-terminal helices, creating a purely hydrophobic core between all four chains (Figure 1B). C6-714 has an inner cavity diameter of 43.2 Å and its N terminus can be extended to achieve larger distance spacing, whereas the structure is again docked together at the C terminus (Figure 1C). C6-46 involves the carboxyl (C)- and amino (N)-terminal helices at the interfaces to adjacent chains, where the N terminus points toward the central cavity and the C terminus toward the outside (Figure 1D). The designed residue substitutions that generate the oligomeric assemblies from the original DHR building blocks are listed in Table S3. Six designs were further selected for characterization by cryoelectron microscopy (cryo-EM) (Tables S4 and S5). The cryo-EM map for windmill-shaped C4-131 was limited to >10 Å global resolution due to preferred orientation bias, but shows that the "blades" are arranged as designed and that the four core C-terminal helices are tightly packed (Figure 1E). The higher resolution for design C4-81 allows individual helices to be clearly distinguished, and following rigid-body fitting using ChimeraX, the design model closely matched the cryo-EM map (Figure 1F). For C6-79, a C6-docked assembly matched the SAXS data more closely than the original C8 assembly as well as the cryo-EM map, and the 2D classes clearly indicate that it is a hexamer under our cryo-EM conditions (Figure 1G).

Oligomer extension

An advantage of using modular repeat proteins as building blocks is that the length of the oligomer arms can be increased or decreased simply by inserting or deleting repeat units (Figure 2A).[10,20,25] To explore the viability of this approach, three designs (C4-71, C6-71, and C8-71) derived from DHR71 were selected for repeat extension. Two or four repeat units were added at the N terminus, creating a 6-repeat variant and an 8-repeat variant of each design. The oligomeric state of each

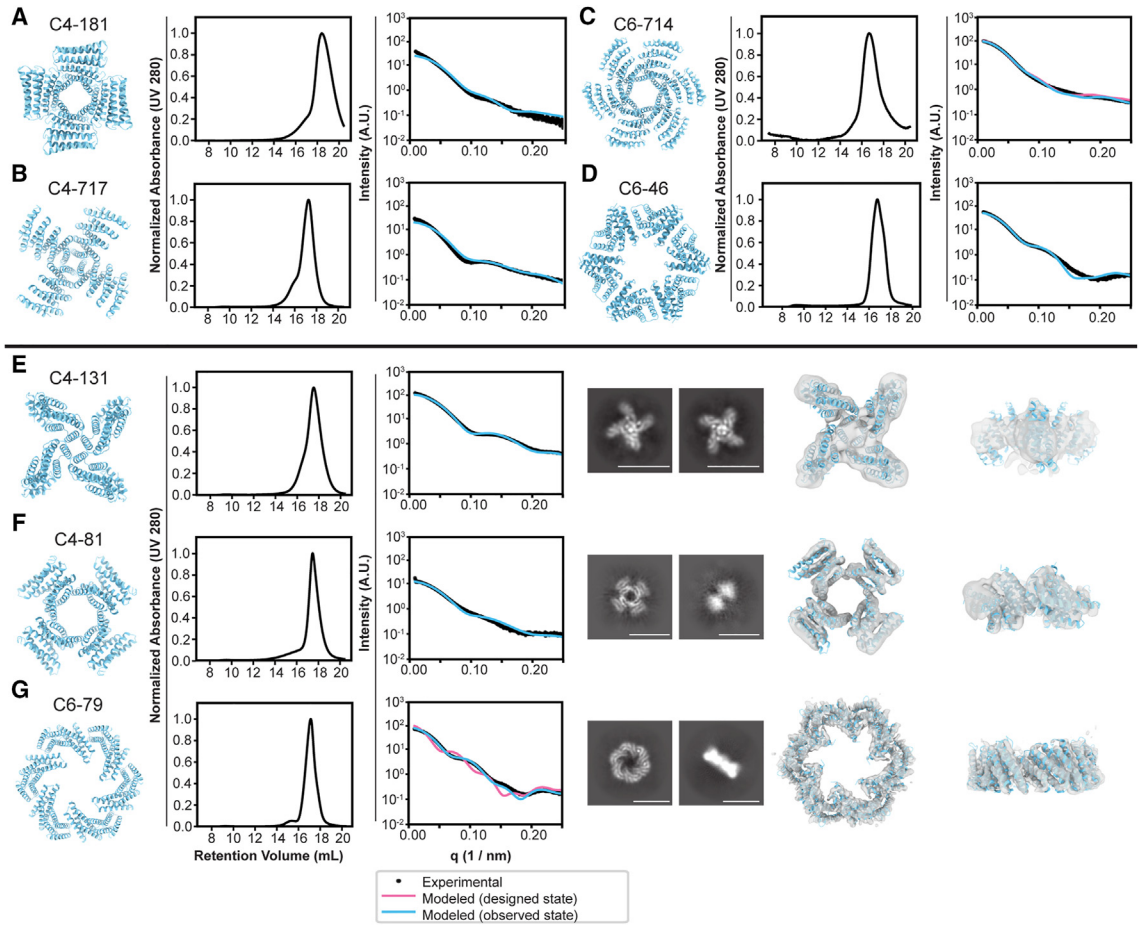

Figure 1. Biophysical characterization of designed protein oligomers

From left to right: design model, size-exclusion chromatogram, and SAXS data comparison of model to experimental data (A) C4-181, (B) C4-717, (C) C6-714, (D) C6-46, and (E) C4-131 design model, size-exclusion chromatogram, and SAXS data analysis; right: cryo-EM 2D class average, cryo-EM map (EMDB: EMD-28958) overlay to design model (cyan) top and side view (F) C4-81 design model, size-exclusion chromatogram, SAXS data analysis; right: cryo-EM 2D class average, cryo-EM map (EMDB: EMD-28973) superimposed to design model (cyan) top and side view (G) C6-79 SEC characterization and SAXS fit using both the C8 design model and the C6 dock. Right: cryo-EM 2D class average, cryo-EM map (EMDB: EMD-28889) superimposed to design model top and side view. Scale bars: 10 nm in (E)–(G).

See also Figures S1, S2, and S5 and Tables S1–S5.

extended design was characterized by SEC-MALS, SAXS, and cryo-EM. Both 2D classes and 3D reconstructions from single-particle cryo-EM analysis of the extended oligomers show overall geometry in good agreement with design models, with sufficiently high resolution in some cases to confirm positions of individual helices. The C-terminal helix of C4-71 docked as designed against the mid-axis of the neighboring chain horizontally, yielding a distance of 47.4 Å between opposing-chain C termini across the inner cavity (Figure 2B; the interface harbors 10 tryptophans, which make pi-pi stacking interactions stabilizing the assembly). C6-71, in contrast, has an inner diameter of 72.0 Å between opposing-chain C termini and harbors a tilted chain-chain interaction, where the interfacial C-terminal helix is only in contact with the neighboring chain along half its length. Side-chain orientations can be discerned in the C6-71 8-repeat extension map despite the low number of total particles used in constructing this map (Figure 2C). The octopus-like C8-71 structure has N-terminal extensible arms with C-terminal helices of the individual chains docked together along the full horizontal length of the structure, resulting in an inner diameter of 55.1 Å and a maximal distance between opposing N termini of 170.0 Å in the largest 8-repeat extension (Figure 2D).

All cryo-EM maps were in good agreement with the respective design models, with the exception of C6-79, which, as noted above, formed a hexamer instead of the designed octamer. None of the other designs showed any off-target oligomeric states in the 2D class averages (Figures S4–S8).

Cryo-EM reconstructions of C6-79 and C8-71

Based on the resolution of the cryo-EM maps, we built models for C6-79 and C8-71 (Figures S9–S11; Table S6). Both the C6-79 and C8-71 cryo-EM models align well with the corresponding design models, with pairwise root-mean-square deviations (RMSDs) of 2.85 and 1.79 Å, respectively (Figure 3).

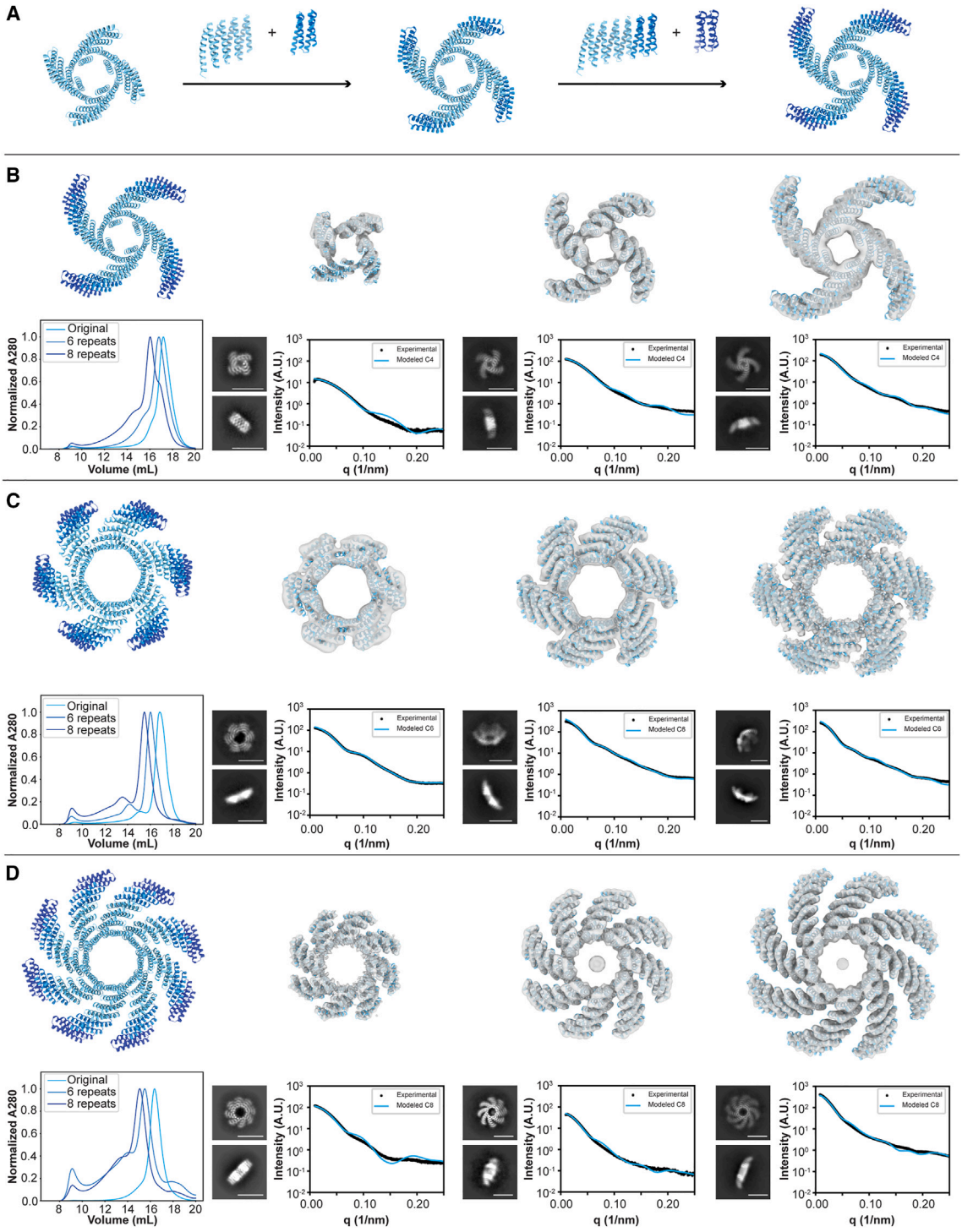

Figure 2. Modulating oligomer geometry by repeat extension

(A) Depiction of DHR-based repeat extension for oligomers. Each extension unit consists of 2 repeats.

(B) C4-71 4-repeat (EMDB: EMD-28974), 6-repeat (EMDB: EMD-28966), and 8-repeat (EMDB: EMD-28967) cryo-EM maps superimposed with design model, top and side-view class averages and SAXS characterization below the cryo-EM maps of the different repeat extension variants. Bottom left: SEC overlay of the individual structures.

(C) C6-71 4-repeat (EMDB: EMD-28968), 6-repeat (EMDB: EMD-28969, and 8-repeat (EMDB: EMD-28970) cryo-EM maps superimposed with design model, top and side-view class averages and SAXS characterization below the cryo-EM maps of the different repeat extension variants. Bottom left: SEC overlay of the individual structures.

(legend continued on next page)

In C8-71, the hydrophobic residues Trp152 and Leu198 on the adjacent chain are buried in the interface or the core of the structure, respectively, and are important for interface formation (Figure S12A). Mutating these residues to hydrophilic residues (W152E and/or L198D) disrupts oligomer formation, as shown by broadening of the SEC trace (Figure S12B).

Design of FGFR agonists

We next investigated whether clustering receptor tyrosine kinases in higher-order geometries by presenting receptor-binding domains on the designed oligomers could drive cross-phosphorylation of their intracellular kinase domains and induce downstream signaling.[35] The multiple distinct valencies and geometries of our oligomeric ligands enable exploration of how the geometry and valency of tyrosine kinase receptor association influence signaling output and cell behavior (Figure 4A, left). We chose as a model system the FGF signaling pathway (Figure 4A, right) and fused a *de novo*-designed minibinder (mb7) against FGFRc (PDB: 7N1J) at either the N or C termini of the designed cyclic oligomers with a short glycine-serine linker.[36] Six oligomers were selected for fusion: C2-58, C4-71, C6-71, C6-79, and C8-71. Depending on the fusion terminus and the geometry of the oligomer, the binding domains are displayed at different spacings on adjacent subunits: for example, C6-79C_mb7 displays the minibinders 54 Å apart with mb7 on the C terminus of the oligomer, while C6-79N_mb7 displays the binders 18 Å apart with mb7 on the N terminus of the oligomer. In SEC experiments, the fusions eluted at the same volume as the base oligomers, with the exception of C6-71C_mb7, which eluted significantly earlier than the base design. 2D EM class averages showed that C6-71C_mb7 particles were self-associating into dihedral structures, presumably via the hydrophobic interface of the minibinder domain being presented in a favorable conformation for this interaction. The other oligomeric fusions showed little to no self-association on EM or SEC (Figure S13).

FGFR pathway activation

FGF-mediated FGFR signaling results in stimulation of the Ras signaling pathway, leading to phosphorylation of extracellular-signal-regulated kinase 1 and 2 (ERK1/2) and activation of phospholipase C-gamma (PLC-ɣ), leading to intracellular calcium release.[24,37,38] We evaluated the signaling activity of our designs by screening them in serum-starved Chinese hamster ovary (CHO) cells stably expressing hFGFR1c (CHO-R1c) at 10 nM each for 15 min at 37°C. Downstream activation through phosphorylation of ERK1/2 and FGFR1 (Y653/654) was analyzed by western blot. Of the designs, we found that C6-79C_mb7, C6-79N_mb7, C4-71N_mb7, C4-71C_mb7, and C8-71C_mb7 broadly induced strong FGFR activation and ERK1/2 phosphorylation, comparable to that achieved by native FGF2, while C2-58-2X_mb7, C6-71C_mb7, C6-71N_mb7, and C8-71N_mb7 displayed weaker activity (Figures 4B and S14).

To characterize their dose-dependent activity, we titrated a subset of these designs using phosphoflow[39] and western blotting for ERK1/2 phosphorylation in CHO-R1c cells (Figures 4C and S15). C2-58-2X_mb7, C4-71C_mb7, C4-71N_mb7, C6-79C_mb7, and C8-71C_mb7 had similar EC_{50} values of 0.63, 1.33, 0.89, 1.56, and 2.07 nM, respectively, and similar maximal activation (E_{max}) values, while C2-58-2X_mb7 had a lower E_{max}. To investigate how the geometry of receptor association influences signaling, the rigid repeat arm length of C4-71N_mb7 was systematically varied, leading to distances between mb7 N termini of 53, 76, and 96 Å. Phosphoflow experiments showed that only the shortest separation distance (53 Å) was able to stimulate ERK phosphorylation (with an EC_{50} of 1.3 nM), whereas the larger separation distances of mb7 did not lead to pathway activation (Figure S16).

Receptor clustering on the cell surface

To investigate whether FGFR1c activation was due to induced receptor clustering, cells were examined by single-particle tracking with a HaloTag targeting FGFR1c[40] to directly visualize their diffusion in the plasma membrane; receptors engaged in a signaling cluster should exhibit decreased diffusion, manifesting in a decreased diffusion coefficient.[41] Receptors on cells treated with C6-79C_mb7 showed slower diffusion than those treated with FGF1 and heparin (Figure S17), indicating that C6-79C_mb7 induces an oligomeric state of FGFR1c at the membrane. To probe the presence of local receptor clusters on the cell surface after ligand treatment, intensity levels of single spots in HaloTagged CHO-R1c cells labeled with Alexa488 were evaluated.[42] C6-79C_mb7-treated cells showed signals with an intensity distribution slightly shifted compared with FGF1 supplemented with heparin, with intensity peaks at 500, 1,000, and 2,000 a.u., suggesting that multiple receptors are clustered together by the designed mb7-presenting oligomers. The extent of signaling correlated with the ability of the designs to cluster receptors (Figures 4D and 4E).

FGFR1c isoform specificity

FGFRs 1–3 have two alternatively spliced variants, the "c" and "b" isoforms, which have different third Ig-like domains and variable FGF ligand affinities.[43] Tissue-specific expression of these isoforms and their reciprocal signaling play roles in embryonic development, tissue repair, and cancer.[22] Separating the functions of the FGFR b- and c-isoforms in differentiation has been hindered by a lack of ligands that can selectively bind one isoform or the other. The mb7 minibinder was designed to specifically bind the c-isoform of the FGFR, and it selectively inhibits signaling through this isoform.[21] We evaluated the receptor isoform specificity of our synthetic agonists by treating serum-starved L6 rat myoblast cells stably expressing either the c- or b-isoform of hFGFR1 (L6-R1c or L6-R1b, respectively; overexpression was validated with RT-qPCR [Figure S18]) with 10 nM

(D) C8-71 4-repeat (EMDB: EMD-28888), 6-repeat (EMDB: EMD-28971), and 8-repeat (EMDB: EMD-28972) cryo-EM maps superimposed with design model, top and side-view class averages and SAXS characterization below the cryo-EM maps of the different repeat extension variants. Bottom left: SEC overlay of the individual structures. Scale bars: 10 nm in (B)–(D).
See also Figures S3, S4, and S6–S8 and Tables S2–S5.

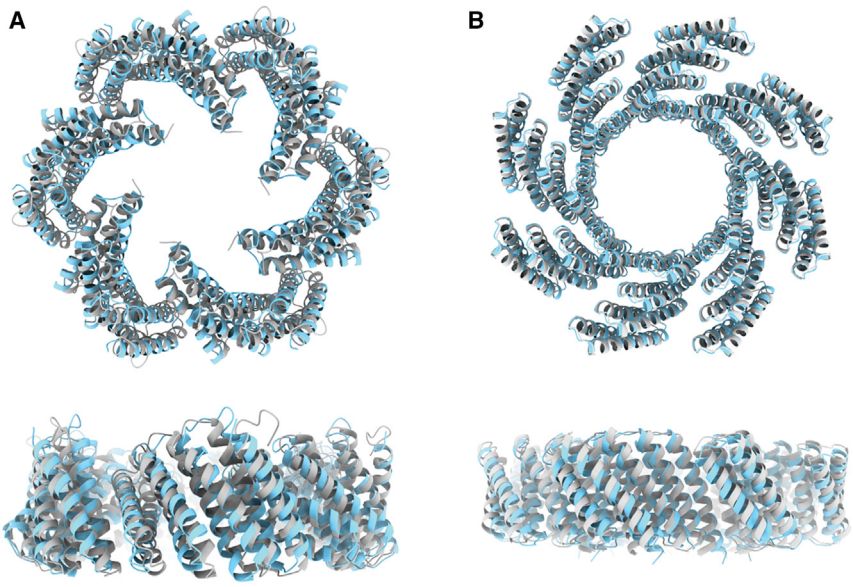

Figure 3. Cryo-EM structural analysis

(A) C6-79 alignment of design model (gray) with cryo-EM structure (cyan, PDB: 8F6R) in top and side view. Structures align well with an RMSD of 2.85 Å (B) C8-71 alignment of design model (gray) with cryo-EM structure (cyan, PDB: 8F6Q) in top and side view. Structures are in good agreement with an RMSD of 1.79 Å.

See also Figures S9–S12 and Tables S4–S6.

of mb7, FGF2, or C6-79C_mb7 for 15 min at 37°C. Although FGF2 does not discriminate between the two FGFR1 isoforms and activates signaling in both cell types, C6-79C_mb7 stimulates ERK1/2 and FGFR phosphorylation only in L6-R1c cells. We reasoned that it should be possible to specifically activate signaling through the b-isoform by combining FGF2 with the monomeric mb7 (which blocks signaling through the c-isoform); to test this, we stimulated both L6 cell lines with a combination of mb7 and FGF2 at 10 nM each for 15 min. We found that this combination stimulates ERK1/2 phosphorylation in L6-R1b cells only; thus, our designs enable selective activation of signaling through either isoform (Figure 4F).

We next investigated the ability of the designs to activate FGF signaling through the PLC-ɣ downstream branch of signaling by measuring the levels of intracellular calcium release following treatment of serum-starved CHO-R1c cells with varying concentrations of the designs. These results show a similar trend: C6-79C_mb7, C4-71C_mb7, and C8-71C_mb7 induce strong intracellular calcium release, with EC_{50} values of 0.38, 0.72, and 3.09, respectively, while C2-58-2X_mb7 displays lower activity, with an EC_{50} of 26.02 nM (Figures 4G and S19). Although the peak magnitude of calcium release was similar between FGF2 at 10 nM and the synthetic agonist C6-79C_mb7 at 10 nM, there was a pronounced difference in the duration of the response: the higher valency synthetic ligand, C6-79C_mb7, generated longer-duration calcium transients (Figure 4H), similar to a control condition in which we supplemented FGF2 together with heparin. This strong, heparin-independent signaling effect (Figure S20) of our designed agonist likely reflects the slow off rates of the high avidity multivalent agonists (Figure S21). To compare the effects of the agonist C6-79C_mb7 and FGF2 on the whole proteome, we carried out a (phospho-)proteomic analysis using mass spectrometry following treatment of FGFR1c-expressing CHO cells and found very similar changes in the overall proteome and in phosphopeptide abundance (Figure S22).

Sculpting vascular differentiation with the designed agonists

FGF signaling plays an important role during early embryogenesis[44,45]; the controlled spatiotemporal expression of FGFRs and their ligands drives specification and development of many cell lineages.[46–48] In the vasculature, mesodermal precursors give rise to endothelial and perivascular cell fates. The role of FGF signaling and the FGFR isoforms in this bifurcation is not currently understood.

We investigated the effect of the c-isoform-specific FGFR minibinder oligomers on vascular development by generating endothelial cells and perivascular cells from human induced pluripotent stem cells (iPSCs) through a cardiogenic mesoderm intermediate (Figure S23A).[49] We replaced the ~1 nM FGF2 (which engages both b- and c-isoforms of FGFRs[50]) in a previously described differentiation media between days 2 and 5 (when mesodermal intermediates first appear) in the protocol with 1 nM C6-79C_mb7 (the most potent synthetic agonist), 100 nM C2-58-2X_mb7 (the weakest agonist), 10 nM mb7, or 10 nM mb7, in combination with 1 nM FGF2 (to specifically activate signaling through the b-isoform), and from day 5 onward allowed the cells to differentiate in normal conditions for 28 days; samples were harvested for single-cell RNA sequencing (scRNA-seq) analysis at days 0, 5, 14, and 28. The sequencing datasets were analyzed using Monocle3[51] and visualized using uniform manifold approximation and projection (UMAP), which revealed 5 clusters of cells that segregated predominantly by time point and cell type (Figure 5A); cell types were annotated based on the differential expression of previously published canonical marker genes (Figure S23B).

Endothelial versus perivascular fate specification

All treatments (FGF2 and designed agonists) directed iPSCs to differentiate and form a common endothelial-perivascular precursor at day 5. This common precursor population then bifurcated to form either endothelial cells or perivascular cells at day 14. The cellular differentiation trajectory was design-dependent and determined by day 14. Addition of FGF2, C6-79C_mb7, or C2-58-2X_mb7 generated ~60% endothelial cells in all three cases; the remaining population differentiated into perivascular cells. In contrast, the differentiation media without any FGF addition (control) resulted in a population that was only ~34% endothelial (endothelial cell formation is weakly driven in the absence of any supplemented FGF2, presumably because of low levels of endogenously secreted FGFs; Figure S23C). On the other end

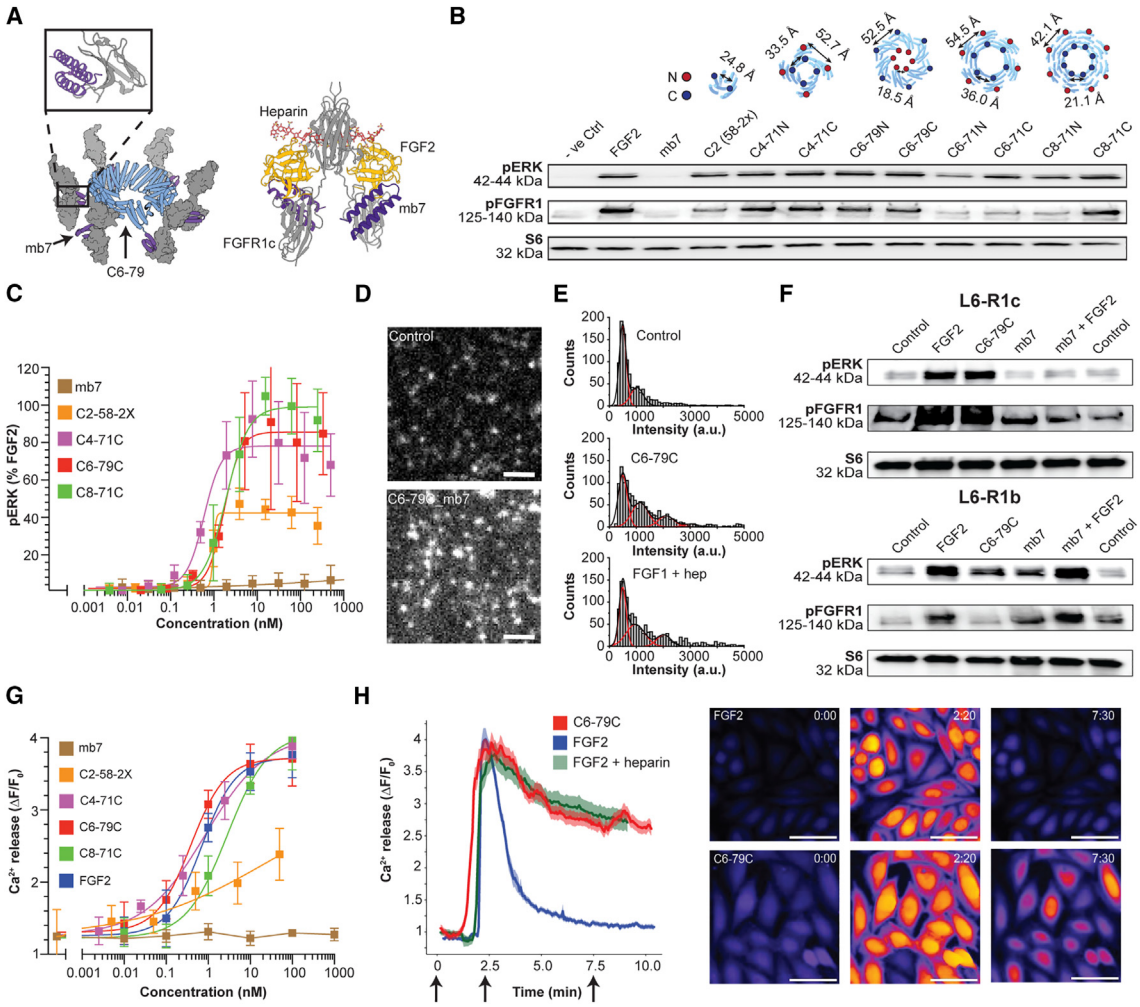

Figure 4. Modulation of FGFR signaling by designed agonists

(A) Cartoon model of C6-79C_mb7 oligomer (blue and purple) engaging six FGF receptors (gray). Top left: cartoon model of mb7 engaging FGFR4 domain 3 (PDB: 7N1J). Right: natural geometry of signaling competent FGF2 (yellow) with FGFR1c (gray) and heparin (red) (PDB: 1FQ9) together with superimposed mb7 (purple).

(B) Signaling response to a library of oligomers presenting mb7 in CHO-R1c cells, treated at 10 nM each, analyzed through western blot. Top: cartoons of oligomers presenting mb7 at their N or C termini; distances between neighboring chains are shown above their respective treatments. Total FGFR1 and ERK loading controls can be found in Figure S14.

(C) Dose-response curves of selected designs via phosphoflow for pERK1/2 stimulation. Error bars represent SEM from three independent biological repeats.

(D) Single-particle tracking of FGFR1 molecules on the cell surface.

(E) Intensity histograms of receptor clusters on the cell surface reveals receptor clustering induced via oligomerization.

(F) Signaling response (pERK and pFGFR1) to FGF2, mb7, C6-79C_mb7, or mb7 + FGF2 in L6-R1c (top) or L6-R1b (bottom) cells, analyzed through western blot.

(G) Dose-response curves of selected designs, assessed through intracellular calcium release. Error bars represent SEM from three independent biological repeats.

(H) Comparison of a calcium intensity signaling trajectory after treatment with FGF2 (with or without heparin) or C6-79C_mb7 at 10 nM each. Right: exemplary images comparing the calcium response exhibited in CHO-R1c cells following treatment with FGF2 or C6-79C_mb7 at 10 nM across three different time points (0:00, 2:20, and 7:30 min). Scale bars: 2 μm in (D) and 50 μm in (H).

See also Figures S13–S22.

of the spectrum, cells treated with mb7 showed a marked preference for perivascular lineage, producing only 28% endothelial cells. Cells treated with a combination of mb7 and FGF2 were almost exclusively mesenchymal, producing a population that was 93% perivascular (Figure 5B). These results suggest that FGFR c-isoform activity is critical for the development of endothelial cells, and specific activation of the b-isoform instead biases the cells toward perivascular fate. Immunostainings of differentiated iPSCs for endothelial (CD31) and perivascular (PDGFR-B) markers at day 14 confirmed the primary cell fate after treatment with C6-79C_mb7 (FGFR c-isoform-specific signaling) or mb7 together with FGF2 (FGFR b-isoform-specific signaling), which led to the enrichment of endothelial or perivascular cells, respectively (Figure 5C).

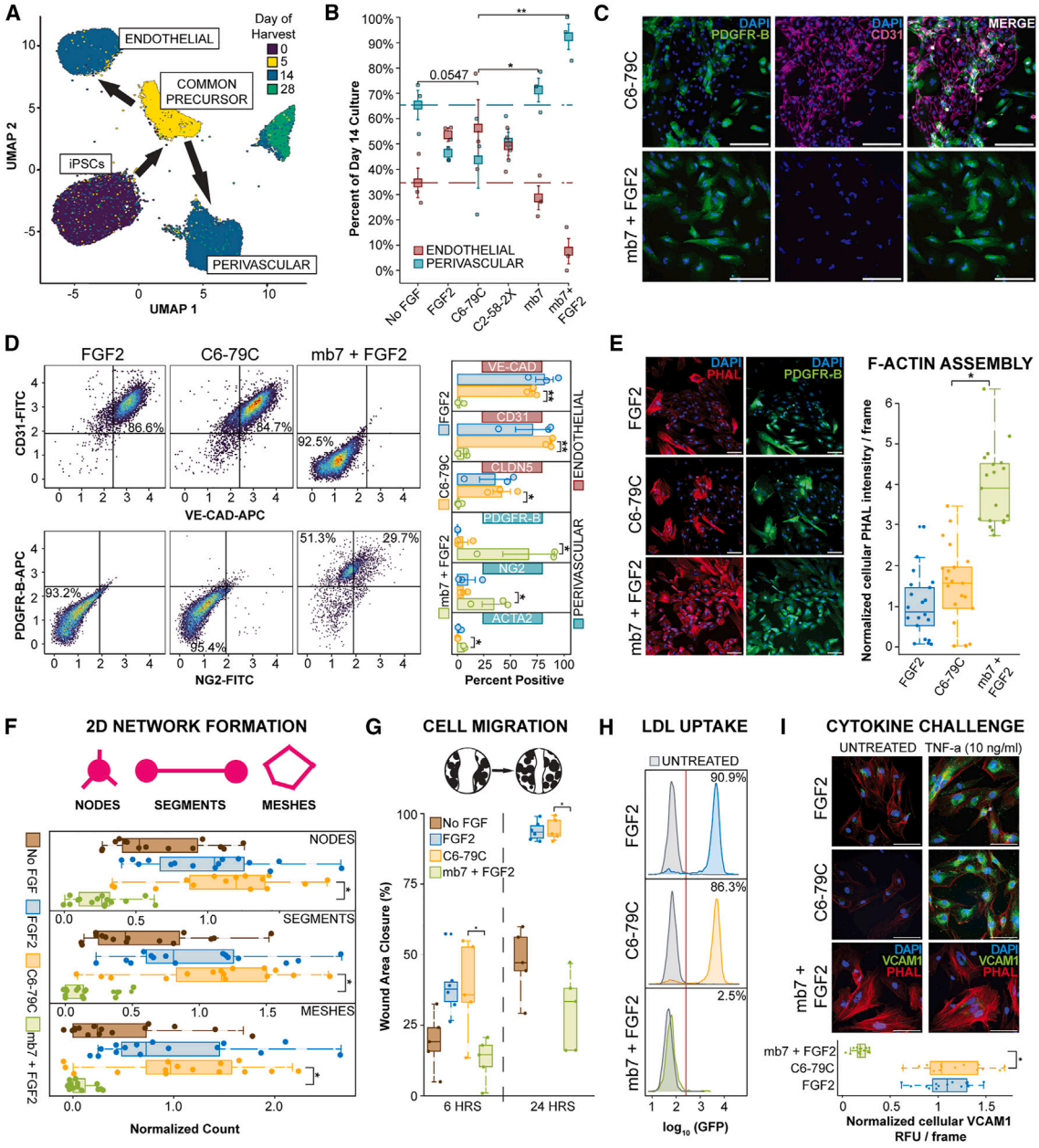

Figure 5. Control over vascular differentiation with designed agonists and antagonists

(A) UMAP embeddings of all sequenced cells colored by day of harvest, along with given cluster annotations.

(B) Proportion of endothelial or perivascular cells generated at day 14 following treatment with FGF2, C2-58-2X_mb7, C6-79C_mb7, mb7 alone, or mb7 in combination with FGF2. Error bars represent SEM from 3 independent biological repeats.

(C) Immunohistochemical characterization of differentiated cells treated with C6-79C_mb7 or mb7 in combination with FGF2, with PDGFR-B and CD31 to specifically mark perivascular and endothelial cells, respectively. Scale bars: 200 μm.

(D) Quantitative analysis of a select panel of endothelial (VE-cadherin, CD31, and CLND5) and perivascular (PDGFR-B, ACTA2, and NG2) markers using flow cytometry. Left: representative 2D scatterplots; Right: summarized results with mean and SEM from 3 independent biological repeats.

(E) F-actin assembly. Left: representative immunofluorescence images from FGF2, C6-79C_mb7 and mb7 + FGF2-derived cells (PDGFR-B, perivascular cells; PHAL, F-actin). Scale bars: 100 μm. Right: summarized per-cell phalloidin (PHAL) intensity from 3 independent biological repeats (7 randomly chosen field of views from each).

(F) 2D network formation. Normalized count of nodes, segments, and meshes after 24 h, summarized from 3 independent biological repeats (5 randomly chosen fields of view from each).

(G) Cell migration. Percentage closure of inflicted scratch area after 6 and 24 h, summarized from 3 independent biological repeats (3 randomly chosen field of views from each).

(H) LDL uptake. Representative flow cytometry of fluorescently labeled LDL uptake by cells generated using FGF2, C6-79C_mb7, and mb7 + FGF2 after 4 h of treatment. Mean and SEM are reported from 3 independent biological repeats.

(legend continued on next page)

We used flow cytometry with endothelial and perivascular cell surface markers to further characterize the cells harvested at day 14 of differentiation. Populations derived using FGF2 or C6-79C_mb7 were similar in composition, consisting primarily of endothelial cells (VE-cadherin$^+$ cells: 81.2% and 69.9%, respectively; CD31$^+$ cells: 70.1% and 87.2%, respectively; CLND5$^+$ cells: 34.9% and 41.2%, respectively), whereas cells derived using mb7 in combination with FGF2 were overwhelmingly perivascular in identity (PDGFR-B$^+$ cells: 76.2%; NG2$^+$ cells: 33.9%; ACTA2$^+$ cells: 16.2%) (Figure 5D). These results agree with the trend seen in the transcriptomic data—signaling of FGFRs through their c-isoform is critical for the development of endothelial cells, while b-isoform-specific signaling instead promotes the perivascular lineage.

Perivascular cells are contractile cells that are known to play a role in capillary blood flow regulation through the assembly of F-actin bundles[52,53]; we characterized our cell populations by measuring intracellular actin (using fluorescently labeled phalloidin) at day 14 of differentiation. Cells derived using mb7 + FGF2 exhibited ~4-fold increase in F-actin assembly over cells derived using FGF2 or C6-79C_mb7 (Figure 5E) owing to the robust formation of stress fibers in these perivascular cells. To characterize the functional maturity of the endothelial populations, we used tube formation,[54] cell migration,[55,56] LDL uptake,[57] and cytokine challenge[58] assays. The capacity to assemble into capillary-like tubules is a hallmark phenotype of endothelial cells,[59] and the cells derived via FGFR c-isoform activation demonstrated a robust 2D network formation capacity (measured by numbers of nodes, segments, and meshes in a tube formation assay) (Figures 5F and S24A). In addition, these cells readily migrated, completely sealing an inflicted scratch within 24 h (Figures 5G and S24B). Low-density lipoprotein (LDL) uptake is a critical process observed in endothelial cells to acquire cholesterol,[60] and we found that endothelial cells derived using FGF2 and C6-79C_mb7 (but not mb7 + FGF2) exhibited high and comparable levels of receptor-mediated uptake of fluorophore-labeled LDL (Figure 5H). Finally, endothelial cells are known to upregulate vascular cell adhesion molecule 1 (VCAM-1) (for adhesion and trans-endothelial migration of leukocytes) in response to inflammatory cytokines,[61,62] and we observed that endothelial cells derived using FGF2 and C6-79C_mb7 (but not mb7 + FGF2), upon exposure to tumor necrosis factor alpha (TNF-α), displayed a significant increase in VCAM-1 expression (Figure 5I). These results suggest that the endothelial cells generated via c-isoform activity are functional and mature, with increased endothelial functionality compared with cells derived using the FGFR c-isoform antagonist (mb7 + FGF2), which exhibit more of a perivascular identity.

Arterial versus venous endothelial cell fate specification

Sub-clustering of the day-14 endothelial expression data suggested that arterial and venous endothelial cells emerged in different ratios with the different treatments.[63] In order to characterize these sub-populations, we compared our endothelial expression data with a previously published RNA-seq dataset from arterial and venous endothelial cells generated from human pluripotent stem cells.[64] We used the genes identified as differentially expressed in arterial and venous cells in this dataset to assign an arteriovenous specificity score for each cell in our endothelial dataset, and classified cells that scored above the median specificity score as arterial, and cells below the score as venous. We found that endothelial cells generated with or without added FGF2 primarily adopted the venous cell fate (68% or 86% venous, respectively), while C6-79C_mb7 induced a strong bias toward an arterial-like endothelial cell fate (64% arterial-like) (Figure 6A).

We hypothesized that the clear emergence of endothelial subtypes at the protein level would require further maturation of the iPSC-derived endothelial cells. To this end, we adapted a previously described protocol for creating self-organizing 3D blood vessel organoids (BVOs) from pluripotent stem cells[65] (Figure S25A). These organoids contain the major cell types (endothelial and perivascular cells) that assemble into capillary-like networks, and, importantly, these organoids can be grown and matured for more than 60 days in culture. We replaced FGF2 in the protocol with an equivalent concentration of C6-79C_mb7 between days 5 and 13, which mimics days 2–5 in 2D culture in respect of the emergence of mesodermal intermediates and promotion of vascular lineages.[66] Organoids were harvested at day 37 and stained for VE-cadherin (to observe the formation of vascular networks) and EFNB2 (to detect arterial-like endothelial cells). Cells in organoids derived using C6-79C_mb7 exhibited significantly higher average expression of EFNB2 (Figures 6B and S25B), suggesting that c-isoform activation of FGFRs biases endothelial cells toward an arterial fate following maturation.

BVOs can form stable vascular networks upon transplantation into immunodeficient mice.[65,66] To investigate whether organoids generated using C6-79C_mb7 could replicate this phenotype, we transplanted day 21 C6-79C_mb7-derived and FGF2-derived organoids under the kidney capsule of immunodeficient mice and harvested tissues after 3 weeks. Immunohistochemical analysis revealed the emergence of human vascular endothelial (hVE-cadherin+ or hCD31+) networks with outgrowths into the surrounding stroma that formed connections with mouse (mCD31+) vascular cells (Figures 6C and S26). These results highlight the potential of designed proteins as tailored agonists for differentiation of cells into highly specific lineages.

DISCUSSION

The extensible star-shaped oligomers designed in this work considerably expand the tools available for clustering cell surface receptors and other targets with different valencies and geometries. The designed scaffolds are highly expressed in *E. coli* and the spacing of attached binding domains can be systematically varied simply by adding or deleting the modular repeat

(I) Cytokine challenge assay. Representative immunofluorescence images of cells treated with TNF-α (10 ng/mL) for 24 h, summarized from 3 independent biological repeats (5 randomly chosen fields from each) (VCAM1, vascular cell adhesion molecule 1). Scale bars: 100 μm. *$p < 0.05$, **$p < 0.01$, Student's two-tailed t test.

See also Figures S23 and S24 and Table S7.

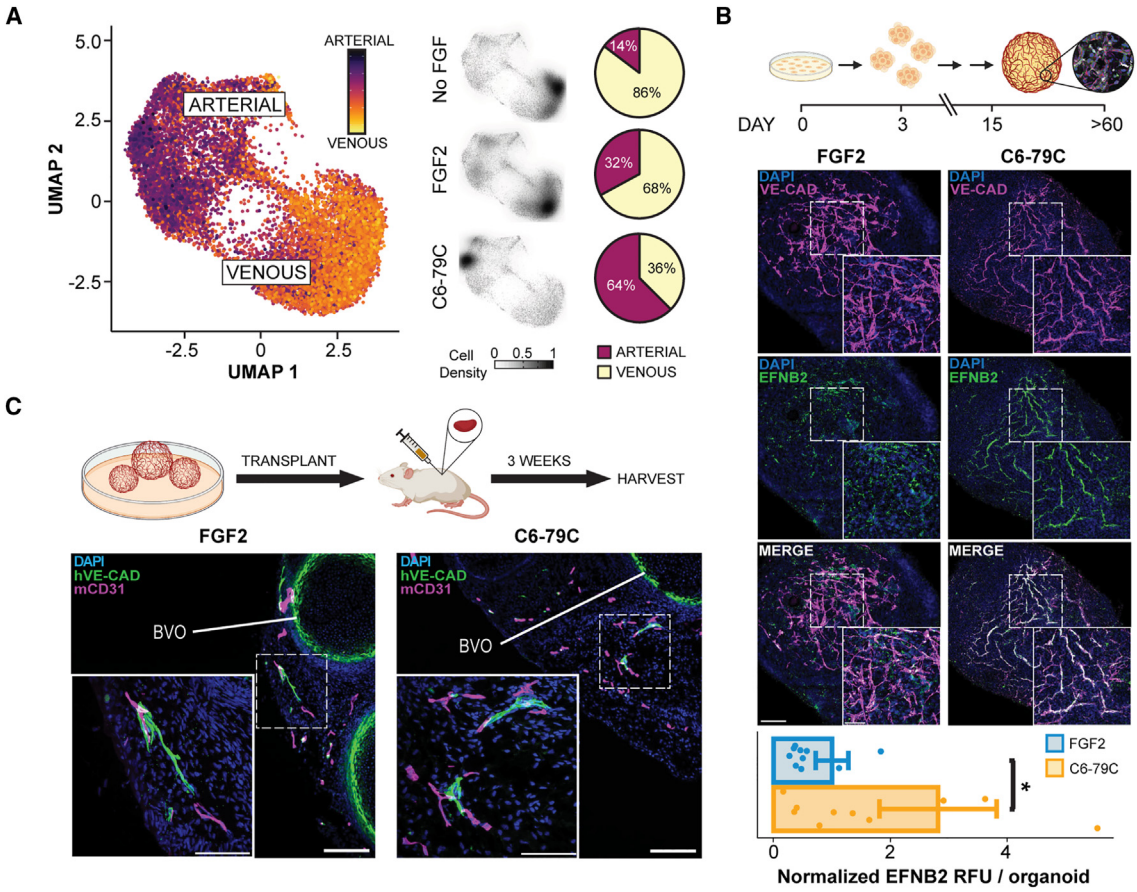

Figure 6. Control over endothelial subtype fate via isoform-specific agonism

(A) Left: UMAP embeddings of sub-clustered endothelial cells, colored by arteriovenous cell specificity. Middle: density plots showing specific endothelial subtype populations enriched by the individual treatments. Right: proportion of arterial or venous endothelial cells generated at day 14 following treatment with No FGF, FGF2, or C6-79C_mb7.

(B) Top: representative immunofluorescence images of blood vessel organoids (BVOs) generated using FGF2 or C6-79C_mb7. Vascular networks are marked with VE-cadherin and arterial-like endothelial cells are marked with EFNB2. Scale bars: 200 μm (whole) and 50 μm (inset). Bottom: per-organoid quantification of EFNB2, summarizing 10 independently generated organoids from each treatment.

(C) Immunohistochemical characterization of BVOs transplanted under the mouse kidney capsule. Scale bars: 200 μm (whole) and 100 μm (inset). *$p < 0.05$, Student's two-tailed t test.

See also Figures S25 and S26.

units. C8-71 and its extensions are the first designed scaffolds offering both a defined octameric symmetry and a stepwise variation in diameter through repeat units. The highest success rate was achieved with the DHR71 building block, perhaps because the design model (used in the docking protocol to avoid issues of missing terminal residues or imperfect repeat unit symmetry in the crystal structure) was closer to the crystal structure (0.67 Å RMSD),[25] leading to greater accuracy of the oligomer computational models.

FGFR homodimerizes upon FGF binding, and hence attention has focused on activation of the FGFR pathway by receptor homodimerization and heparin-based oligomerization.[67] The multivalent binders stimulate FGFR activation by dimerizing FGFRs or by driving higher order assemblies. We observed pathway activation by C2, C4, C6, and C8 FGFR engaging ligands, which varied when the geometry of presentation was tuned by varying the length of the radially extending arms. The C4 extension series revealed a strong distance dependence for activation: mb7 templated 53 Å apart showed strong pERK signaling, whereas the larger constructs with extension lengths of 76 and 96 Å did not signal, consistent with the FGF2-FGFR1 dimer complex structure (PDB: 1FQ9)[68] in which the membrane proximal termini are 48 Å apart. Direct measurement of FGFR diffusion in the membrane (Figure S17) and of the oligomerization state of the receptor in the membrane (Figures 4D and 4E) suggest that synthetic ligands drive FGFR clustering.

Commercially available naturally occurring signaling molecules (such as FGF2) often have pleiotropic effects and it can be difficult to use these to promote differentiation of highly specific cell subpopulations; small molecule treatments can have similar limitations. Our designed proteins not only recapitulate classical aspects of FGF signaling but also have a number of

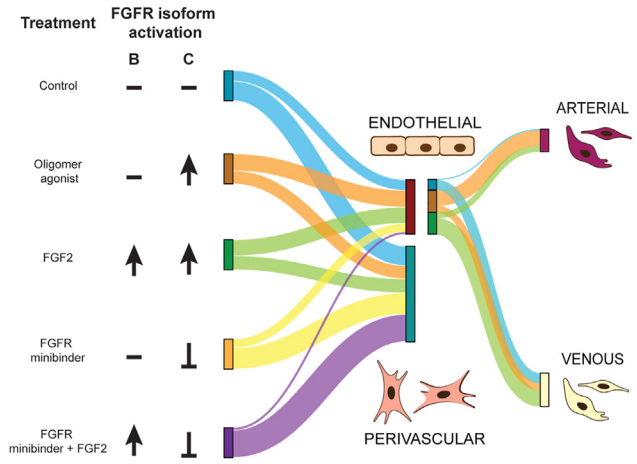

Figure 7. Control over vascular differentiation

At the first bifurcation, the designs enable selective formation of endothelial or perivascular cells, and in subsequent endothelial cell differentiation, synthetic agonist treatments bias toward arterial fate.

distinct advantages in sustained signaling, promotion of vascular differentiation, and ease of production. Likely because of the slow off rate of mb7 for FGFR, and the avid binding of the multivalent constructs, the calcium transients elicited by our synthetic agonists have longer duration than those elicited by FGF. The specificity of mb7 for the c-isoform[21] enables specific activation of signaling through the c-isoform receptor, while addition of mb7 to FGF enables activation of signaling exclusively through the b-isoform. These and perhaps other subtle differences in proximal signaling result in distinct outcomes at multiple developmental stages in vascular differentiation. Our designed scaffolds provide a means to control the prevalence of endothelial or perivascular cells by taking advantage of the capability to activate signaling through just the b- or just the c-receptor isoforms (Figure 7). In subsequent endothelial cell differentiation, C6-79C_mb7 promotes the arterial cell fate. Although the tissue distributions of different FGFR splice forms have been extensively characterized,[24] our work goes beyond previous studies by delineating their functional roles in vascular endothelial differentiation. Our splice-variant-specific designs can promote either the endothelial cell or perivascular fate, and can elicit specific subtypes of vascular endothelial cells, and should be useful for both probing biological mechanisms and therapeutic applications.

Limitations of the study

Here, we used flexible fusion of the FGFR-binding domain to preexisting oligomers; rigid fusion to custom-generated oligomers using methods such as RFDiffusion[18] could provide tighter control of receptor architecture and fine-tuning of signaling outcome.[10] On the biology side, we were unable to carry out genetic knockouts of FGFR1/2c to further test the role of this variant in the developing iPSC-derived endothelium because FGFR1/2c appears to be essential earlier during human pluripotency. Designed agonists and antagonists with receptor-isoform-dependent specificity provide an approach for probing the roles of different isoforms in developmental bifurcations when genetic knockouts are not feasible due to early essentiality. The designed-oligomer-based approach described here provides a versatile way in which to promote receptor clustering and shape pathway activation with multiple levels of control compared with the native signaling molecules: the receptor-binding domains can have higher receptor subtype specificity, the on and off rates for receptor subunits can be tuned, and the valency and geometry of receptor engagement can be systematically varied. We envision that such customized synthetic agonists will have broad applications in both *ex vivo* and *in vivo* control of cellular differentiation.

STAR★METHODS

Detailed methods are provided in the online version of this paper and include the following:

SUPPLEMENTAL INFORMATION

Supplemental information can be found online at https://doi.org/10.1016/j.cell.2024.05.025.

ACKNOWLEDGMENTS

We thank Michelle DeWitt for help with protein expression, George Ueda and Brent Herdlicka for advice on endotoxin removal methods, and Ryan Kibler for assistance with SAXS sample submission. We also want to thank Xinting Li, Mila Lamb, and Paul Levine for mass spectrometry verification of asymmetric units of the designs. We want to thank Mohamad Abedi and Maggie Ahlrichs for advice on phosphoflow cytometry and cell culture. We thank Luki Goldschmidt and Patrick Vecchiato for computational support. We also want to thank Will Sheffler for computational support. We thank Nanditaa Balachander and Yen Lim for help with molecular biology, Dr. Yan Ting Zhao for help with HUVEC cell culture, Professor Julie Mathieu for advice on differentiation assays, and Dale Hailey and the Garvey microscopy core for help with microscopy. We thank Thomas Perkins for initial discussions about the proteomics data acquisition. We thank William Rice, Alice Paquette, and Bing Wang of the NYU Cryo-EM Core Facility for assistance with cryo-EM grid screening. Collection of 300 kV data was enabled by a block allocation grant through the National Center for Cryo-EM Access and Training (NCCAT), and we thank Ed Eng, Carolina Hernandez, and Charlie Dubbeldam for their work in data collection, scheduling, sample handling, and grant administration. We thank all members of the Bhabha/Ekiert lab, especially Nicolas Coudray, for helpful discussions regarding computing and data processing, and we thank the NYU high-performance computing (HPC) team. All Krios datasets were collected through NCCAT, part of the Simons Electron Microscopy Center located at the New York Structural Biology Center. This work was supported by the Audacious Project at the Institute for Protein Design (T.S., F.P., Z.L., and D.B.); the ISCRM Fellows Award (T.V.); the Institute for Protein Design Breakthrough Fund (W.Y. and A.F.); The Nordstrom-Barrier Directors Fund at the Institute for Protein Design (A.E. and L.S.); Open Philanthropy (R.L.R., G.B., D.C.E., L. Carter, M.M., and D.B.); NIGMS grants R35GM128777 (D.C.E.) and R35GM150919 (D.K.S.); NHLBI grants R01HL146868, R01HL148081, and R01HL160825 (C.E.M.); National Institute on Aging grants R01 AG063845 (N.I.E., L. Cao, and D.B.) and U19AG065156 (D.R.H.); Human Frontier Science Program Long-Term Fellowship #LT000880/2019-L (F.P.); the European Molecular Biology Organization via ALTF191-2021 (T.S.); the Howard Hughes Medical Institution (B.C., D.B., and J.S.); the HHMI Hanna Gray Fellowship via GT11817 (N.B.); the ISCRM Fellows Program (A.P.); National Institutes of Health T90DE021984 (D.D.E.) and U01DK127553 and 5UC2 DK126006 (B.S.F.); the Brotman Baty Institute (BBI); NIH R01GM097372, R01GM083867, and 1P01GM081619; the NHLBI Progenitor Cell Biology Consortium (U01HL099997 and UO1HL099993); SCGE COF220919 and AHA 19IPLOI34760143 (H.R.-B.); and DOD PR203328 W81XWH-21-1-0006 (H.R.-B. and D.B.). Work at NCCAT is supported by the NIH Common Fund Transformative High Resolution Cryo-Electron Microscopy program (U24 GM129539) and by grants from the Simons Foundation (SF349247) and the NY State Assembly. The SAXS work was conducted at the Advanced Light Source (ALS), a national user facility operated by Lawrence Berkeley National Laboratory on behalf of the Department of Energy, Office of Basic Energy Sciences, through the Integrated Diffraction Analysis Technologies (IDAT) program, supported by DOE Office of Biological and Environmental Research. Additional support comes from the National Institute of Health project ALS-ENABLE (P30 GM124169) and a High-End Instrumentation grant S10OD018483.

AUTHOR CONTRIBUTIONS

N.I.E. and D.B. conceived the project. A.P. and H.R.-B. conceived analyzing the designed proteins in endothelial differentiation. N.I.E. and A.E. designed oligomeric constructs. W.Y., B.C., and D.R.H. designed building blocks for oligomers. N.I.E., T.S., A.F., Z.L., L.C., and M.M. characterized oligomers. F.P. developed the script for oligomer extension. R.L.R., G.B., D.C.E., and N.I.E. performed EM analysis of the designed constructs. N.B. performed cyclic docking of the oligomers. A.P., T.S., S.A., M.G., and D.D.E. performed cell assays. A.P., T.V., S.M., L.B., C.E.M., B.S.F., H.R-B., and Y.Z. designed, performed, or supervised animal experiments. A.P., D.D.E., and H.R-B. performed or supervised organoid assays. C.L. and D.K.S. performed proteomics experiments. L.C. and B.C. developed the minibinder. N.I.E., T.S., P.H., A.M., and S.G. purified the endotoxin-free protein. S.L. provided L6-R1c and L6-R1b cells. A.P. and S.R.S. performed the transcriptomics study. D.B., L.S., J.S., C.T., B.N., J.S., and H.R.-B. supervised the study. N.I.E., T.S., A.P., R.L.R., H.R.-B., and D.B. wrote the manuscript with input from all authors.

DECLARATION OF INTERESTS

L.S., D.B., N.I.E., T.S., A.E., A.F., W.Y., D.R.H., B.C., H.R.-B., A.P., R.L.R., G.B., and D.C.E. are coinventors on a patent application that has been filed by the University of Washington.

Received: December 16, 2022
Revised: February 14, 2024
Accepted: May 13, 2024
Published: June 10, 2024

REFERENCES

1. Garcia-Parajo, M.F., Cambi, A., Torreno-Pina, J.A., Thompson, N., and Jacobson, K. (2014). Nanoclustering as a dominant feature of plasma membrane organization. J. Cell Sci. *127*, 4995–5005. https://doi.org/10.1242/jcs.146340.
2. Wu, H. (2013). Higher-order assemblies in a new paradigm of signal transduction. Cell *153*, 287–292. https://doi.org/10.1016/J.CELL.2013.03.013.
3. Mayer, B.J., and Yu, J. (2018). Protein Clusters in Phosphotyrosine Signal Transduction. J. Mol. Biol. *430*, 4547–4556. https://doi.org/10.1016/J.JMB.2018.05.040.
4. Westerfield, J.M., and Barrera, F.N. (2020). Membrane receptor activation mechanisms and transmembrane peptide tools to elucidate them. J. Biol. Chem. *295*, 1792–1814. https://doi.org/10.1074/jbc.REV119.009457.
5. Zhang, K., Gao, H., Deng, R., and Li, J. (2019). Emerging Applications of Nanotechnology for Controlling Cell-Surface Receptor Clustering. Angew. Chem. Int. Ed. Engl. *58*, 4790–4799. https://doi.org/10.1002/anie.201809006.
6. Porębska, N., Ciura, K., Chorążewska, A., Zakrzewska, M., Otlewski, J., and Opaliński, Ł. (2023). Multivalent protein-drug conjugates - An emerging strategy for the upgraded precision and efficiency of drug delivery to cancer cells. Biotechnol. Adv. *67*, 108213. https://doi.org/10.1016/j.biotechadv.2023.108213.
7. Zhao, Y.T., Fallas, J.A., Saini, S., Ueda, G., Somasundaram, L., Zhou, Z., Xavier Raj, I., Xu, C., Carter, L., Wrenn, S., et al. (2021). F-domain valency determines outcome of signaling through the angiopoietin pathway. EMBO Rep. *22*, e53471. https://doi.org/10.15252/embr.202153471.
8. Divine, R., Dang, H.V., Ueda, G., Fallas, J.A., Vulovic, I., Sheffler, W., Saini, S., Zhao, Y.T., Raj, I.X., Morawski, P.A., et al. (2021). Designed proteins assemble antibodies into modular nanocages. Science *372*, eabd9994. https://doi.org/10.1126/science.abd9994.
9. Ben-Sasson, A.J., Watson, J.L., Sheffler, W., Johnson, M.C., Bittleston, A., Somasundaram, L., Decarreau, J., Jiao, F., Chen, J., Mela, I., et al. (2021). Design of biologically active binary protein 2D materials. Nature *589*, 468–473. https://doi.org/10.1038/s41586-020-03120-8.
10. Mohan, K., Ueda, G., Kim, A.R., Jude, K.M., Fallas, J.A., Guo, Y., Hafer, M., Miao, Y., Saxton, R.A., Piehler, J., et al. (2019). Topological control of cytokine receptor signaling induces differential effects in hematopoiesis. Science *364*, eaav7532. https://doi.org/10.1126/science.aav7532.
11. Moraga, I., Spangler, J.B., Mendoza, J.L., Gakovic, M., Wehrman, T.S., Krutzik, P., and Garcia, K.C. (2017). Synthekines are surrogate cytokine

and growth factor agonists that compel signaling through non-natural receptor dimers. eLife *6*, e22882. https://doi.org/10.7554/eLife.22882.

12. Yang, C., Sesterhenn, F., Bonet, J., van Aalen, E.A., Scheller, L., Abriata, L.A., Cramer, J.T., Wen, X., Rosset, S., Georgeon, S., et al. (2021). Bottom-up de novo design of functional proteins with complex structural features. Nat. Chem. Biol. *17*, 492–500. https://doi.org/10.1038/s41589-020-00699-x.
13. Shaw, A., Lundin, V., Petrova, E., Fördős, F., Benson, E., Al-Amin, A., Herland, A., Blokzijl, A., Högberg, B., and Teixeira, A.I. (2014). Spatial control of membrane receptor function using ligand nanocalipers. Nat. Methods *11*, 841–846. https://doi.org/10.1038/nmeth.3025.
14. Taga, T., and Kishimoto, T. (1997). Gp130 and the interleukin-6 family of cytokines. Annu. Rev. Immunol. *15*, 797–819. https://doi.org/10.1146/annurev.immunol.15.1.797.
15. Martinez-Moczygemba, M., and Huston, D.P. (2003). Biology of common β receptor–signaling cytokines: il-3, IL-5, and GM-CSF. J. Allergy Clin. Immunol. *112*, 653–665. https://doi.org/10.1016/S0091.
16. Boulanger, M.J., Chow, D.C., Brevnova, E.E., and Garcia, K.C. (2003). Hexameric structure and assembly of the interleukin-6/IL-6 alpha-receptor/gp130 complex. Science *300*, 2101–2104. https://doi.org/10.1126/science.1083901.
17. Gerben, S.R., Borst, A.J., Hicks, D.R., Moczygemba, I., Feldman, D., Coventry, B., Yang, W., Bera, A.K., Miranda, M., Kang, A., et al. (2023). Design of Diverse Asymmetric Pockets in De Novo Homo-oligomeric Proteins. Biochemistry *62*, 358–368. https://doi.org/10.1021/acs.biochem.2c00497.
18. Watson, J.L., Juergens, D., Bennett, N.R., Trippe, B.L., Yim, J., Eisenach, H.E., Ahern, W., Borst, A.J., Ragotte, R.J., Milles, L.F., et al. (2023). De novo design of protein structure and function with RFdiffusion. Nature *620*, 1089–1100. https://doi.org/10.1038/s41586-023-06415-8.
19. Wicky, B.I.M., Milles, L.F., Courbet, A., Ragotte, R.J., Dauparas, J., Kinfu, E., Tipps, S., Kibler, R.D., Baek, M., DiMaio, F., et al. (2022). Hallucinating symmetric protein assemblies. Science *378*, 56–61. https://doi.org/10.1126/science.add1964.
20. Fallas, J.A., Ueda, G., Sheffler, W., Nguyen, V., McNamara, D.E., Sankaran, B., Pereira, J.H., Parmeggiani, F., Brunette, T.J., Cascio, D., et al. (2017). Computational design of self-assembling cyclic protein homo-oligomers. Nat. Chem. *9*, 353–360. https://doi.org/10.1038/NCHEM.2673.
21. Park, J.S., Choi, J., Cao, L., Mohanty, J., Suzuki, Y., Park, A., Baker, D., Schlessinger, J., and Lee, S. (2022). Isoform-specific inhibition of FGFR signaling achieved by a de-novo-designed mini-protein. Cell Rep. *41*, 111545. https://doi.org/10.1016/j.celrep.2022.111545.
22. Holzmann, K., Grunt, T., Heinzle, C., Sampl, S., Steinhoff, H., Reichmann, N., Kleiter, M., Hauck, M., and Marian, B. (2012). Alternative Splicing of Fibroblast Growth Factor Receptor IgIII Loops in Cancer. J. Nucleic Acids *2012*, 950508. https://doi.org/10.1155/2012/950508.
23. Yeh, B.K., Igarashi, M., Eliseenkova, A.V., Plotnikov, A.N., Sher, I., Ron, D., Aaronson, S.A., and Mohammadi, M. (2003). Structural basis by which alternative splicing confers specificity in fibroblast growth factor receptors. Proc. Natl. Acad. Sci. USA *100*, 2266–2271. https://doi.org/10.1073/pnas.0436500100.
24. Turner, N., and Grose, R. (2010). Fibroblast growth factor signalling: from development to cancer. Nat. Rev. Cancer *10*, 116–129. https://doi.org/10.1038/nrc2780.
25. Brunette, T.J., Parmeggiani, F., Huang, P.-S.S., Bhabha, G., Ekiert, D.C., Tsutakawa, S.E., Hura, G.L., Tainer, J.A., and Baker, D. (2015). Exploring the repeat protein universe through computational protein design. Nature *528*, 580–584. https://doi.org/10.1038/nature16162.
26. Brunette, T.J., Bick, M.J., Hansen, J.M., Chow, C.M., Kollman, J.M., and Baker, D. (2020). Modular repeat protein sculpting using rigid helical junctions. Proc. Natl. Acad. Sci. USA *117*, 8870–8875. https://doi.org/10.1073/pnas.1908768117.
27. Sheffler, W., Yang, E.C., Dowling, Q., Hsia, Y., Fries, C.N., Stanislaw, J., Langowski, M., Brandys, M., Khmelinskaia, A., King, N.P., et al. Fast and versatile sequence-independent protein docking for nanomaterials design using RPXDock. PLoS Comput. Biol. 19, e1010680. 10.1371/journal.pcbi.1010680.
28. Coventry, B., and Baker, D. (2021). Protein sequence optimization with a pairwise decomposable penalty for buried unsatisfied hydrogen bonds. PLoS Comput. Biol. *17*, e1008061. https://doi.org/10.1371/journal.pcbi.1008061.
29. Boyken, S.E., Chen, Z., Groves, B., Langan, R.A., Oberdorfer, G., Ford, A., Gilmore, J.M., Xu, C., DiMaio, F., Pereira, J.H., et al. (2016). De novo design of protein homo-oligomers with modular hydrogen-bond network-mediated specificity. Science *352*, 680–687. https://doi.org/10.1126/science.aad8865.
30. Maguire, J.B., Haddox, H.K., Strickland, D., Halabiya, S.F., Coventry, B., Griffin, J.R., Pulavarti, S.V.S.R.K., Cummins, M., Thieker, D.F., Klavins, E., et al. (2021). Perturbing the energy landscape for improved packing during computational protein design. Proteins *89*, 436–449. https://doi.org/10.1002/prot.26030.
31. Yang, W., Hicks, D.R., Ghosh, A., Schwartze, T.A., Coventry, B., Goreshnik, I., Allen, A., Halabiya, S.F., Kim, C.J., Hinck, C.S., et al. (2024). Design of High Affinity Binders to Convex Protein Target Sites. Preprint at bioRxiv. https://doi.org/10.1101/2024.05.01.592114.
32. Dyer, K.N., Hammel, M., Rambo, R.P., Tsutakawa, S.E., Rodic, I., Classen, S., Tainer, J.A., and Hura, G.L. (2014). High-throughput SAXS for the characterization of biomolecules in solution: a practical approach. Methods Mol. Biol. *1091*, 245–258. https://doi.org/10.1007/978-1-62703-691-7_12.
33. Classen, S., Hura, G.L., Holton, J.M., Rambo, R.P., Rodic, I., McGuire, P.J., Dyer, K., Hammel, M., Meigs, G., Frankel, K.A., et al. (2013). Implementation and performance of SIBYLS: a dual endstation small-angle X-ray scattering and macromolecular crystallography beamline at the Advanced Light Source. J. Appl. Crystallogr. *46*, 1–13. https://doi.org/10.1107/S0021889812048698.
34. Putnam, C.D., Hammel, M., Hura, G.L., and Tainer, J.A. (2007). X-ray solution scattering (SAXS) combined with crystallography and computation: defining accurate macromolecular structures, conformations and assemblies in solution. Q. Rev. Biophys. *40*, 191–285. https://doi.org/10.1017/S0033583507004635.
35. Lemmon, M.A., and Schlessinger, J. (2010). Cell signaling by receptor tyrosine kinases. Cell *141*, 1117–1134. https://doi.org/10.1016/j.cell.2010.06.011.
36. Cao, L., Coventry, B., Goreshnik, I., Huang, B., Sheffler, W., Park, J.S., Jude, K.M., Marković, I., Kadam, R.U., Verschueren, K.H.G., et al. (2022). Design of protein-binding proteins from the target structure alone. Nature *605*, 551–560. https://doi.org/10.1038/s41586-022-04654-9.
37. Ornitz, D.M., and Itoh, N. (2015). The Fibroblast Growth Factor signaling pathway. Wiley Interdiscip. Rev. Dev. Biol. *4*, 215–266. https://doi.org/10.1002/wdev.176.
38. Ferguson, H.R., Smith, M.P., and Francavilla, C. (2021). Fibroblast Growth Factor Receptors (FGFRs) and Noncanonical Partners in Cancer Signaling. Cells *10*, 1–35. https://doi.org/10.3390/cells10051201.
39. Wu, S., Jin, L., Vence, L., and Radvanyi, L.G. (2010). Development and application of "phosphoflow" as a tool for immunomonitoring. Expert Rev. Vaccines *9*, 631–643. https://doi.org/10.1586/erv.10.59.
40. Los, G.V., Encell, L.P., McDougall, M.G., Hartzell, D.D., Karassina, N., Zimprich, C., Wood, M.G., Learish, R., Ohana, R.F., Urh, M., et al. (2008). HaloTag: A novel protein labeling technology for cell imaging and protein analysis. ACS Chem. Biol. *3*, 373–382. https://doi.org/10.1021/cb800025k.
41. Jaqaman, K., Kuwata, H., Touret, N., Collins, R., Trimble, W.S., Danuser, G., and Grinstein, S. (2011). Cytoskeletal control of CD36 diffusion promotes its receptor and signaling function. Cell *146*, 593–606. https://doi.org/10.1016/j.cell.2011.06.049.

42. Lee, S.-H., Shin, J.Y., Lee, A., and Bustamante, C. (2012). Counting single photoactivatable fluorescent molecules by photoactivated localization microscopy (PALM). Proc. Natl. Acad. Sci. USA *109*, 17436–17441. https://doi.org/10.1073/pnas.1215175109.

43. Gong, S.-G. (2014). Isoforms of receptors of fibroblast growth factors. J. Cell. Physiol. *229*, 1887–1895. https://doi.org/10.1002/jcp.24649.

44. Kumar, V., Goutam, R.S., Park, S., Lee, U., and Kim, J. (2021). Functional Roles of FGF Signaling in Early Development of Vertebrate Embryos. Cells *10*, 2148. https://doi.org/10.3390/cells10082148.

45. Dorey, K., and Amaya, E. (2010). FGF signalling: diverse roles during early vertebrate embryogenesis. Development *137*, 3731–3742. https://doi.org/10.1242/dev.037689.

46. Yu, P., Wilhelm, K., Dubrac, A., Tung, J.K., Alves, T.C., Fang, J.S., Xie, Y., Zhu, J., Chen, Z., De Smet, F., et al. (2017). FGF-dependent metabolic control of vascular development. Nature *545*, 224–228. https://doi.org/10.1038/nature22322.

47. Javerzat, S., Auguste, P., and Bikfalvi, A. (2002). The role of fibroblast growth factors in vascular development. Trends Mol. Med. *8*, 483–489. https://doi.org/10.1016/S1471-4914(02)02394-8.

48. Di Matteo, A., Belloni, E., Pradella, D., Cappelletto, A., Volf, N., Zacchigna, S., and Ghigna, C. (2020). Alternative splicing in endothelial cells: novel therapeutic opportunities in cancer angiogenesis. J. Exp. Clin. Cancer Res. *39*, 275. https://doi.org/10.1186/s13046-020-01753-1.

49. Palpant, N.J., Pabon, L., Friedman, C.E., Roberts, M., Hadland, B., Zaunbrecher, R.J., Bernstein, I., Zheng, Y., and Murry, C.E. (2017). Generating high-purity cardiac and endothelial derivatives from patterned mesoderm using human pluripotent stem cells. Nat. Protoc. *12*, 15–31. https://doi.org/10.1038/nprot.2016.153.

50. Ornitz, D.M., Xu, J., Colvin, J.S., McEwen, D.G., MacArthur, C.A., Coulier, F., Gao, G., and Goldfarb, M. (1996). Receptor Specificity of the Fibroblast Growth Factor Family. J. Biol. Chem. *271*, 15292–15297. https://doi.org/10.1074/jbc.271.25.15292.

51. Cao, J., Spielmann, M., Qiu, X., Huang, X., Ibrahim, D.M., Hill, A.J., Zhang, F., Mundlos, S., Christiansen, L., Steemers, F.J., et al. (2019). The single-cell transcriptional landscape of mammalian organogenesis. Nature *566*, 496–502. https://doi.org/10.1038/s41586-019-0969-x.

52. Kureli, G., Yilmaz-Ozcan, S., Erdener, S.E., Donmez-Demir, B., Yemisci, M., Karatas, H., and Dalkara, T. (2020). F-actin polymerization contributes to pericyte contractility in retinal capillaries. Exp. Neurol. *332*, 113392. https://doi.org/10.1016/j.expneurol.2020.113392.

53. Erdener, Ş.E., Küreli, G., and Dalkara, T. (2022). Contractile apparatus in CNS capillary pericytes. Neurophotonics *9*, 021904. https://doi.org/10.1117/1.NPh.9.2.021904.

54. Kubota, Y., Kleinman, H.K., Martin, G.R., and Lawley, T.J. (1988). Role of laminin and basement membrane in the morphological differentiation of human endothelial cells into capillary-like structures. J. Cell Biol. *107*, 1589–1598. https://doi.org/10.1083/jcb.107.4.1589.

55. Liang, C.-C., Park, A.Y., and Guan, J.-L. (2007). In vitro scratch assay: a convenient and inexpensive method for analysis of cell migration in vitro. Nat. Protoc. *2*, 329–333. https://doi.org/10.1038/nprot.2007.30.

56. Chim, S.M., Qin, A., Tickner, J., Pavlos, N., Davey, T., Wang, H., Guo, Y., Zheng, M.H., and Xu, J. (2011). EGFL6 promotes endothelial cell migration and angiogenesis through the activation of extracellular signal-regulated kinase. J. Biol. Chem. *286*, 22035–22046. https://doi.org/10.1074/jbc.M110.187633.

57. Voyta, J.C., Via, D.P., Butterfield, C.E., and Zetter, B.R. (1984). Identification and isolation of endothelial cells based on their increased uptake of acetylated-low density lipoprotein. J. Cell Biol. *99*, 2034–2040. https://doi.org/10.1083/jcb.99.6.2034.

58. Amersfoort, J., Eelen, G., and Carmeliet, P. (2022). Immunomodulation by endothelial cells - partnering up with the immune system? Nat. Rev. Immunol. *22*, 576–588. https://doi.org/10.1038/s41577-022-00694-4.

59. Arnaoutova, I., and Kleinman, H.K. (2010). In vitro angiogenesis: endothelial cell tube formation on gelled basement membrane extract. Nat. Protoc. *5*, 628–635. https://doi.org/10.1038/nprot.2010.6.

60. Zhang, X., Sessa, W.C., and Fernández-Hernando, C. (2018). Endothelial Transcytosis of Lipoproteins in Atherosclerosis. Front. Cardiovasc. Med. *5*, 130. https://doi.org/10.3389/fcvm.2018.00130.

61. Chiu, J.-J., Lee, P.-L., Chen, C.-N., Lee, C.-I., Chang, S.-F., Chen, L.-J., Lien, S.-C., Ko, Y.-C., Usami, S., and Chien, S. (2004). Shear stress increases ICAM-1 and decreases VCAM-1 and E-selectin expressions induced by tumor necrosis factor-[alpha] in endothelial cells. Arterioscler. Thromb. Vasc. Biol. *24*, 73–79. https://doi.org/10.1161/01.ATV.0000106321.63667.24.

62. Singh, R.J.R., Mason, J.C., Lidington, E.A., Edwards, D.R., Nuttall, R.K., Khokha, R., Knauper, V., Murphy, G., and Gavrilovic, J. (2005). Cytokine stimulated vascular cell adhesion molecule-1 (VCAM-1) ectodomain release is regulated by TIMP-3. Cardiovasc. Res. *67*, 39–49. https://doi.org/10.1016/j.cardiores.2005.02.020.

63. Potente, M., and Mäkinen, T. (2017). Vascular heterogeneity and specialization in development and disease. Nat. Rev. Mol. Cell Biol. *18*, 477–494. https://doi.org/10.1038/nrm.2017.36.

64. Ang, L.T., Nguyen, A.T., Liu, K.J., Chen, A., Xiong, X., Curtis, M., Martin, R.M., Raftry, B.C., Ng, C.Y., Vogel, U., et al. (2022). Generating human artery and vein cells from pluripotent stem cells highlights the arterial tropism of Nipah and Hendra viruses. Cell *185*, 2523–2541.e30. https://doi.org/10.1016/j.cell.2022.05.024.

65. Wimmer, R.A., Leopoldi, A., Aichinger, M., Wick, N., Hantusch, B., Novatchkova, M., Taubenschmid, J., Hämmerle, M., Esk, C., Bagley, J.A., et al. (2019). Human blood vessel organoids as a model of diabetic vasculopathy. Nature *565*, 505–510. https://doi.org/10.1038/s41586-018-0858-8.

66. Nikolova, M.T., He, Z., Wimmer, R.A., Seimiya, M., Nikoloff, J.M., Penninger, J.M., Gray Camp, J., and Treutlein, B. (2022). Fate and state transitions during human blood vessel organoid development. Preprint at bioRxiv. https://doi.org/10.1101/2022.03.23.485329.

67. Spivak-Kroizman, T., Lemmon, M.A., Dikic, I., Ladbury, J.E., Pinchasi, D., Huang, J., Jaye, M., Crumley, G., Schlessinger, J., and Lax, I. (1994). Heparin-induced oligomerization of FGF molecules is responsible for FGF receptor dimerization, activation, and cell proliferation. Cell *79*, 1015–1024. https://doi.org/10.1016/0092-8674(94)90032-9.

68. Schlessinger, J., Plotnikov, A.N., Ibrahimi, O.A., Eliseenkova, A.V., Yeh, B.K., Yayon, A., Linhardt, R.J., and Mohammadi, M. (2000). Crystal structure of a ternary FGF-FGFR-heparin complex reveals a dual role for heparin in FGFR binding and dimerization. Mol. Cell *6*, 743–750. https://doi.org/10.1016/s1097-2765(00)00073-3.

69. Leman, J.K., Weitzner, B.D., Lewis, S.M., Adolf-Bryfogle, J., Alam, N., Alford, R.F., Aprahamian, M., Baker, D., Barlow, K.A., Barth, P., et al. (2020). Macromolecular modeling and design in Rosetta: recent methods and frameworks. Nat. Methods *17*, 665–680. https://doi.org/10.1038/s41592-020-0848-2.

70. Zivanov, J., Nakane, T., Forsberg, B.O., Kimanius, D., Hagen, W.J., Lindahl, E., and Scheres, S.H. (2018). New tools for automated high-resolution cryo-EM structure determination in RELION-3. eLife *7*, e42166. https://doi.org/10.7554/eLife.42166.

71. Punjani, A., Rubinstein, J.L., Fleet, D.J., and Brubaker, M.A. (2017). cryoSPARC: algorithms for rapid unsupervised cryo-EM structure determination. Nat. Methods *14*, 290–296. https://doi.org/10.1038/nmeth.4169.

72. Bell, J.M., Chen, M., Durmaz, T., Fluty, A.C., and Ludtke, S.J. (2018). New software tools in EMAN2 inspired by EMDatabank map challenge. J. Struct. Biol. *204*, 283–290. https://doi.org/10.1016/j.jsb.2018.09.002.

73. Hohn, M., Tang, G., Goodyear, G., Baldwin, P.R., Huang, Z., Penczek, P.A., Yang, C., Glaeser, R.M., Adams, P.D., and Ludtke, S.J. (2007). SPARX, a new environment for Cryo-EM image processing. J. Struct. Biol. *157*, 47–55. https://doi.org/10.1016/j.jsb.2006.07.003.

74. Schneidman-Duhovny, D., Hammel, M., and Sali, A. (2010). FoXS: a web server for rapid computation and fitting of SAXS profiles. Nucleic Acids Res. *38*, W540–W544. https://doi.org/10.1093/NAR/GKQ461.

75. Suloway, C., Pulokas, J., Fellmann, D., Cheng, A., Guerra, F., Quispe, J., Stagg, S., Potter, C.S., and Carragher, B. (2005). Automated molecular microscopy: the new Leginon system. J. Struct. Biol. *151*, 41–60. https://doi.org/10.1016/j.jsb.2005.03.010.

76. Zheng, S.Q., Palovcak, E., Armache, J.-P., Verba, K.A., Cheng, Y., and Agard, D.A. (2017). MotionCor2: anisotropic correction of beam-induced motion for improved cryo-electron microscopy. Nat. Methods *14*, 331–332. https://doi.org/10.1038/nmeth.4193.

77. Lander, G.C., Stagg, S.M., Voss, N.R., Cheng, A., Fellmann, D., Pulokas, J., Yoshioka, C., Irving, C., Mulder, A., Lau, P.-W., et al. (2009). Appion: an integrated, database-driven pipeline to facilitate EM image processing. J. Struct. Biol. *166*, 95–102. https://doi.org/10.1016/j.jsb.2009.01.002.

78. Tan, Y.Z., Baldwin, P.R., Davis, J.H., Williamson, J.R., Potter, C.S., Carragher, B., and Lyumkis, D. (2017). Addressing preferred specimen orientation in single-particle cryo-EM through tilting. Nat. Methods *14*, 793–796. https://doi.org/10.1038/nmeth.4347.

79. Pettersen, E.F., Goddard, T.D., Huang, C.C., Couch, G.S., Greenblatt, D.M., Meng, E.C., and Ferrin, T.E. (2004). UCSF Chimera—a visualization system for exploratory research and analysis. J. Comput. Chem. *25*, 1605–1612. https://doi.org/10.1002/jcc.20084.

80. Adams, P.D., Afonine, P.V., Bunkóczi, G., Chen, V.B., Davis, I.W., Echols, N., Headd, J.J., Hung, L.-W., Kapral, G.J., Grosse-Kunstleve, R.W., et al. (2012). PHENIX: a comprehensive Python-based system for macromolecular structure solution. Acta Crystallogr. D Biol. Crystallogr. *66*, 213–221. https://doi.org/10.1107/S0907444909052925.

81. Emsley, P., Lohkamp, B., Scott, W.G., and Cowtan, K. (2010). Features and development of Coot. Acta Crystallogr. D Biol. Crystallogr. *66*, 486–501. https://doi.org/10.1107/S0907444910007493.

82. Holden, S.J., Uphoff, S., Hohlbein, J., Yadin, D., Le Reste, L., Britton, O.J., and Kapanidis, A.N. (2010). Defining the Limits of Single-Molecule FRET Resolution in TIRF Microscopy. Biophys. J. *99*, 3102–3111. https://doi.org/10.1016/J.BPJ.2010.09.005.

83. Ellis, B., Haaland, P., Hahne, F., Le Meur, N., Gopalakrishnan, N., Spidlen, J., Jiang, M., and Finak, G. (2024). flowCore: Basic structures for flow cytometry data. Bioconductor. http://bioconductor.org/packages/flowCore/.

84. Schindelin, J., Arganda-Carreras, I., Frise, E., Kaynig, V., Longair, M., Pietzsch, T., Preibisch, S., Rueden, C., Saalfeld, S., Schmid, B., et al. (2012). Fiji: an open-source platform for biological-image analysis. Nat. Methods *9*, 676–682. https://doi.org/10.1038/nmeth.2019.

85. Trapnell, C., Cacchiarelli, D., Grimsby, J., Pokharel, P., Li, S., Morse, M., Lennon, N.J., Livak, K.J., Mikkelsen, T.S., and Rinn, J.L. (2014). The dynamics and regulators of cell fate decisions are revealed by pseudotemporal ordering of single cells. Nat. Biotechnol. *32*, 381–386. https://doi.org/10.1038/nbt.2859.

86. Carpentier, G., Berndt, S., Ferratge, S., Rasband, W., Cuendet, M., Uzan, G., and Albanese, P. (2020). Angiogenesis Analyzer for ImageJ—A comparative morphometric analysis of "Endothelial Tube Formation Assay" and "Fibrin Bead Assay". Sci. Rep. *10*, 11568. https://doi.org/10.1038/s41598-020-67289-8.

87. Suarez-Arnedo, A., Torres Figueroa, F., Clavijo, C., Arbeláez, P., Cruz, J.C., and Muñoz-Camargo, C. (2020). An image J plugin for the high throughput image analysis of in vitro scratch wound healing assays. PLoS One *15*, e0232565. https://doi.org/10.1371/journal.pone.0232565.

88. Chaudhury, S., Lyskov, S., and Gray, J.J. (2010). PyRosetta: a script-based interface for implementing molecular modeling algorithms using Rosetta. Bioinformatics *26*, 689–691. https://doi.org/10.1093/bioinformatics/btq007.

89. Tegunov, D., and Cramer, P. (2019). Real-time cryo-electron microscopy data preprocessing with Warp. Nat. Methods *16*, 1146–1152. https://doi.org/10.1038/s41592-019-0580-y.

90. Rohou, A., and Grigorieff, N. (2015). CTFFIND4: Fast and accurate defocus estimation from electron micrographs. J. Struct. Biol. *192*, 216–221. https://doi.org/10.1016/j.jsb.2015.08.008.

91. Bepler, T., Morin, A., Rapp, M., Brasch, J., Shapiro, L., Noble, A.J., and Berger, B. (2019). Positive-unlabeled convolutional neural networks for particle picking in cryo-electron micrographs. Nat. Methods *16*, 1153–1160. https://doi.org/10.1038/s41592-019-0575-8.

92. Echols, N., Grosse-Kunstleve, R.W., Afonine, P.V., Bunkóczi, G., Chen, V.B., Headd, J.J., McCoy, A.J., Moriarty, N.W., Read, R.J., Richardson, D.C., et al. (2012). Graphical tools for macromolecular crystallography in PHENIX. J. Appl. Crystallogr. *45*, 581–586. https://doi.org/10.1107/S0021889812017293.

93. Schindelin, J., Rueden, C.T., Hiner, M.C., and Eliceiri, K.W. (2015). The ImageJ ecosystem: an open platform for biomedical image analysis. Mol. Reprod. Dev. *82*, 518–529. https://doi.org/10.1002/mrd.22489.

94. Carpenter, A.E., Jones, T.R., Lamprecht, M.R., Clarke, C., Kang, I.H., Friman, O., Guertin, D.A., Chang, J.H., Lindquist, R.A., Moffat, J., et al. (2006). CellProfiler: image analysis software for identifying and quantifying cell phenotypes. Genome Biol. *7*, R100. https://doi.org/10.1186/gb-2006-7-10-r100.

95. Stirling, D.R., Swain-Bowden, M.J., Lucas, A.M., Carpenter, A.E., Cimini, B.A., and Goodman, A. (2021). CellProfiler 4: improvements in speed, utility and usability. BMC Bioinformatics *22*, 433. https://doi.org/10.1186/s12859-021-04344-9.

96. Fontana, M., Fijen, C., Lemay, S.G., Mathwig, K., and Hohlbein, J. (2018). High-throughput, non-equilibrium studies of single biomolecules using glass-made nanofluidic devices. Lab Chip *19*, 79–86. https://doi.org/10.1039/C8LC01175C.

97. Srivatsan, S.R., McFaline-Figueroa, J.L., Ramani, V., Saunders, L., Cao, J., Packer, J., Pliner, H.A., Jackson, D.L., Daza, R.M., Christiansen, L., et al. (2020). Massively multiplex chemical transcriptomics at single-cell resolution. Science *367*, 45–51. https://doi.org/10.1126/SCIENCE.AAX6234.

98. Hao, Y., Hao, S., Andersen-Nissen, E., Mauck, W.M., 3rd, Zheng, S., Butler, A., Lee, M.J., Wilk, A.J., Darby, C., Zager, M., et al. (2021). Integrated analysis of multimodal single-cell data. Cell *184*, 3573–3587.e29. https://doi.org/10.1016/j.cell.2021.04.048.

99. Leutert, M., Rodríguez-Mias, R.A., Fukuda, N.K., and Villén, J. (2019). R2-P2 rapid-robotic phosphoproteomics enables multidimensional cell signaling studies. Mol. Syst. Biol. *15*, e9021. https://doi.org/10.15252/msb.20199021.

100. Navarrete-Perea, J., Yu, Q., Gygi, S.P., and Paulo, J.A. (2018). Streamlined Tandem Mass Tag (SL-TMT) Protocol: An Efficient Strategy for Quantitative (Phospho)proteome Profiling Using Tandem Mass Tag-Synchronous Precursor Selection-MS3. J. Proteome Res. *17*, 2226–2236. https://doi.org/10.1021/acs.jproteome.8b00217.

101. Schweppe, D.K., Eng, J.K., Yu, Q., Bailey, D., Rad, R., Navarrete-Perea, J., Huttlin, E.L., Erickson, B.K., Paulo, J.A., and Gygi, S.P. (2020). Full-Featured, Real-Time Database Searching Platform Enables Fast and Accurate Multiplexed Quantitative Proteomics. J. Proteome Res. *19*, 2026–2034. https://doi.org/10.1021/acs.jproteome.9b00860.

102. Eng, J.K., Jahan, T.A., and Hoopmann, M.R. (2013). Comet: an open-source MS/MS sequence database search tool. Proteomics *13*, 22–24. https://doi.org/10.1002/pmic.201200439.

103. Rad, R., Li, J., Mintseris, J., O'Connell, J., Gygi, S.P., and Schweppe, D.K. (2021). Improved Monoisotopic Mass Estimation for Deeper Proteome Coverage. J. Proteome Res. *20*, 591–598. https://doi.org/10.1021/acs.jproteome.0c00563.

STAR★METHODS

KEY RESOURCES TABLE

REAGENT or RESOURCE	SOURCE	IDENTIFIER
Antibodies		
Monoclonal Rabbit anti-phospho-p44/42 MAPK (Erk 1/2) (Thr202/Tyr204)	Cell Signaling	Cat# 4370S; RRID: AB_2315112
Polyclonal Rabbit anti-p44/42 MAPK (Erk 1/2)	Cell Signaling	Cat# 9102; RRID: AB_330744
Polyclonal Rabbit anti-phospho-FGF Receptor (Tyr653/654)	Cell Signaling	Cat# 3471; RRID: AB_331072
Monoclonal Rabbit anti-FGF Receptor 1 (D8E4)	Cell Signaling	Cat# 9740; RRID: AB_11178519
Monoclonal Rabbit Anti-S6 Ribosomal Protein	Cell Signaling	Cat# 2217S; RRID: AB_331355
Monoclonal Mouse anti-phospho-p44/42 MAPK (ERK 1/2) (pT202/Y204) - AlexaFluor488	BD Biosciences	Cat# 612592; RRID: AB_399875
Goat Anti-Rabbit IgG (H+L) - HRP Conjugate	Bio-Rad	Cat# 1706515; RRID: AB_615912
Monoclonal Mouse anti-CD31 (PECAM-1)	Cell Signaling	Cat# 3528; RRID: AB_2160882
Monoclonal Rabbit anti-PDGFR β (28E1)	Cell Signaling	Cat# 3169; RRID: AB_2162497
Goat anti-Mouse IgG secondary antibody, Alexa Fluor 633	Invitrogen	Cat# A-21050; RRID: AB_2535718
Goat anti-Rabbit IgG secondary antibody, Alexa Fluor 488	Invitrogen	Cat# A-11008; RRID: AB_143165
Anti-Hu CD144 (VE-Cadherin) APC	eBioscience	Cat# 17-1449-42; RRID: AB_10804754
APC anti-human CD140b (PDGFR-B)	BioLegend	Cat# 323608; RRID: AB_2162787
Anti-NG2, Alexa Fluor 488 Conjugate	EMD Millipore	Cat# AB5320A4; RRID: AB_11203143
Polyclonal Anti-Claudin 5 Antibody (Rb)	Abcam	Cat# 15106; RRID: AB_301652
PE Anti-alpha smooth muscle actin	Abcam	Cat# 208844; RRID: AB_11129103
Recombinant anti-VCAM1 antibody	Abcam	Cat# 134047; RRID: AB_2721053
VE-Cadherin (D87F2) Rabbit mAb	Cell Signaling	Cat# 2500; RRID: AB_10839118
Purified Rat Anti-Mouse CD31	BD Biosciences	Cat# 557355; RRID: AB_396660
Bacterial and virus strains		
E.coli BL21 (DE3)	NEB	Cat# C2527H
Chemicals, peptides, and recombinant proteins		
Fetal Bovine Serum (FBS)	Biowest	Cat# S1620
Penicillin-Streptomycin	Gibco	Cat# 1514012
GlutaMAX Supplement	Gibco	Cat# 35050061
Sodium Pyruvate (100mM)	Gibco	Cat# 11360070
HEPES (1M)	Gibco	Cat# 15630130
Heparin sodium salt	Fisher BioReagents	Cat# 9041-08-1
Amphotericin B	Gibco	Cat# 15290018
Gelatin from porcine skin	Sigma-Aldrich	Cat# G1890-100
Sodium Chloride	Fisher Chemical	Cat# 7647-14-5
Hydrochloric Acid	Sigma-Aldrich	Cat# 320331
Streptomycin Sulfate	Sigma-Aldrich	Cat# S9137
Puromycin Dihydrochloride	Gibco	Cat# A11138-03
Recombinant Human FGF-basic	Peprotech	Cat# 100-18B

(*Continued on next page*)

Continued

REAGENT or RESOURCE	SOURCE	IDENTIFIER
Tris-HCl	Sigma-Aldrich	Cat# 1185-53-1
Glycerol	Sigma-Aldrich	Cat# G5516
Triton X-100	Sigma-Aldrich	Cat# 9002-93-1
Sodium dodecyl sulfate (SDS)	Sigma-Aldrich	Cat# 151-21-3
B-Glycerol phosphate	Sigma-Aldrich	Cat# 50020-100G
Sodium Fluoride (NaF)	Sigma-Aldrich	Cat# 7681-49-4
Sodium Pyrophosphate	Sigma-Aldrich	Cat# 13472-36-1
Sodium Orthovanadate	Sigma-Aldrich	Cat# 13721-39-6
Phenylmethylsulfonyl fluoride (PMSF)	Roche Life Sciences	Cat# 329-98-6
Benzonase Nuclease	EMD	Cat# 70664
Protease Inhibitor Tablets	Thermo Fisher Scientific	Cat# A32963
Phosphatase inhibitor cocktail 2	Sigma-Aldrich	Cat# P5726
4X Laemmli Sample Buffer	Bio-Rad	Cat# 1610747
2-Mercaptoethanol	Sigma-Aldrich	Cat# M7522-100
Calbryte 520 AM	AAT Bioquest	Cat# 20651
Heparin Oligosaccharide dp10	Iduron	Cat# H010
Bovine Serum Albumin (BSA)	VWR	Cat# 0332-500G
Vectashield with DAPI	Vector laboratories	Cat# H-2000-2
GSK3-Inhibitor (CHIR99021)	Cayman Chemicals	Cat# 13122
Growth Factor Reduced Matrigel	Corning	Cat# 356231
Recombinant Human/Murine/Rat Activin A	Peprotech	Cat# 120-14P
Recombinant Human BMP-4	R&D Systems	Cat# 314-BP-010
B27 supplement, minus insulin	Thermo Fisher Scientific	Cat# A1895601
Recombinant Human VEGF	R&D Systems	Cat# 293-VE-050
L-Ascorbic Acid	Sigma-Aldrich	Cat# A8960
1-Thioglycerol	Sigma-Aldrich	Cat# M6145
NaN3 sodium azide	EMD Millipore	Cat# 26628-22-8
Human TNF-a Recombinant Protein	Gibco	Cat# PHC3011
KnockOut Serum Replacement	Gibco	Cat# 10828028
MEM Non-Essential Amino Acids solution (100X)	Gibco	Cat# 11140050
Y-27632 ROCK Inhibitor	Tocris Bioscience	Cat# 1254
SB-431542	Miltenyi Biotec	Cat# 130-106-275
Acetonitrile	VMR	Cat# BDH83639.400
Formic acid	Fisher Scientific	Cat# A117-50
Alexa Fluor™ 568 Phalloidin	Invitrogen	Cat# A12380
De novo designed oligomeric proteins	This paper	Table S10
Critical commercial assays		
BD Cytofix Buffer	BD Biosciences	Cat# 554655
BD Phosflow PERM buffer	BD Biosciences	Cat# 558050
BD BSA stain Buffer	BD Biosciences	Cat# 554657
Illumina P3 100 cycle kit	Illumina	Cat# 20040559
Illumina P2 100 cycle kit	Illumina	Cat# 20046811
LDL Uptake Assay Kit - Cell Based	Abcam	Cat# 287862
TMTpro	Thermo Fisher Scientific	Cat# A52045
Deposited data		
Cryo-EM Map of C4-131	This paper	EMDB: EMD-28958
Cryo-EM Map of C4-71	This paper	EMDB: EMD-28974

(*Continued on next page*)

Continued

REAGENT or RESOURCE	SOURCE	IDENTIFIER
Cryo-EM Map of C4-71_6x	This paper	EMDB: EMD-28966
Cryo-EM Map of C4-71_8x	This paper	EMDB: EMD-28967
Cryo-EM Map of C4-81	This paper	EMDB: EMD-28973
Cryo-EM Map of C6-71	This paper	EMDB: EMD-28968
Cryo-EM Map of C6-71_6x	This paper	EMDB: EMD-28969
Cryo-EM Map of C6-71_8x	This paper	EMDB: EMD-28970
Cryo-EM Map of C6-79	This paper	EMDB: EMD-28889
Cryo-EM Map of C8-71	This paper	EMDB: EMD-28888
Cryo-EM Map of C8-71_6x	This paper	EMDB: EMD-28971
Cryo-EM Map of C8-71_8x	This paper	EMDB: EMD-28972
Atomic Model of C6-79	This paper	PDB: 8F6R
Atomic Model of C8-71	This paper	PDB: 8F6Q
RNA Sequencing Data	This paper	Harvard Dataverse: https://doi.org/10.7910/dvn/jivgf2, https://doi.org/10.7910/dvn/80rttv, https://doi.org/10.7910/dvn/hmcsib
Proteomic Mass Spectrometry Data	This paper	Zenodo: https://doi.org/10.5281/zenodo.11099790
Protein design models	This paper	Zenodo: https://doi.org/10.5281/zenodo.11095779
Experimental models: Cell lines		
WTC-11 human induced pluripotent stem cells	Coriell	Cat# GM25256
HUVEC (pooled donor) endothelial cells	Lonza	Cat# CC-2519
Chinese Hamster Ovary cells (CHO) (pgsD-677 cells) stably expressing FGFR1c (CHO-R1c)	ATCC; Modified cells were gift from Schlessinger Lab	Based on Cat# CRL-2244
Rat Myoblast (L6) stably expressing FGFR1c (L6-R1c)	ATCC; Modified cells were gift from Sangwon Lee Lab[21]	Based on Cat# CRL-1458
Rat Myoblast (L6) stably expressing FGFR1b (L6-R1b)	ATCC; Modified cells were gift from Sangwon Lee Lab[21]	Based on Cat# CRL-1458
Experimental models: Organism/strains		
NOD.CB17-Prkdscid/J	Jackson Laboratories	RRID:IMSR_JAX:001303
Oligonucleotides		
q-RT-PCR Primer Sequences	Integrated DNA Technologies	Table S8
Hash Oligonucleotides for single cell RNA-seq	Integrated DNA Technologies	Table S9
Recombinant DNA		
pET-29b(+)	Integrated DNA Technologies	https://www.addgene.org/vector-database/2569/
Software and algorithms		
Rosetta	Leman et al.[69]	https://www.rosettacommons.org/software
Cyclic Docking Protocol	Fallas et al.[20] and Sheffler et al.[27]	https://github.com/willsheffler/rpxdock
Relion 3.1	Zivanov et al.[70]	https://relion.readthedocs.io/en/release-3.1/
cryoSPARC v3	Punjani et al.[71]	https://cryosparc.com/
EMAN2	Bell et al.[72]	https://blake.bcm.edu/emanwiki/EMAN2
Sparx	Hohn et al.[73]	https://sparx-em.org/
FrameSlice	Dyer et al.[32]	https://sibyls.als.lbl.gov/ran/instructions

(*Continued on next page*)

Continued

REAGENT or RESOURCE	SOURCE	IDENTIFIER
ScÅtter	Dyer et al.[32]	https://bl1231.als.lbl.gov/scatter/
FOXS server	Schneidman-Duhovny et al.[74]	https://modbase.compbio.ucsf.edu/foxs/
Leginon	Suloway et al.[75]	www.leginon.org
MotionCor2	Zheng et al.[76]	https://msg.ucsf.edu/software
Appion	Lander et al.[77]	www.appion.org
3DFSC server	Tan et al.[78]	https://3dfsc.salk.edu/
UCSF Chimera	Pettersen et al.[79]	https://www.cgl.ucsf.edu/chimera/
Phenix v1.16	Adams et al.[80]	www.phenix-online.org
COOT	Emsley et al.[81]	https://www2.mrc-lmb.cam.ac.uk/personal/pemsley/coot/
Octet Analysis Studio	Sartorius	https://www.sartorius.com/en/products/biolayer-interferometry/octet-systems-software
MATLAB	Mathworks	https://www.mathworks.com/
GaussStorm	Holden et al.[82]	https://kapanidis.web.ox.ac.uk/software
R Studio	Posit	www.posit.co
flowCore	Ellis et al.[83]	https://bioconductor.org/packages/flowCore/
Origin Pro 9.1	OriginLab	www.originlab.com
GraphPad Prism 9	Dotmatics	www.graphpad.com
Fiji	Schindelin et al.[84]	https://imagej.net/ij/
Monocle3	Trapnell et al.[85]	https://cole-trapnell-lab.github.io/monocle3/
Adobe Illustrator	Adobe	https://www.adobe.com/products/illustrator.html
CellProfiler	Carpenter et al.[70]	www.cellprofiler.org
Angiogenesis Analyzer tool	Carpentier et al.[86]	https://biii.eu/angiogenesis-analyzer-imagej
Wound Healing tool	Suarez-Arnedo et al.[87]	https://biii.eu/wound-healing-tool
FlowJo Software	BD Life Sciences	https://www.flowjo.com/solutions/flowjo
Imaris Microscopy Image Analysis Software (Version 9.9)	Oxford Instruments	https://imaris.oxinst.com/
Custom code	This paper	https://github.com/ashx56/FGF_Oligomer_2024
Other		
Formvar/carbon 400 mesh copper grids	Ted Pella	Cat# 01754-F

RESOURCE AVAILABILITY

Lead contact

Further information and requests for resources and reagents should be directed to and will be fulfilled by the lead contact, Hannele Ruohola-Baker (hannele@uw.edu).

Materials availability

Sequences for the generated de novo designed oligomers from this study are published in Table S10 and the designed proteins are available upon request.

Data and code availability

- The coordinates of the atomic models have been deposited in the Protein Data Bank under accession codes PDB: 8F6R and 8F6Q (C6-79 and C8-71).
- The cryo-EM maps have been deposited in the Electron Microscopy Data Bank with accession codes EMDB: EMD-28958 (C4-131), EMDB: EMD-28974 (C4-71), EMDB: EMD-28966 (C4-71_6x), EMDB: EMD-28967 (C4-71_8x), EMDB: EMD-28973

(C4-81), EMDB: EMD-28968 (C6-71), EMDB: EMD-28969 (C6-71_6x), EMDB: EMD-28970 (C6-71_8x), EMDB: EMD-28889 (C6-79), EMDB: EMD-28888 (C8-71), EMDB: EMD-28971 (C8-71_6x), and EMDB: EMD-28972 (C8-71_8x).

- Raw and processed files for Bulk and Single-cell RNA-seq experiments have been deposited at Harvard Dataverse and are publicly available as of the date of publication. Accession numbers are listed in the key resources table.
- Proteomic Mass Spectrometry data have been deposited at Zenodo and are publicly available as of the date of publication. Accession numbers are listed in the key resources table.
- Protein design models are available in a Zenodo repository and are publicly available as of the date of publication. Accession numbers are listed in the key resources table.
- All original code has been deposited at https://github.com/ashx56/FGF_Oligomer_2024 and is publicly available as of the date of publication.
- Any additional information required to reanalyze the data reported in this paper will be shared by the lead contact upon request.

EXPERIMENTAL MODEL AND STUDY PARTICIPANT DETAILS

Cell lines

Cells were cultured under standard conditions on cell culture grade plastic dishes or flasks at 37°C enriched with 5% CO_2 in incubators and generally passaged when cells reached confluency.

Chinese Hamster Ovary cells (CHO - pgsD-677 cells) stably expressing FGFR1c (Gift from the Schlessinger Lab) were maintained in F-12K medium [ATCC, #30-2004] supplemented with 10% Fetal Bovine Serum, 1% Penicillin-Streptomycin, and 10 μg/mL Puromycin [Gibco, #A11138-03].

Rat myoblast (L6) cells [ATCC, #CRL-1458] stably expressing either human FGFR1c (L6-R1c) or FGFR1b (L6-R1b)[21] (Gift from the Sangwon Lee Lab) were maintained in DMEM medium [Gibco, #10566] supplemented with 10% Fetal Bovine Serum, 1% Penicillin-Streptomycin, and 10 μg/mL Puromycin.

Human umbilical vein endothelial cells (HUVECs) were obtained from Lonza, Germany (#CC-2519). Cells were grown in EGM2 media (20% Fetal Bovine Serum [BioWest, #S1620], 1% Penicillin-Streptomycin [Gibco, #1514012], 1% Glutamax [Gibco #35050061], 1% ECGS (Endothelial Cell Growth Supplement), 1mM Sodium Pyruvate [Gibco, #11360070], 7.5mM HEPES [Gibco, #15630130], 0.08mg/mL Heparin [Fisher BioReagents, #9041-08-1], 0.01% Amphotericin B [Gibco, #15290018], a mixture of 1X RPMI 1640 +/- glucose [Gibco, #1187902] for a final concentration of 5.6mM glucose; filtered through 0.2-μm filter) on 0.1% gelatin-coated [Sigma, #G1890-100] 35mm cell culture dishes. Details about assays performed with these cells can be found in the method details section.

WTC-11 human induced pluripotent stem cells (Coriell, Cat# GM25256) were used for blood vessel organoid and endothelial cell differentiation. For endothelial cell differentiation, hiPSCs (WTC-11 human induced pluripotent stem cells) [Coriell, #GM25256] were seeded on 24-well plates coated with growth factor-reduced Matrigel [Corning, #356231] and cultured in mTeSR1 stem cell medium [StemCell Technologies, #85850] until cells reach confluence with media changes daily. Details about differentiation conditions, performed assays with differentiated endothelial and perivascular cells as well as blood vessel organoid formation can be found in the method details section.

Animals

All animal studies were conducted in accordance with all relevant ethical regulations under protocols approved by the Institutional Animal Care and Use Committee at the University of Washington in Seattle. NOD-SCID mice (RRID:IMSR_JAX:001303), adult males 8-10 weeks old were utilized for the experiments. Mice were maintained on a standard diet under standard pathogen-free housing conditions, with food and water freely available.

METHOD DETAILS

Scaffold selection and cyclic docking

Subunit scaffolds consisted of a set of 18 monomeric designed repeat proteins with high-resolution crystal structures or SAXS data.[25,26] PDB IDs for designs with crystal structures are provided in Table S1. Docking was performed as previously described.[20] Briefly, the protocol aligns subunits along the desired symmetry axis and scores these using a residue pair-motif database derived from PDB structures. This resulted in 829 outputs among all 5 symmetries attempted (C4, C5, C6, C7, and C8). Outputs were then sequence designed by Rosetta FastDesign to generate an oligomeric interface. These design outputs were filtered by ΔΔG (between -35 and -70), solvent accessible surface area (SASA > 700 A^2), shape complementarity (sc > 0.65), and fewer than 2 unsatisfied hydrogen bonds. This resulted in 150 outputs, which were then visually screened for geometric redundancy. Docking for alternative symmetries was performed as above without the interface design step.

5 helix concave scaffold generation

5 helix concave scaffolds (5HCS) are small curved repeat proteins. The backbones were designed by helical extension based on a library of short helical and loop fragments clustered to include only the most common and ideal fragments. These fragments were

pieced together using a published helical extension method to create helix-turn-helix-turn modules that were repeated 5 times to generate 5 repeat DHR-like proteins (manuscript in preparation).[30]

Repeat extension script

DHR-based oligomers were extended using a custom PyRosetta[88] script that uses an align-and-replace approach. To extend an oligomer with accessible N-termini by two repeats, the second repeat of the 4-repeat parent DHR was aligned to the N-terminal repeat of the oligomer. Subsequently, the terminal repeat of the oligomer was replaced by repeats 2 to 4 of the parent DHR. For oligomers with accessible C-termini the third repeat of the 4-repeat parent DHR was aligned to the C-terminal repeat of the oligomer, and the C-terminal repeat of the oligomer was replaced by repeats 1 to 3 of the parent DHR. The process was repeated to achieve additional extensions.

Expression and purification

Sequences of the designed proteins were reverse translated with optimization for *Escherichia coli* expression, with a C-terminal glycine-serine linker followed by a 6x histidine tag. Sequences were ordered as synthetic genes from Integrated DNA Technologies within the pET29b+ vector between NdeI and XhoI cloning sites. This vector contains a kanamycin resistance marker and a T7 promoter. Plasmids were transformed into *E. coli* BL21 (DL3) competent cells and plated on LB with kanamycin at 50mg/L. Transformants were inoculated into 50mL of autoinduction expression media (for 1L: 12g tryptone, 24g yeast extract, 20 mL 50×M, 20 mL 50x5052, 2 mL 1M MgSO4, 200 μL Studier Trace metals, 100 μg kanamycin, q.s. to 1L with filtered water) in a 250mL flask. Expression cultures were grown for 20 hours at 37°C with 200rpm shaking. Cells were pelleted by centrifugation at 4000xg and resuspended in a lysis buffer consisting of 25mM Tris pH 8, 300mM NaCl, and 20mM imidazole with added protease inhibitor and DNase. Cells were lysed by sonication at 85% amplitude with 8 x 15 second pulses. Lysate was separated into soluble and insoluble fractions by centrifugation at 18,000xg. Immobilized metal affinity chromatography (IMAC) was used to purify designed protein. Nickel-nitrilotriacetic acid (Ni-NTA) resin was initially equilibrated with 5 column volumes (CV) lysis buffer. Supernatant was poured over the columns, followed by 20CV wash buffer (25mM Tris pH 8, 400mM NaCl, 30mM imidazole). Protein was eluted using 5CV elution buffer (25mM Tris pH 8, 300mM NaCl, 500mM imidazole). Eluate was purified by size exclusion chromatography (SEC) on an AKTA PURE FPLC system, using either a Superose 6 Increase 10/300 GL column or a Superdex 200 Increase 10/300 GL column, with Tris-buffered saline (TBS; 25mM Tris pH 8, 150mM NaCl) at a speed of 0.75mL/min. Fractions corresponding to the peak trace were collected and combined for further analysis. Sequences of all proteins produced in the study can be found in Table S10.

Low-endotoxin protein production

Genes were expressed as described above. Cultures were resuspended and lysed in a phospho-buffered saline (PBS)-based lysis buffer with added protease inhibitor and DNase. Cells were sonicated and pelleted as described above. Supernatant was filtered through a 0.45μm filter prior to loading onto IMAC columns. IMAC columns were pre-washed with PBS + 1% Triton X-100 + 0.75% CHAPS to remove any residual endotoxin and equilibrated with PBS + 5 mM imidazole. Supernatant was poured onto the column and followed by washing with 5CV PBS + 30 mM imidazole. To remove endotoxin, 4 wash steps were performed using 5CV PBS + 1% Triton X-100 + 0.75% CHAPS, with 30 min 37 °C incubations on the first and third wash. This was followed by 2 washes with 10CV PBS, then elution with 5CV PBS + 400 mM imidazole. SEC was performed as described above on a dedicated AKTA PURE FPLC with lines, loops, and fraction dispenser pre-washed using 500mM NaOH + 0.75% CHAPS. Endotoxin levels were measured with the LAL endotoxin testing system (Charles River Laboratories).

Proteins expressed by the General Protein Production core were transformed as above then a pre-culture was inoculated into 50mL of LB media and grown at 37°C for 18 hours. 10mL of this pre-culture was used to inoculate 500mL of autoinduction expression media (recipe above) in a 2L flask. Cells were lysed using a Microfluidics M-110P microfluidizer. Soluble and insoluble portions of the lysate were separated at 17000g. Supernatant was flown over 3 mL of nickel resin and washed with PBS wash buffer (20 mM NaPO4, 300 mM NaCl, 30 mM Imidazole, 0.75% CHAPS) for 6 washes of 10mL each (a total of 60 mL). SEC was performed as described above. Endotoxin levels were measured as above.

Size exclusion chromatography with multi-angle light scattering

Samples were run in TBS (50mM Tris-HCL, 150mM NaCl pH 8.0) at 1mL/min over a Superose 6 10/300 GL column using an Agilent 1260 HPLC. The HPLC is in line with a Heleos multi-angle static light scattering and Optilab T-rEX detector (Wyatt Technology Co.). Using ASTRA (Wyatt Technology Co.), a weighted average molecular weight (Mw) and number average molar mass (Mn) were calculated to determine monodispersity-by-polydispersity index (PDI), with PDI = Mw/Mn.

Negative stain EM grid preparation, data collection, and data processing

Proteins were diluted to 20 μg/ml in TBS, then immediately applied to freshly glow-discharged Formvar/carbon 400 mesh copper grids (Ted Pella catalog #01754-F). After incubation for 45s, excess protein solution was removed by blotting from the side with filter paper, then grids were inverted onto two successive drops of sample buffer followed by three to five successive drops of 2% uranyl formate, with excess solution removed by blotting after each application. The final stain applied was incubated for 15s before blotting. Air-dried grids were imaged using a FEI Talos L120C TEM equipped with a 4K × 4K Gatan OneView camera, at a nominal

magnification of 73,000x and pixel size of 2.0 Å. Micrographs were imported to Relion 3.1[70] and/or cryoSPARC v2[71] and, after picking using automated protocols in each program, particles were subjected to 2D classification. Design model projections were generated using EMAN2[72] and Relion, and projections were aligned with experimental 2D class averages using Sparx.[73]

Small-angle X-ray scattering

SEC-purified samples were prepared for small-angle X-ray scattering (SAXS) by concentrating (if needed) with a 10K molecular weight cut-off spin concentrator followed by filtration with a 0.22μm spin filter. Samples were sent in low (1mg/mL) and high (3-5mg/mL) concentrations in TBS, with flow-through from concentrators used as blanks for later buffer subtraction during data analysis. Scattering data were collected at the SIBYLS High Throughput SAXS Advanced Light Source in Berkeley, California[33,34] and analyzed with FrameSlice and ScÅtter software packages.[32] Experimental data were compared to design model predictions using the FOXS server (https://modbase.compbio.ucsf.edu/foxs/).[74] For samples with clear deviation from the design model and indication of off-target symmetry by SEC-MALS and electron microscopy, data were additionally compared to a theoretical design model of the off-target symmetry (described above).

Cryo-EM grid preparation and data collection

All grids were plunge-frozen into liquid ethane using a Vitrobot Mark IV with a chamber maintained at 100% humidity and 22°C. Prior to plunge-freezing, 3.5 μL of each design at 0.1 - 1.0 mg/ml was applied to freshly glow-discharged grids of the following types: QUANTIFOIL R 1.2/1.3 on Cu 400 mesh grids (C6-79), QUANTIFOIL R 1.2/1.3 on Cu 400 mesh grids + graphene oxide (C8-71; Electron Microscopy Sciences cat. #GOQ400R1213Cu), and/or QUANTIFOIL R 2/2 on Cu 300 mesh grids + 2 nm C (C4-71 and extensions, C4-81, C8-71 and extensions, C6-71 and extensions, and C4-131). All grids were first screened at NYU on a Talos Arctica microscope operated at 200 kV with a Gatan K3 camera. Larger datasets were acquired for C4-71, C4-81, C6-79, and C8-71 on a Titan Krios microscope operated at 300 kV with a Gatan K3 camera and BioQuantum energy filter ("Krios 6" operated by NCCAT at the New York Structural Biology Center). In both imaging setups, data acquisition was controlled via Leginon[75] and pre-processing (including motion correction and 2X binning) was performed with MotionCor2 as integrated in Appion.[76,77] Further data collection parameters are shown in Table S4.

Some designs exhibited preferred orientation that appeared to be correlated with ice thickness: in thicker (>30-40nm) ice, side views of the ring predominated, whereas top views (looking down the symmetry axis) could be seen only in the thinnest ice (15-20 nm, as measured by aperture-limited scattering). In such cases, and where grid quality allowed, data were collected in a range of ice thicknesses to minimize orientation bias.

Processing of 200 kV cryo-EM screening datasets (C4-71 extensions, C6-71 and extensions, C8-71 extensions)

Aligned, dose-weighted micrographs and STAR files for particles picked "on the fly" with Warp[89] were imported to cryoSPARC[71] v.3 for CTF estimation,[90] particle picking, 2D classification, and 3D classification/refinement. 2D classification of particles imported from Warp was used to identify suitable starting classes for template-based auto-picking. In cases where Warp picking did not yield meaningful templates (or omitted certain particle views), unrepresented particle views were located using manual and/or blob picking and classified in 2D to generate additional templates for auto-picking. Initial maps were generated from 2D-curated particles by *ab initio* reconstruction in C1 followed by iterative rounds of heterogeneous and homogeneous refinement. Global resolution (using independent half-maps from refinement and FSC = 0.143 threshold) was estimated using the 3DFSC server (https://3dfsc.salk.edu/).[78] Additional processing details for each dataset are shown in Table S5.

Processing of 300 kV cryo-EM datasets (C4-71, C4-81, C6-79, C8-71)

Detailed processing workflows are shown in Figures S9 and S10. For all 300 kV datasets, aligned and dose-weighted micrographs were imported to cryoSPARC v.2/v.3 for CTF estimation, particle picking, 2D classification, and initial 3D curation and refinement. Templates for C6-79 auto-picking were generated using cryoSPARC's "blob picker". For C4-81, C4-71, and C8-71, 2D averages generated from cryo-EM pre-screening data were used for initial template-based auto-picking. Template-based auto-picking of the C8-71 ring was dominated by side views; to retain top views during auto-picking and curation, these views were picked separately using a single auto-picking template generated from 2D classification of manually-picked top views. For C4-81 and C8-71, curated particles from template picking were used as a training set for Topaz[91] picking within cryoSPARC. The final sets of curated particles from cryoSPARC were imported to Relion v.3[70] for further 2D/3D classification and 3D refinement, which improved map quality for C4-71 and C4-81. Final 3D refinements were performed with the highest expected symmetry imposed, as well as in C1 and with lower-order symmetries imposed. For all datasets, imposing the highest designed circular symmetry improved map quality without introducing substantial artifacts. Global resolution (using independent half-maps from refinement and FSC = 0.143 threshold) and sphericity were estimated using the 3DFSC server (https://3dfsc.salk.edu/).[78] The FSC mask automatically tightened during the final round of homogenous refinement in cryoSPARC was used for resolution and sphericity calculations for C6-79 and C8-71. Additional processing details for each dataset are shown in Table S6.

C6-79 and C8-71 model building and refinement

De novo designed model coordinates for the C8-71 octamer were first docked into the cryo-EM map as a single rigid body using UCSF Chimera.[79] Initial fitting for C6-79 was performed in Chimera with six copies of the designed monomer manually placed

into the map, fit as six individual rigid bodies, and merged into a single set of coordinates for the hexamer. In PHENIX v.1.16,[80] docked coordinates were stripped of hydrogens using phenix.pdbtools and refined in real space using iterative rounds of phenix.real_space_refine and manual model adjustment in COOT.[81,92] For C8-71, a single instance of simulated annealing was performed at the beginning of automated refinement in PHENIX; non-crystallographic symmetry, secondary structure, Ramachandran, and rotamer restraints were enabled throughout. Additional density is present in the C8-71 cryo-EM maps near W113, at the interface between subunits of the octamer. In addition to the C8 map used for model refinement, this density is also visible at comparable thresholds in C1 and C4 maps refined from the same particles. As no obvious candidate molecule could be identified for this density, it was left unmodelled.

For C6-79, rigid-body refinement and a single instance of simulated annealing were used in early rounds of automated real-space refinement. Non-crystallographic symmetry, secondary structure, Ramachandran, and rotamer restraints were enabled throughout refinement. Additionally, the final round of phenix.real_space_refine included ADP refinement and reference model restraints (using the starting model as a reference to restrain residues 46-53 to manually-adjusted positions and strictly match rotamers). Additional model statistics are shown in Table S6.

Cell culture

Human umbilical vein endothelial cells (HUVECs) were obtained from Lonza, Germany (#CC-2519). Cells were grown in EGM2 media (20% Fetal Bovine Serum [BioWest, #S1620], 1% Penicillin-Streptomycin [Gibco, #1514012], 1% Glutamax [Gibco #35050061], 1% ECGS (Endothelial Cell Growth Supplement), 1mM Sodium Pyruvate [Gibco, #11360070], 7.5mM HEPES [Gibco, #15630130], 0.08mg/mL Heparin [Fisher BioReagents, #9041-08-1], 0.01% Amphotericin B [Gibco, #15290018], a mixture of 1X RPMI 1640 +/- glucose [Gibco, #1187902] for a final concentration of 5.6mM glucose; filtered through 0.2-μm filter) on 0.1% gelatin-coated [Sigma, #G1890-100] 35mm cell culture dishes. Cells were cryopreserved at passage 4 for later thawing and use in Western blots.

ECGS was extracted from 25 mature whole bovine pituitary glands [Pel-Freeze, #57133-2]. Pituitary glands were homogenized with ice-cold 0.15M NaCl [Fisher Chemical, #CAS 7647-14-5] and adjusted to pH 4.5 with HCl [Sigma-Aldrich, 320331]. Following 1hr centrifugation at 4°C, the supernatant (wine colored) was collected and adjusted to pH 7.6, followed by addition of 0.5g/100 mL of Streptomycin Sulfate [Sigma, #S9137]. The following day, the supernatant was centrifuged at 4,000 RPM for 1hr at 4°C. The supernatant was sterile filtered using a 0.45-μm filter and stored at -20°C.

Parental heparan-deficient Chinese hamster ovary (CHO) cells [pgsD-677 cells; ATCC, #CRL-2244] stably expressing human FGFR1c were maintained in F-12K medium [ATCC, #30-2004] supplemented with 10% Fetal Bovine Serum, 1% Penicillin-Streptomycin, and 10 μg/mL Puromycin [Gibco, #A11138-03]. Rat myoblast (L6) cells [ATCC, #CRL-1458] stably expressing either human FGFR1c (L6-R1c) or FGFR1b (L6-R1b)[21] were maintained in DMEM medium [Gibco, #10566] supplemented with 10% Fetal Bovine Serum, 1% Penicillin-Streptomycin, and 10 μg/mL Puromycin.

Treatment and protein isolation for Western blot and proteomics

For activation assays, cells were seeded onto 12-well plates and grown to ~80% confluence. Cells were serum-starved overnight in their respective media (F-12K for CHO cells, DMEM low glucose (1 g/L) [Gibco, 11885-084] for HUVEC, L6 cells). The following day, cells were stimulated with different concentrations of either recombinant FGF2 [Peprotech, #100-18B] or designed scaffolds at 37 °C for 15 min. Concentration is reported as the concentration of the oligomeric particle, not the mb7 domain; therefore, 10 nM of C4-71C_mb7 corresponds to 10 nM of C4 oligomer and 40 nM of mb7. Following treatment, cells were washed once with 1X PBS before harvesting total protein for analysis.

Cells were lysed with lysis buffer containing 20 mM Tris–HCl [Sigma-Aldrich, #1185-53-1] (pH 7.5), 150 mM NaCl, 15% Glycerol [Sigma-Aldrich, #G5516], 1% Triton-X [Sigma-Aldrich, #9002-93-1], 3% SDS [Sigma-Aldrich, #151-21-3], 25 mM b-Glycerophosphate [Sigma-Aldrich, #50020-100G], 50 mM NaF [Sigma-Aldrich, #7681-49-4], 10 mM Sodium Pyrophosphate [Sigma-Aldrich, #13472-36-1], 0.5% Sodium Orthovanadate [Sigma-Aldrich, #13721-39-6], 1% PMSF [Roche Life Sciences, #329-98-6], 25 U benzonase nuclease [EMD, #70664], protease inhibitor cocktail [Pierce Protease Inhibitor Mini Tablets, Thermo Scientific, #A32963], and phosphatase inhibitor cocktail 2 [Sigma-Aldrich, #P5726] in a tube. 4X Laemmli Sample Buffer [Bio-Rad, #1610747] containing 10% beta-mercaptoethanol [Sigma-Aldrich, #M7522-100] was added to the cell lysate and then heated at 95°C for 10 min. The boiled samples were either used immediately for Western blot analysis or stored at -80°C.

Western blotting

If frozen, protein samples were thawed and heated at 95 °C for 10 minutes. A 4-10% SDS-PAGE gel was loaded with 30uL of protein per well and separated for 30 min at 250V. Proteins were transferred onto a nitrocellulose membrane for 12 minutes using the semi-dry turbo transfer Western blot apparatus [Bio-Rad]; the membrane was then blocked in 5% bovine serum albumin (BSA) [VWR, #0332-500G] for 1 hour. The membrane was incubated with the appropriate primary antibodies on a rocker at 4°C overnight. The antibodies used in this study were pERK1/2 p44/42 [Cell Signaling, #4370S] at 1:1,000 dilution, S6 [Cell Signaling, #2217S] at 1:1,000 dilution, ERK1/2 p44/42 [Cell Signaling, #9102] at 1:1,000 dilution, Phospho-FGF Receptor (Tyr 653/654) [Cell Signaling, #3471] at 1:1,000 dilution, and FGF Receptor 1 (D8E4) [Cell Signaling, #9740] at 1:1,000 dilution. The next day, membranes were washed with 1X TBS-T (3 times, 10 min intervals) and incubated with the respective HRP-conjugated secondary antibody [BioRad, #1706515] (1:10,000 dilution in 5% BSA) at room temperature for 1 hour. All the membranes were washed with 1X TBS-T (3 times,

10 min intervals) after secondary antibody incubation, developed using a Chemiluminescence developer, and imaged using a Bio-Rad ChemiDoc Imager.

Calcium release assay

CHO-R1c cells were seeded on 96-well flat bottom microplates [Corning, #3603] and grown to ~70-80% confluence. Cells were starved in serum-free F12-K medium for 3 hours. Following starvation, the cells were incubated in serum-free media containing 5μM Calbryte 520 AM fluorescent intracellular calcium indicator [AAT Bioquest, #20651] for 30 min at 37°C. Cells were washed 3X with serum-free media and treated with various concentrations of recombinant FGF2 (with or without 40μg/mL Heparin [Iduron, #H010]) or designed scaffolds. Confocal live imaging was done on a Nikon Yokogawa W1 spinning disk confocal microscope using a 20X objective. Parameters for each live frame: Excitation/Emission filters for GFP fluorescence, Exposure time of 150ms, Acquisition rate of 5 sec/frame, and total recording time of 20 minutes (5 min baseline recording + 15 min ligand treatment time). Images were processed with Fiji software distribution of ImageJ v1.52i[84,93] and frame-by-frame cellular fluorescence intensity was tracked and quantified with CellProfiler.[94,95] Dose-specific average calcium release was calculated by tracking each individual cell's response during the recording time and computing the mean peak fluorescence achieved by all cells in the frame. An average of 50-100 cells were tracked per recording.

Phosphoflow assay

CHO-R1c cells were grown in T75 flasks. One day before the experiment, cells were changed to starvation medium (F12K+P/S). On the day of the experiment, cells were washed, trypsinized, plated at 200k cells per well in a 96-well plate and incubated with ligands at corresponding concentrations for 15 min in starvation conditions at 37 °C in 100 μl. Afterwards cells were immediately fixed with 100 μl of prewarmed BD Cytofix buffer (BD Biosciences, #554655) and incubated at 37 °C for 10 min. Cells were spun down by centrifugation for 5 min at 300xg and supernatant was discarded by inverting the plate. The plate was gently vortexed, 100 μl of BD Phosflow PERM buffer (BD Biosciences, #558050) was added and cells were incubated for 30 min in the dark on ice. After the incubation, cells were washed twice with 200 μl of BSA stain buffer (BD Bioscience, #554657). After the washing steps, cells were resuspended in 100 μl of 1:10 diluted pERK-AlexaFluor488 (BD Biosciences, #612592) in BSA stain buffer and incubated for 30 min at RT in the dark. Cells were washed twice with 200 μl of BSA stain buffer and after final resuspension in 200 μl of BSA stain buffer immediately analyzed with the Attune flow cytometer. For analysis FSC, SSC and AlexaFluor488 laser settings were set to 1, 250 and 330. The plate autosampler was run at 100 μl/min and cells were gated to a single cell population and geometric mean of the population was calculated and plotted via Origin Pro 9.1. Data were fit using a Hill function in Origin. Data were normalized on 10 nM of FGF (ThermoFisher Scientific, #PHG0369) stimulation.

Biolayer interferometry (BLI) assay

BLI measurements were performed with the Sartorius Octet system. Streptavidin harboring tips were incubated in Octet Buffer for 30 min before the measurement. For the measurement, tips were equilibrated in Octet Buffer for 150 s, then biotinylated FGFR2 (ectodomain residues 147-366, UniProt ID: P21802, previously expressed in mammalian cells using a IgK signal peptide (METDTLL LWVLLLWVPGSTG) at the N-terminus and a C-terminal TEV cleavage site, 6-His and Avitag (GSENLYFQGSHHHHHHGSGL NDIFEAQKIEWHE)) was loaded onto the tips at 30 nM for 300 s. After a brief equilibration in Octet Buffer for 300 s, tips were dipped into different concentrations of ligands for association for 1400-1800 s. Dissociation was performed for 1400 s in Octet Buffer. Data were analyzed and fit via the Octet Analysis Software.

TIRF microscopy

For single-molecule imaging experiments, pgsD-677 cells were plated on 35-mm glass-bottom dishes (MatTek Corporation,#P35G-1.5-14-C) to 75% confluence in phenol-red free DMEM (Gibco, #21063029) supplemented with 4.5 g/L glucose and 10% (vol/vol) FBS (FBS; Gibco, #16140071) and transfected with 0.25 g HaloTag-FGFR1c plasmid the next day using Lipofectamine 3000 reagent (Invitrogen, #L3000001), according to the manufacturer's instructions. The following day, cells were starved for 2-3 hours in serum-free media, labeled with 0.25 M cell-impermeant Alexa488 HaloTag ligand (Promega, #G1001) for 15 min at 37°C and 5% CO2, and then washed 3x with phenol-red free media. After labeling, cells were immediately imaged at 37°C and 5% CO2 in a cage incubator (OkoLab) housing a Nikon Eclipse Ti2 microscope (Nikon) equipped with a motorized Ti-LA-HTIRF module with a 15-mW LU-N4 488 laser, using a CFI Plan Apochromat Lambda 100x/1.45 Oil TIRF objective and a Prime95B cMOS camera (110-nm pixel size; Teledyne Photometrics). Images were acquired using a 100-ms exposure time at 10 Hz with the laser power set at 100%. The penetration depth of the evanescent field was ~118 nm.

Single-particle tracking

Particles were localized and tracked using the MATLAB software GaussStorm.[82,96] Briefly, particles were automatically detected by application of a bandpass filter to remove noise, followed by convolution with a Gaussian kernel, and then the selection of above-threshold pixels. Particles were then fitted with elliptical two-dimensional Gaussian functions, which yielded their intensities expressed as the volume under the curve, as well as their positions with subpixel accuracy. Particles were tracked frame to frame using

a tracking algorithm with a tracking window of 7 pixels between consecutive frames. The distribution of the displacements of single particles was used to calculate mean diffusion coefficient in a field of view encompassing an entire cell.

Transcriptomics on HUVEC endothelial cells

HUVEC endothelial cells were seeded at a density of 80,000 cells/well in a 0.1% gelatin-coated 12-well tissue culture dish, and allowed to grow to 80% confluence. Cells were washed 3X with 1X PBS and serum-starved overnight in DMEM low glucose (1 g/L). Following starvation, cells were treated with either recombinant FGF2 or C6-79C_mb7 at 10 nM or 100 nM in serum-free media for 6 hours. Concentration is reported as the concentration of the oligomeric particle, not the mb7 domain. After treatment, cells were enzymatically detached using Tryp-LE [Thermo-Fisher Scientific, #12563011] and washed once with cold 1X PBS. Cells from each treatment were then counted and loaded at a concentration of 10,000 cells/lane on the 10x 3' gene expression platform [10X Genomics, PN-1000121]. After library preparation, libraries were sequenced on the Nextseq 550 with a 75 cycle high-output kit (Read1: 26bp, Index1:8bp, Read2:58). Processed reads were then mapped using the 10x cell-ranger pipeline and mapped to the hg38 reference genome. Transcriptomes from treated samples (recombinant FGF2 or C6-79C_mb7) were then compared to serum starved cells using the fit_models() function in the Monocle3 software suite. Cells treated with C6-79C_mb7 showed a similar transcription pattern in comparison to cells treated with FGF2 (Figure S27).[7]

Immunostaining of differentiated iPSCs

For immunofluorescence imaging of differentiated iPSCs, cells were seeded on glass coverslips coated with 0.1% gelatin on Day 5, and cultured until confluency on Day 14 following the process described below. The cells were then fixed in 4% paraformaldehyde (PFA) for 15 minutes. The fixed cells were washed three times for 5 min each in 1X PBS before blocking for 1 hr with 3% BSA and 0.1% Triton X-100 in 1X PBS while on nutation. Primary antibody incubation was carried out at a 1:100 dilution in blocking buffer overnight at 4C: CD31 (Cell Signaling, Catalog #3528), and PDGFR-B (Cell Signaling, Catalog #3169). Following overnight incubation, the cells were washed three times for 5 min each in 1X PBS while on nutation. The cells were then incubated with secondary antibodies (Invitrogen, A21050 and Invitrogen, A11008; 1:200 each) diluted in blocking buffer for 1.5 hrs at 37°C. Secondary antibodies were then removed, and cells were washed three times for 10 min each in 1X PBS on nutation. Coverslips were sealed using VECTASHIELD with DAPI [Vector laboratories, #H-2000-2] upside-down on glass slides for analysis in confocal microscopy. Images were taken on a Nikon Yokogawa W1 spinning disk confocal microscope using a 20X objective.

In vitro differentiation of endothelial cells

Briefly, hiPSCs (WTC-11 human induced pluripotent stem cells) [Coriell, #GM25256] were seeded on 24-well plates coated with growth factor-reduced Matrigel [Corning, #356231] and cultured in mTeSR1 stem cell medium [StemCell Technologies, #85850] until cells reach confluence with media changes daily. One day before differentiation (deemed Day (-1)), cells were pre-treated with mTeSR1 supplemented with 1μM of GSK3-Inhibitor (CHIR99021) [Cayman Chemicals, #13122]. On the first day of differentiation (D0), stem cell media was replaced with cardiogenic mesoderm media consisting of RPMI 1640 Medium [Thermo, #11875093] supplemented with 1X B27(-) [Fisher Scientific, #A1895601], 100 ng/mL Activin A [PeproTech, #120-14P] and 1X Matrigel for 17 hrs. The next day, media was replaced with RPMI supplemented with 1μM of GSK3-Inhibitor (CHIR99021), B27 (-), and 5 ng/mL bone morphogenetic protein-4 (BMP-4) [R&D systems, #314-BP-010] for 24 hours. On Day 2 of differentiation, cells were washed with 1X PBS and media was replaced with vascular differentiation media consisting of StemPro [Thermo Fisher, #10639011] supplemented with 1X Glutamax, 1X Penicillin-Streptomycin, 300 ng/mL vascular endothelial growth factor (VEGF) [R&D systems, #293-VE-050], 10 ng/mL BMP-4, 5 ng/mL FGF2, 50 ug/mL Ascorbic Acid [Sigma-Aldrich, #A8960], and 40 μM monothioglycerol (MTG) [Sigma-Aldrich, #M6145]. On Day 5, cells were dissociated with Accutase [Thermo, #A1110501] and replated on 12-well 0.1% gelatin-coated tissue culture dishes in endothelial growth media (EGM) consisting of EGM basal media [Lonza, #CC-3121] supplemented with 20 ng/mL VEGF, 20 ng/mL FGF2 and 1μM GSK3-Inhibitor (CHIR99021). EGM media was replaced every 48 hours until the final harvest at Day 28.

After harvest, samples from each day were exposed to an hypotonic lysis buffer (10mM Tris-HCl Ph7.4, 10 mM NaCl, 3 mM MgCl2, 0.05% IGEPAL), labeled with hash oligos (Table S9), chemically fixed, and then stored at -80°C until cells from all experimental timepoints had been collected. Following collection, cells were processed using the sci-RNA-seq as described previously.[97] Following library preparation, libraries were sequenced on 2 Nextseq2000 100 cycle kit with standard sequencing chemistry: Read1: 34bp, Index1: 10bp, and Read2: 66bp. Reads were then demultiplexed, assigned to cells and mapped to the hg38 reference genome. Sample barcodes were matched to a corresponding experimental condition only if a sample barcode was significantly enriched (Chi-squared test; q-value < 0.05) and displayed a 4 fold enrichment ratio in that cell.[97]

All low-quality reads were removed from the data by setting UMI cutoff to greater than 100 and removing all mitochondrial reads. To eliminate effects of cell-cycle heterogeneity, we used Seurat's[98] workflow for cell-cycle scoring and regression. Following Monocle3's workflow, the data were normalized by size factor, preprocessed using PCA, embedded in 2 dimensions with UMAP, and clustered. Differential gene expression analysis was performed to identify genes that were specifically expressed in each cluster, and this information was used to annotate each cluster based on the relative expression of canonical marker genes. The two clusters obtained at Day 14 were compared across conditions to determine the relative contribution of each treatment to either the endothelial or pericyte cluster.

The differentiation and single cell sequencing experiment was repeated, collecting only cells on Day 14. After processing the data, as described above, the endothelial cell cluster was selected for further sub-clustering, and the analysis was repeated (as described above). This analysis indicated that marker genes specific to arterial and venous endothelial cells spanned the embedding. Based on marker gene expression, the cells were annotated into arterial and venous endothelial cells, and the localization of FGF2 and C6-79C_mb7 treated cells was calculated to determine the relative contribution of each treatment.

Sample preparation for proteomics analysis

Frozen protein pellets were resuspended in lysis buffer (8 M urea, 50 mM NaCl, 200 mM EPPS pH 8.5, Roche protease inhibitor tablets) and homogenized by passing through a 21-gauge syringe. Lysates were cleared by centrifugation for 30 min at 20,000 g and protein concentrations were measured using Pierce BCA assay kits. Proteins were then reduced with 5 mM dithiothreitol (DTT) for 30 min at room temperature and alkylated with 25 mM iodoacetamide for 30 min in the dark. The alkylation reaction was quenched by adding an additional aliquot of DTT. 40 μg of protein from each sample was isolated using SP3. In brief, 2 μl of each bead type was added to each sample before adding 2 volumes of ethanol and shaking for 30 min. Sample tubes were placed on a magnet rack and supernatant was aspirated. Beads were washed with 125 μl 80% ethanol three times by resuspending and vortexing. Beads were resuspended in 40 μl digestion buffer [200 mM EPPS pH 8.5, 20 ng μl^{-1} Lys]), then incubated overnight at 37 °C with constant agitation, before adding trypsin (400 ng) for an additional 6 hr at 37 °C. The final concentration of peptide was about 1 μg/μl. HUVEC and CHO samples were labeled with TMTpro 18-plex reagents [Thermo, #A52045] separately, and the mixture was incubated at room temperature for 1 h. The reaction was quenched with 0.5% hydroxylamine, before pooling beads and eluates into a single 2 ml tube and placing it on a magnetic rack. Supernatant was collected. After labeling and mixing, peptide mixtures were desalted using C18 sep-pak cartridges [50 mg, Waters].

For phosphopeptide enrichment, PureCube magnetic beads were used with a modified protocol.[99] In brief, peptides were dissolved in 80% ACN [VMR, #BDH83639.400], 0.1% TFA [Fisher Scientific, #A117-50] and mixed with beads, shaking for 30 min. phosphorylated peptides were eluted with 50% ACN, 2.5% NH_4OH and then neutralized with 75% ACN, 10% formic acid. Eluates were desalted via Stage-tips prior to mass spectrometry analysis. Flow-throughs were then fractionated using basic-pH reverse phase chromatography.[100] Briefly, peptides were resuspended in Buffer A (10mM ammonium bicarbonate, 5% acetonitrile, pH 8) and separated on a linear gradient from 13% to 42% Buffer B (10mM ammonium bicarbonate, 90% acetonitrile, pH 8) over an Agilent 300Extend C18 column using an Agilent 1260 HPLC equipped with wavelength detection at 214 nm and 254 nm). Fractionated peptides were desalted using Stage-tips prior to mass spectrometry analysis.

Mass spectra data analysis

Peptides were separated prior to MS/MS analysis using an Easy-nLC [Thermo, #LC140] equipped with an in-house pulled fused silica capillary column with integrated emitter packed with Accucore C18 media [Thermo, #17126-032130]. Mass spectrometric analysis was carried out on an Orbitrap Eclipse [Thermo, #FSN04-10000]. For whole proteome profiling, separation was carried out with 90-minute gradients from 98% Buffer A [5% ACN, 0.125% formic acid] to 28% Buffer B [90% ACN, 0.125% formic acid]. Multiplexed analysis of samples was done using real-time search data acquisition,[101] based on canonical SPS-MS3 acquisition. Briefly, a survey MS1 scan was used to identify potential peptide precursors (R = 120000, Mass range: 400-2000 m/z, max Inject time: 50ms, AGC: 200%, RF lens: 30%). The top 10 precursors were selected for fragmentation and analysis in the ion trap (Dynamic exclusion: 90s at 10ppm, CID collision energy: 35%, max inject time: 50 ms, AGC: 200%, scan rate: rapid, isolation width: 0.5 m/z). Real-time spectral matching was carried out using the Comet search algorithm.[102] If, and only if, a peptide was matched with high confidence, the instrument would then acquire an additional SPS-MS3 scan for quantification of relative abundances (R = 50000, HCD NCE: 45, max injection time: 150 ms).

For phosphopeptide profiling, separation was carried out with 90-minute gradients from 98% Buffer A (5% ACN, 0.125% formic acid) to 26% Buffer B (90% ACN, 0.125% formic acid). Multiplexed analysis of samples was done using canonical SPS-MS3 acquisition. Briefly, a survey MS1 scan was used to identify potential peptide precursors (R = 120000, Mass range: 300-2000 m/z, max Inject time: 50ms, AGC: 200%, RF lens: 30%). The top 10 precursors were selected for fragmentation and analysis in the ion trap (Dynamic exclusion: 90s at 10ppm, HCD NCE: 30, max inject time: 35 ms, AGC: 250%, scan rate: rapid, isolation width: 0.5 m/z). SPS-MS3 was carried out in the Orbitrap (R = 50000, AGC: 250%, HCD NCE: 45, max inject time: 86 ms).

Raw spectral information was converted to mzXML format using Monocle,[103] and spectra were matched using the Comet search algorithm comparing against the Uniprot human and hamster database. TMTpro is a static modification at the N-terminus of peptides. The maximum missed cleavage was set as 2. Peptides and proteins were filtered to a 1% using rules of protein parsimony.

The protein and phosphosite abundances for each treatment condition were then compared to the average of the vehicle control treatment condition and subjected to a logarithmic transformation with a base of 2 (log_2) of the resulting ratios. Correlation was plotted for the normalized (phospho-)protein log_2 ratios for C6-79C_mb7 and FGF2 treated (100 nM) cells in FGFR1c-expressing CHO and HUVEC cells.

Flow cytometry

Cells derived using FGF2, C6-79C_mb7, and mb7 in combination with FGF2 (at Day 14 of differentiation) were harvested as a single cell suspension, adjusted to a concentration of 0.5 x 10^6 cells/mL in ice-cold FACS Buffer (1X PBS, 1% BSA, 0.1% NaN3 sodium

azide [Millipore-Sigma, #26628-22-8], and blocked for 30 minutes on ice. Primary (unlabeled) antibodies were added at a dilution of 1:100 in FACS buffer for 30 min at 4C: CD31, CLDN5 [Abcam, #15106]. Cells were washed 3 times in 1X PBS by centrifugation at 1500 rpm for 5 minutes each, following which primary (labeled) or secondary antibodies were added at a dilution of 1:100 in FACS buffer for 1 hr at 4C in the dark: VE-Cadherin-APC [eBioscience, #17-1449-42], PDGFR-B-APC [BioLegend, #323608], NG2-FITC [EMD Millipore, #AB5320A4] and ACTA2-PE [Abcam, #208844]. Cells were washed 3 times in 1X PBS by centrifugation at 1500 rpm for 5 minutes each and resuspended in 100uL of ice-cold FACS Buffer for subsequent analysis. Unstained controls were included. Samples were run on a FACSCanto II flow cytometer (BD Biosciences) and recorded events were analyzed using the flowCore package for R. FSC and SSC (Unstained control) were used for size gating. Events were analyzed as percentage of cells positive for the given panel of markers, and values are reported as mean ± SEM from 3 independent biological replicates.

Cell migration assay

Cells derived using no FGF, FGF2, C6-79C_mb7, and mb7 in combination with FGF2 (until Day 14 of differentiation) were grown on 12-well plates coated with 0.1% gelatin. Following the formation of a cell monolayer, with the tip of a 200-uL pipette, a scratch was made to remove cells from the top to bottom of each well. Cells were allowed to grow for 24 hours, and images were captured at the 0-, 6- and 24-hour time points using a Nikon Yokogawa W1 spinning disk confocal microscope at a 20X objective. Images were taken from 3 arbitrarily chosen fields from a total of 3 biological replicates per treatment. The size of the scratch area was quantified using the Wound Healing Size Tool for ImageJ,[87] and values are reported as a percentage reduction in wound area from the 0-hour time point.

Tube formation assay

Cells derived using FGF2, C6-79C_mb7, and mb7 in combination with FGF2 (at Day 14 of differentiation) were seeded on 24-well plates pre-coated (30 minutes before seeding) with ice-cold growth-factor reduced 100% Matrigel. Cells were seeded at a density of 1.5 x 10^5 cells/well, and were incubated at 37°C for 24 hours in serum-free media (DMEM low glucose (1 g/L). Tubular structures were observed after 24 hours, and images were taken from 5 arbitrarily chosen fields from a total of 3 biological replicates per treatment using a Nikon Yokogawa W1 spinning disk confocal microscope at a 20X objective. To quantify their 2D network forming ability, the number of nodes, segments and meshes in each field were quantified using the Angiogenesis Analyzer macro tool[86] for ImageJ. All data were normalized to the FGF2 treatment.

LDL uptake assay

LDL uptake was assessed with the LDL Uptake Assay Kit Cell-Based [Abcam, #287862], using an adapted protocol. Briefly, cells derived using FGF2 and C6-79C_mb7 (at Day 14 of differentiation) were seeded at a density of 3 x 10^5 cells/well in 96-well plates coated with 0.1% gelatin and allowed to starve overnight in DMEM low glucose (1 g/L). Post-starvation, cells were washed with Uptake Assay Buffer (pre-heated to 37°C) and replaced with a 0.1 mg/mL working solution of Fluorophore-Labeled LDL (diluted in pre-heated Uptake Assay Buffer). Cells were incubated at 37°C for 4 hours, following which the cells were washed with Uptake Assay Buffer and harvested for analysis. Samples were run on a FACSCanto II flow cytometer (BD Biosciences) and recorded events were analyzed using the flowCore package for R using a similar process to the one described previously.

Cytokine challenge assay

Cells derived using FGF2 and C6-79C_mb7 (until Day 14 of differentiation) were grown on glass coverslips coated with 0.1% gelatin, following which they were treated with 10 ng/mL TNF-a [Gibco, #PHC3011] in DMEM low glucose (1 g/L) for 24 hours. After 24 hours, the cells were fixed with 4% paraformaldehyde (PFA) for analysis. The fixed cells were washed 3 times for 5 min each in 1X PBS before blocking for 1 hour with 3% BSA and 0.1% Triton X-100 in 1X PBS while on nutation. Primary antibody incubation was carried out at a 1:100 dilution in blocking buffer overnight: VCAM1 [Abcam, #134047]. Following overnight incubation, the cells were washed three times for 5 min each in 1X PBS while on nutation. The cells were then incubated with secondary antibody [Invitrogen, #A11008; 1:200] diluted in blocking buffer for 1.5 hours at 37°C. Secondary antibodies were then removed, and cells were washed three times for 10 min each in 1X PBS on nutation. Coverslips were sealed using VECTASHIELD including DAPI upside-down on glass slides for analysis in confocal microscopy. Images were taken from 5 arbitrarily chosen fields from a total of 3 biological replicates per treatment, using a Nikon Yokogawa W1 spinning disk confocal microscope at a 40X objective.

F-actin assembly

Contractile potential was assessed by quantifying the assembly of F-actin fibers in the cytoplasm. Cells derived using FGF2, C6-79C_mb7, and mb7 in combination with FGF2 (until Day 14 of differentiation) were grown on glass coverslips coated with 0.1% gelatin until they reached ~80% confluence. The cells were then fixed with 4% paraformaldehyde (PFA) for analysis. The fixed cells were washed three times for 5 min each in 1X PBS before blocking for 1 hr with 3% BSA and 0.1% Triton X-100 in 1X PBS while on nutation. Primary antibody incubation was carried out at a 1:100 dilution in blocking buffer overnight: PDGFR-B. Following overnight incubation, the cells were washed three times for 5 min each in 1X PBS while on nutation. The cells were then incubated with secondary antibody (Invitrogen, #A11008; 1:200) and Phalloidin (1:100, Invitrogen, #A12380) diluted in blocking buffer for 1.5 hrs at 37°C. Secondary antibodies were then removed, and cells were washed three times for 10 min each in 1X PBS on nutation. Coverslips were

sealed using VECTASHIELD including DAPI upside-down on glass slides for analysis in confocal microscopy using a Nikon Yokogawa W1 spinning disk confocal microscope with a 20X objective. Images were captured from 7 randomly chosen fields from a total of 3 biological replicates per treatment. Cells in each field were segmented using Cellprofiler,[94,95] and the mean intensity of Phalloidin was quantified per cell. All summarized results are normalized to the FGF2 treatment.

Blood vessel organoids

To create iPSC-derived vascular organoids, WTC-11 hiPSCs were passaged, counted, and resuspended in differentiation media (DMEM/F12, 20% KOSR [Gibco, #10828028], 1X Glutamax, 1X NEAA [Gibco, #11140050]) supplemented with 50μM Y-27632 [Tocris Bioscience, #1254] and distributed into Ultra Low Attachment 6-well culture plates [Corning, #07-200-601] at a density of 3 x 10^5 cells/well to allow spheroid formation. At Day 3, cells were fed with fresh differentiation media supplemented with 12μM CHIR99021. At Days 5, 7, 9, cells were fed with fresh differentiation media supplemented with 30ng/ml recombinant BMP-4, 30ng/ml recombinant $VEGFA_{165}$, and 30ng/ml recombinant FGF2. For Days 11-15, the glucose in the differentiation media was reduced to 2 g/L glucose from 3.15 g/L by using SILAC Advanced DMEM/F12 [Gibco, #A2494301] supplemented with 147.5 mg/mL L-Arginine, 91.25 mg/mL L-Lysine, 2 g/L D-Glucose, 20% KOSR, 1X Glutamax and 1X NEAA. On Day 11, cells were given fresh differentiation media supplemented with 30ng/ml $VEGFA_{165}$, 30ng/mL FGF2, and 10 μM SB431542 [Miltenyi, #130-106-275]. On Day 13, cells were transferred to Ultra Low Attachment U-Bottom 96 well plates [Corning #CLS3474-24EA] at 1 organoid per well, embedded in 1:1 Matrigel:Collagen I matrix, and overlaid with differentiation media supplemented with 100 ng/mL $VEGFA_{165}$ and 100 ng/mL FGF2. From Days 15 to 23, the glucose in the differentiation media was reduced to 1g/L glucose (physiological glucose) by making it as described for Days 11-15, but supplemented with 1 g/L glucose. Cells were fed on Day 15 and every 3 days thereafter until Day 37. To test the ability of C6-79C_mb7 to yield arterial vascular organoids, the FGF2 in the media between days 5 and 13 was replaced with an equivalent concentration of C6-79C_mb7. At time of harvest, organoids were fixed in 8% PFA diluted 1:1 in differentiation media (4% final concentration) for 15 minutes and washed 3 times for 5 minutes each in 1X PBS. Prior to immunostaining, cells were stored in 1X PBS at 4°C.

Immunostaining of blood vessel organoids

For immunostaining, all processes were done with organoids in suspension and all incubations were done in tubes on a nutator. Organoids were blocked in solution (1X PBS containing 5% normal goat serum and 0.3% Triton-X) overnight at 4°C. They were then suspended in antibody dilution buffer (1X PBS containing 1% BSA and 0.3% Triton-X) and primary antibodies diluted at concentrations recommended by the manufacturer and incubated overnight at 4°C. On the third day, cells were washed 3 times for 5 minutes with 1X PBS, then resuspended in antibody dilution buffer containing secondary antibodies at 1:200 and DAPI (1:50), and then incubated overnight at 4°C. On the fourth day, organoids were washed 3 times for 5 minutes in 1x PBS and mounted in Vectashield Antifade Mounting Media on a glass microscope slide equipped with a press-to-seal silicone isolator [Electron Microscopy Sciences], 1 organoid per well. Organoids were imaged on a Leica DMi8 confocal microscope equipped with HyD and PMT spectral detectors and LASX acquisition software [version 3.5.5IR]. Images were processed using Lightning Deconvolution. Images were captured with 10X (NA 0.4 PlanApo) and 20X (NA 0.75 PlanApo) air lenses or a 40X (NA 1.1 PlanApo) water immersion lens. Resulting confocal images were processed with Imaris Microscopy Image Analysis Software (Version 9.9) and FIJI ImageJ Analysis software (Version 2.14.0).

In vivo injections of blood vessel organoids

Mouse kidney capsule implantation

Blood vessel organoids were differentiated using the protocol above with either FGF2 or C6-79C_mb7 for 21 days. On the day of transplantation, organoids in suspension were broken down into single organoids and transferred to a beveled, kinked PE50 tubing [BD Intramedic, #427517]. Two experimental groups were created corresponding to two treatment conditions (FGF2 or C6-79C_mb7, n = 3 mice per group). Adult NOD-SCID mice (8-10 weeks old) were anesthetized using isoflurane supplemented with oxygen within an anesthesia chamber. Animals were then transferred to a nose cone and maintained on 2% isoflurane. To maintain a body temperature of 37C, mice were placed on a heating pad throughout the transplantation. Mice were shaved and the site was sterilized with betadine and alcohol wipes prior to making a 1-2 cm dorsal flank incision. Kidneys were externalized using a cotton swab and the capsule was nicked near the caudal end using a needle tip (22 gauge). The beveled PE50 tubing was inserted beneath the capsule and cellular material was implanted under the control of a Hamilton syringe. A cotton swab was used to clot and seal the opening in the capsule to hold the implant in place. Next, the kidney was returned to the abdominal cavity, the peritoneum was sutured shut with absorbable sutures, and the skin was closed with surgical staples. Experiment was performed in compliance with ethical regulations, IACUC protocol #4375-01. Mice were placed into a heated recovery cage until they regained consciousness, and then moved back to their home cage and transported back to the vivarium. 20 days after injection, mice were euthanized, kidneys were excised with graft intact and fixed in 4% paraformaldehyde at 4°C for 1.25 hours and transferred to 30% sucrose solution at 4°C overnight. Kidneys were then bisected and embedded in embedding cryo-molds [Sakura, #25608-916] with Tissue-Tek O.C.T. compound [Sakura, #4583]. The embedded tissue was then frozen by placing a cold-resistant beaker of 2-methylbutane solution [EMD, #MX0760-1] into liquid nitrogen, which causes fast cooling to -80 °C. Samples were then placed in a -80 °C freezer for storage until cryo-sectioning. 10-20 μm-thick sections were made on pre-chilled Superfrost Plus microscope slides [Fisherbrand, #12-550-15] and then stored at -80 °C until used for immunofluorescence analysis.

Immunofluorescence staining

Frozen slides were blocked in blocking buffer (5% Normal Goat Serum, 0.3% Triton X-100 in 1X PBS) for 90 minutes at RT. Primary antibody incubation was carried out in antibody buffer (1% BSA, 0.3% Triton X-100 in 1X PBS) overnight at 4C: anti-hVE-Cadherin (1:100, [Cell Signaling, Catalog #2500]), anti-hCD31, and anti-mCD31 (1:100, [BD Biosciences, #557355]). Following overnight incubation, the cells were washed three times for 5 min each in 1X PBS, followed by incubation with secondary antibodies (1:200 each) diluted in antibody buffer overnight at 4C. Secondary antibodies were then removed, and cells were washed three times for 5 min each in 1X PBS on nutation. Coverslips were sealed using VECTASHIELD including DAPI upside-down on glass slides for analysis in confocal microscopy.

QUANTIFICATION AND STATISTICAL ANALYSIS

Details of the quantification and statistical analysis can be found in the Figure legends and method details section. Data analysis for SAXS experiments was performed with FrameSlice[32] and ScÅtter[32] software packages and compared to model predictions using the FOXS server.[74] Cryo-EM model building and refinement was performed in PHENIX v.1.16[80] using iteratively phenix.real_space_refine and manual adjustments in COOT.[81] Calcium release assays were processed and analyzed with the Fiji software distribution of ImageJ v1.52i[84,93] and cellular fluorescence was quantified with CellProfiler,[94,95] which was also used for F-actin assembly measurements. Cell migration assays were analyzed with the Wound Healing Size Tool[87] for ImageJ. Tube formation assays were analyzed via the Angiogenesis Analyzer macro tool[86] for ImageJ. Flow cytometry assays were analyzed with FlowJo software or the flowCore package[83] for R and plotted with Origin Pro 9.1. Biolayer-Interferometry data was analyzed using the Octet Analysis Software (Sartorius). Single-particle tracking analysis using TIRF microscopy was done using the MATLAB software and GaussStorm.[82] Transcriptomics data was analyzed using the Monocle3[85] software suite. Immunostainings of blood vessel organoids were processed with the Imaris Microscopy Image Analysis Software (Oxford Instruments) and Fiji ImageJ Version 2.14.0.[84,93]

Supplemental figures

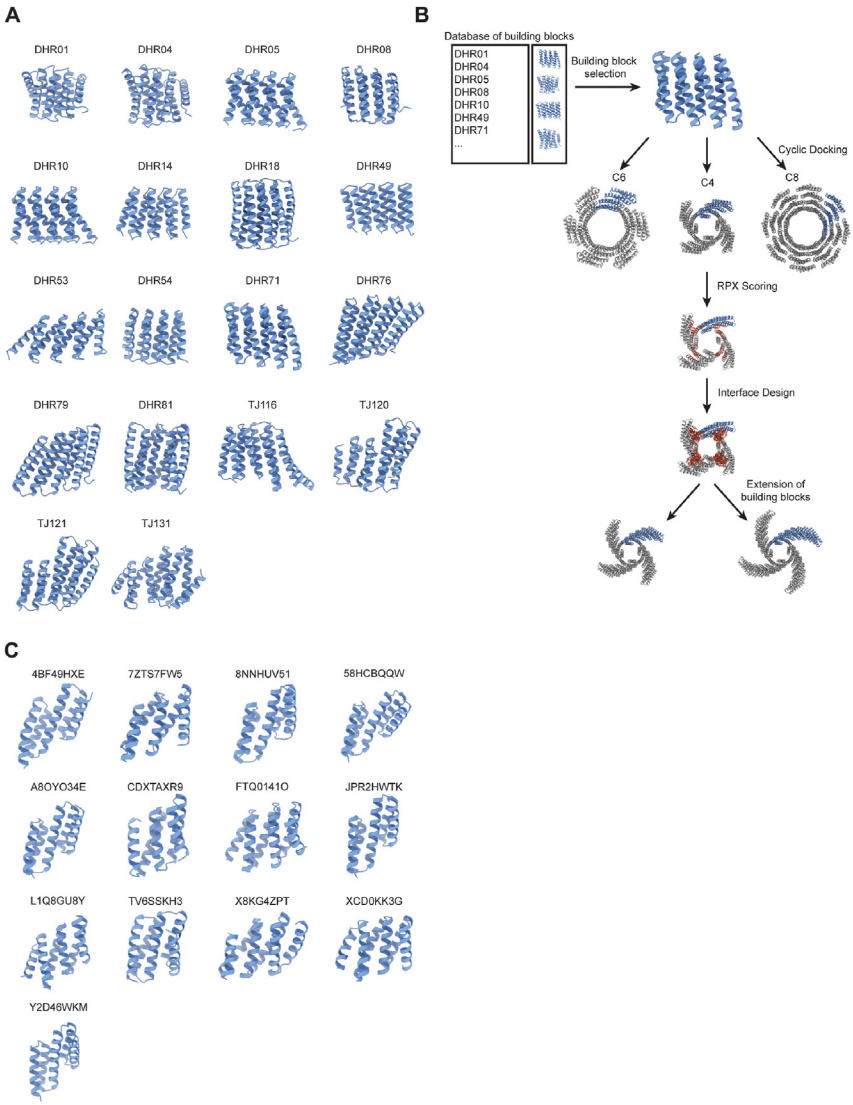

Figure S1. Library of building blocks and computational workflow for oligomeric docking, related to Figure 1

(A) Building blocks used for docking oligomers into various symmetries.

(B) Building blocks are selected from a library of previously designed DHRs. They are then docked into various cyclic symmetries and docking quality is evaluated by RPX scoring. Designs are then interface-designed and evaluated by Rosetta score metrics. Successful designs were then extended by repeat unit addition.

(C) Building blocks used for docking oligomers into C2 symmetries that advanced to experimental characterization.

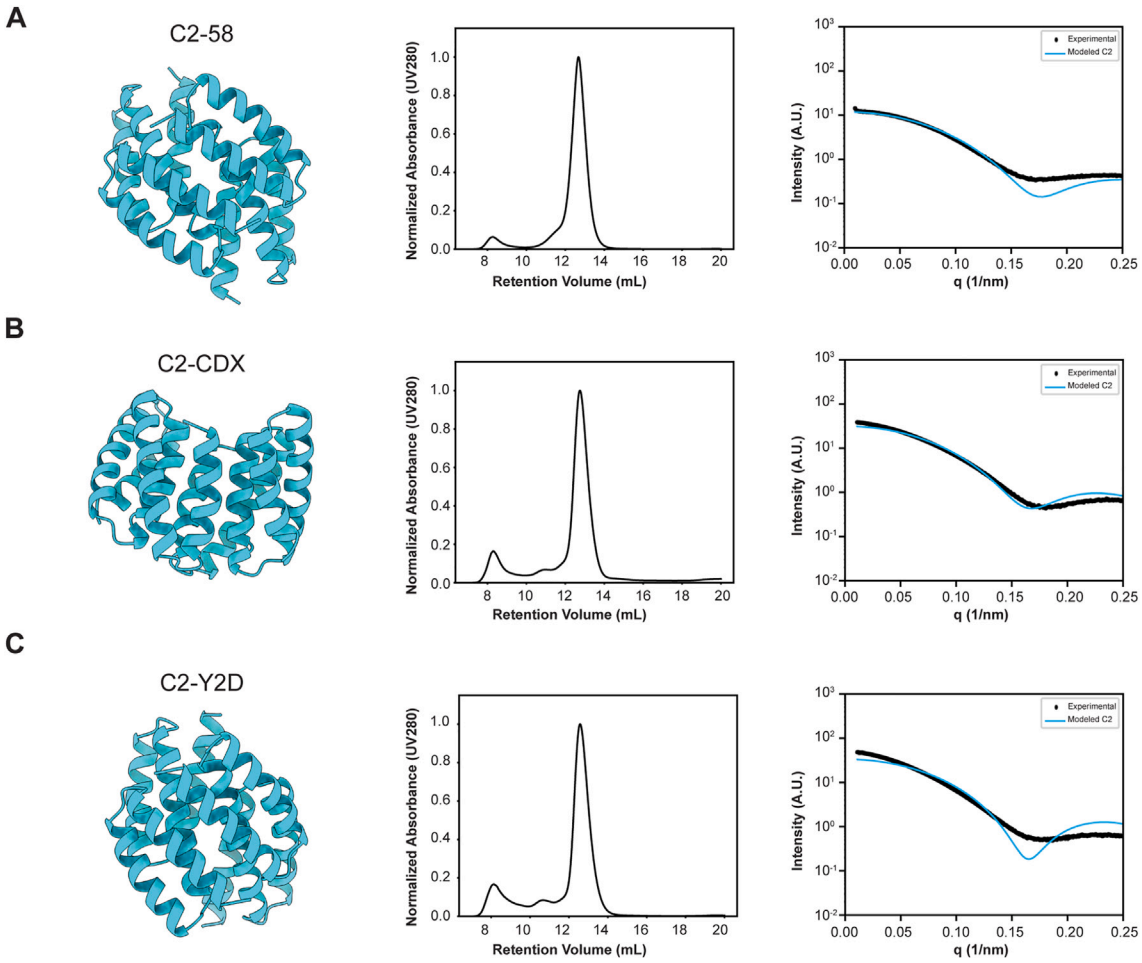

Figure S2. Biophysical characterization of C2-oligomers, related to Figure 1

Left: design model. Middle: SEC characterization. Right: SAXS trace comparison of data (black) versus design (cyan). (A) C2-58, (B) C2-CDX, (C) C2-Y2D construct.

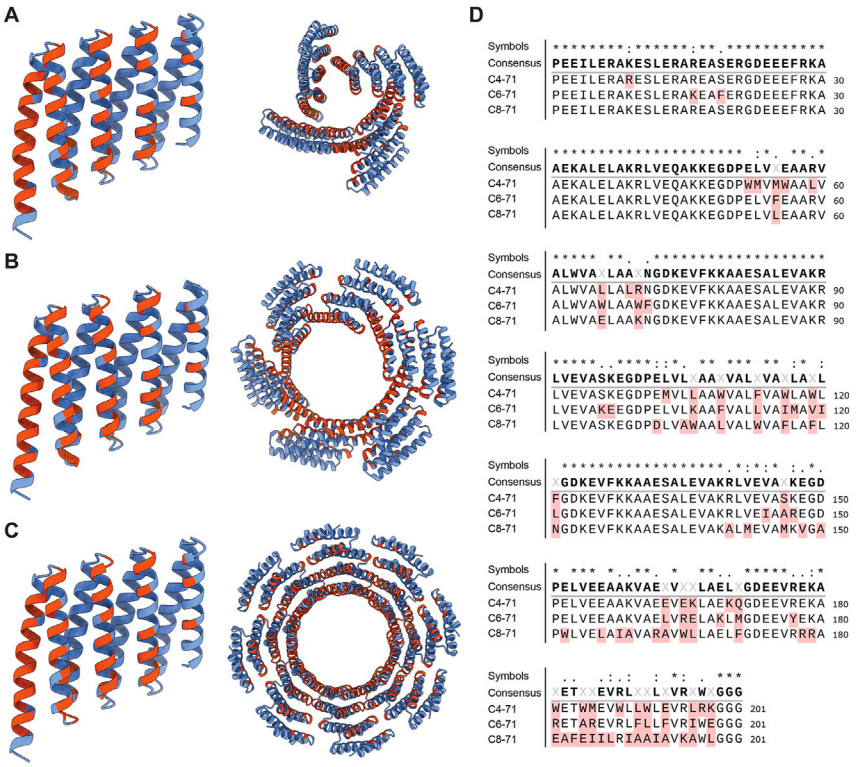

Figure S3. DHR-71 is able to form different oligomers based on the dock and interface residues, related to Figure 2

Residues that changed in comparison with the different oligomeric states are labeled in red.

(A) C4-71 asymmetric unit (left) and oligomeric structure (right).

(B) C6-71 asymmetric unit (left) and oligomeric structure (right).

(C) C8-71 asymmetric unit (left) and oligomeric structure (right).

(D) Multiple sequence alignment of DHR-71-based oligomers.

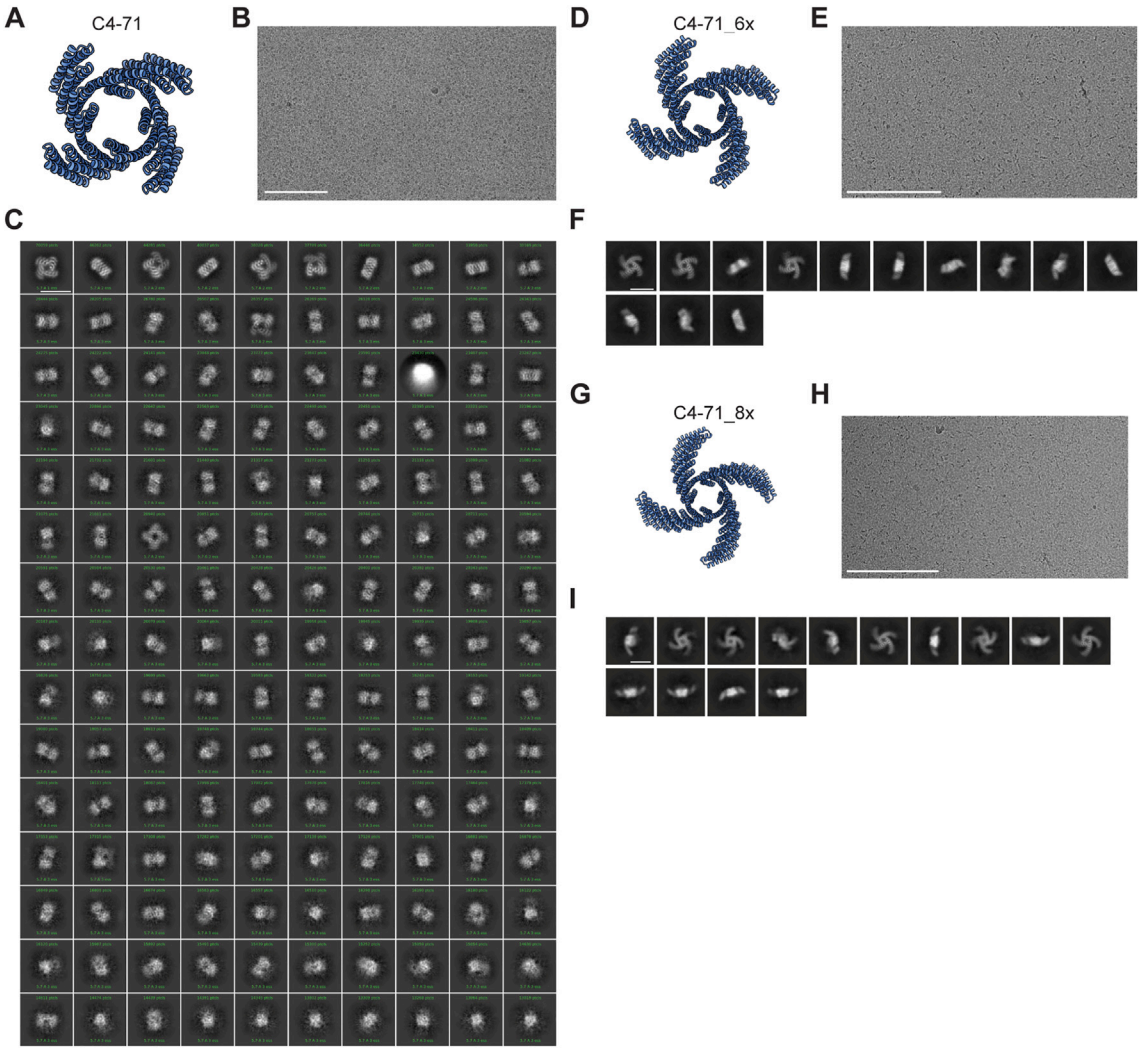

Figure S4. C4-71 extensible oligomer, related to Figure 2

(A–C) (A) C4-71 design model, (B) cryo-EM grid image, and (C) class averages.
(D–F) (D) C4-71_6x repeat extension design model, (E) cryo-EM grid image, and (F) class averages.
(G–I) (G) C4-71_8x repeat extension design model, (H) cryo-EM grid image, and (I) class averages.
Scale bars: 200 nm in (E) and (H), 100 nm in (B), and 10 nm in (C), (F), and (I).

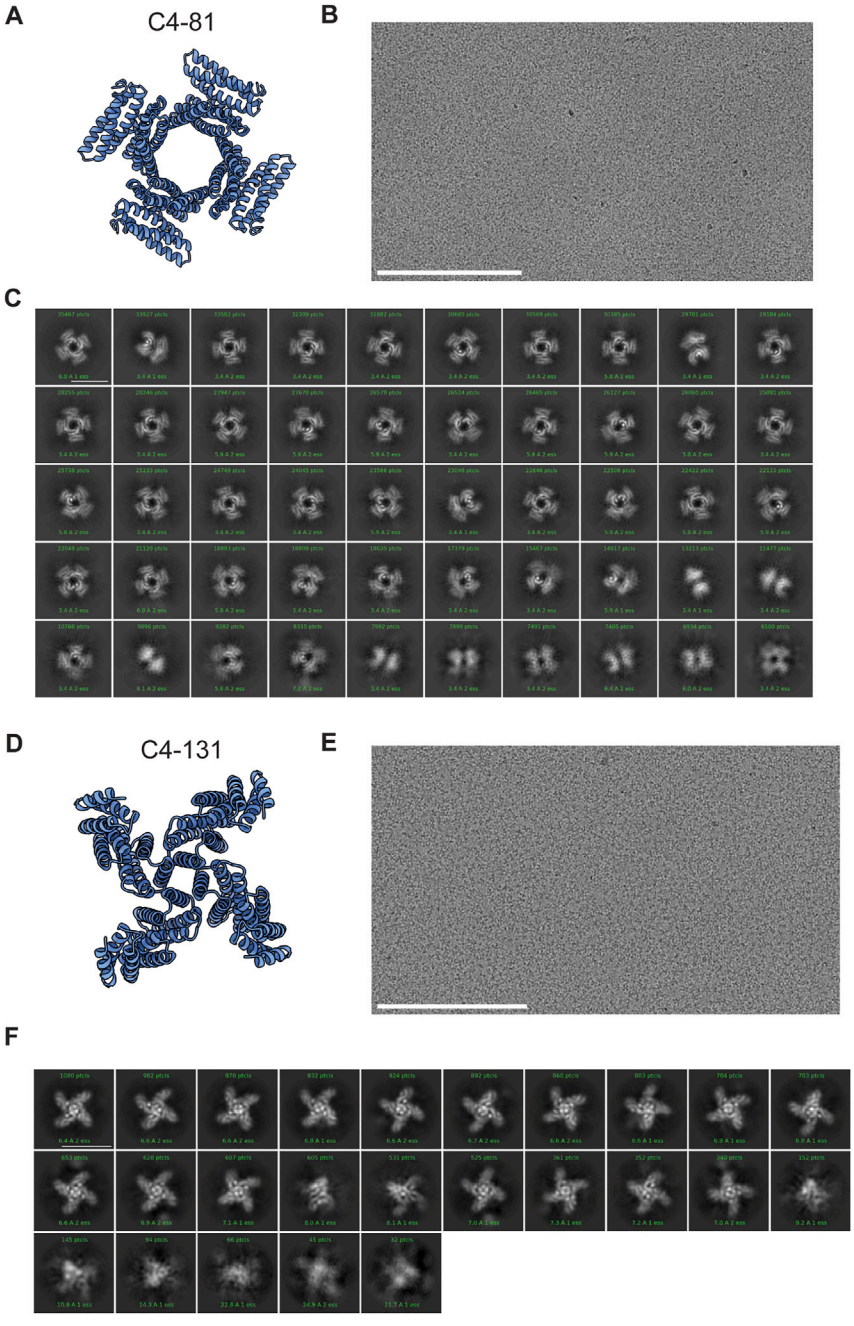

Figure S5. C4-81 and C4-131 class averages, related to Figure 1

(A–C) (A) C4-81 design model, (B) cryo-EM grid image, and (C) class averages.
(D–F) (D) C4-131 design model, (E) cryo-EM grid image, and (F) class averages.
Scale bars: 200 nm in (B) and (E) and 10 nm in (C) and (F).

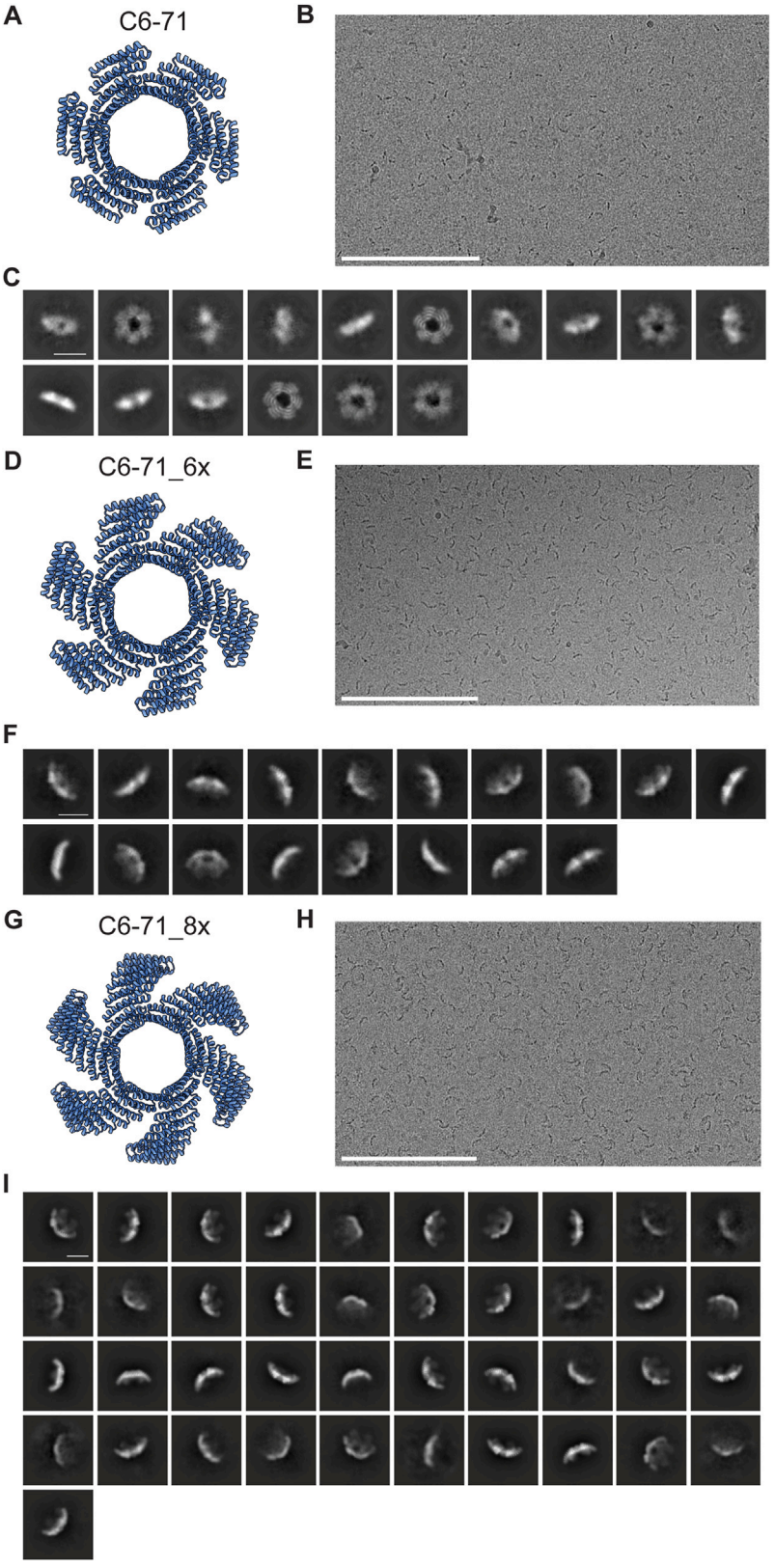

(legend on next page)

Figure S6. C6-71 extensible oligomer, related to Figure 2

(A–C) (A) C6-71 design model, (B) cryo-EM grid image, and (C) class averages.
(D–F) (D) C6-71_6x repeat extension design model, (E) cryo-EM grid image, and (F) class averages.
(G–I) (G) C6-71_8x repeat extension design model, (H) cryo-EM grid image, and (I) class averages.
Scale bars: 200 nm in (B), (E), and (H) and 10 nm in (C), (F), and (I).

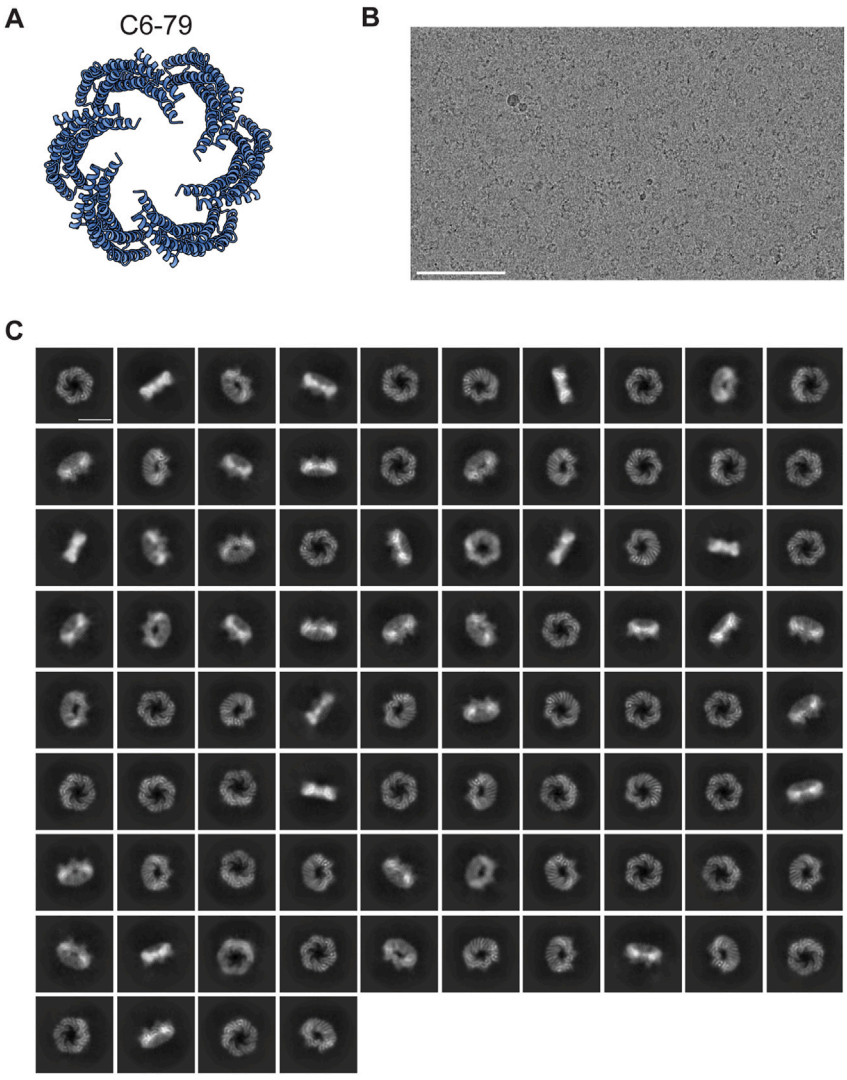

Figure S7. C6-79, related to Figure 2

(A) C6-79 design model, (B) cryo-EM grid image, and (C) class averages. Scale bars: 100 nm in (B) and 10 nm in (C).

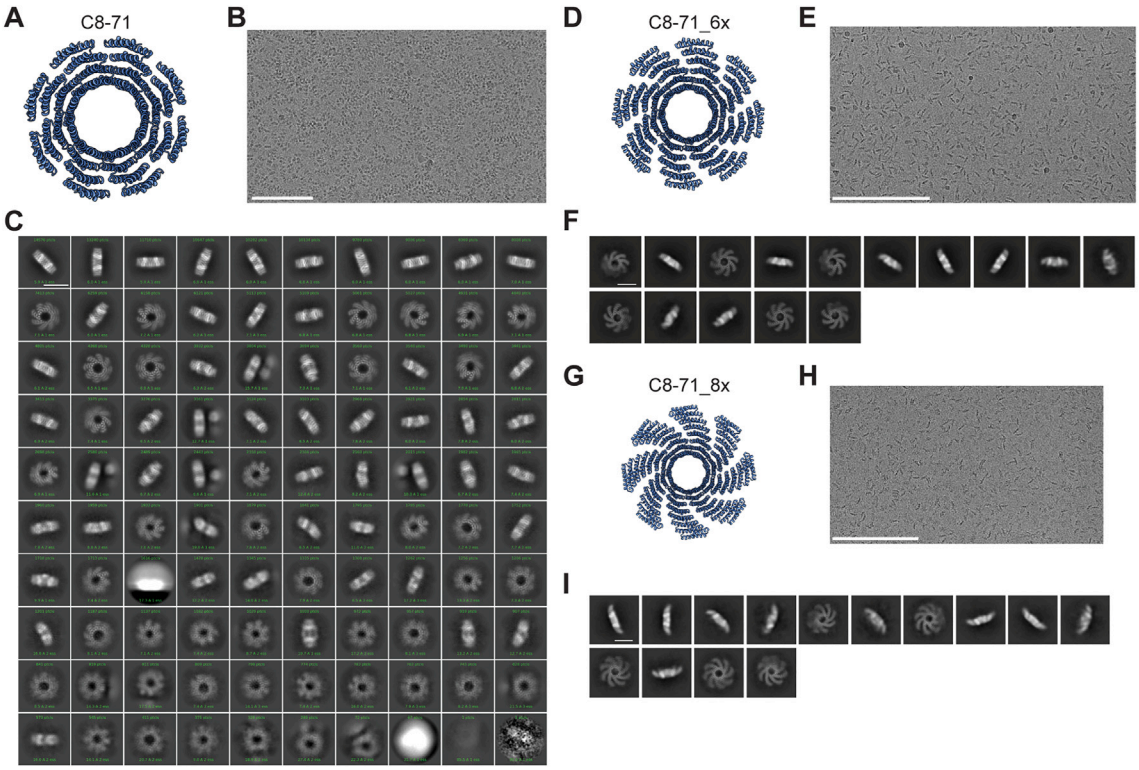

Figure S8. C8-71 extensible oligomer, related to Figure 2

(A–C) (A) C8-71 design model, (B) cryo-EM grid image, and (C) class averages.
(D–F) (D) C8-71_6 repeat extension design model, (E) cryo-EM grid image, and (F) class averages.
(G–I) (G) C8-71_8 repeat extension design model, (H) cryo-EM grid image, and (I) class averages.
Scale bars: 200 nm in (E) and (H), 100 nm in (B), and 10 nm in (C), (F), and (I).

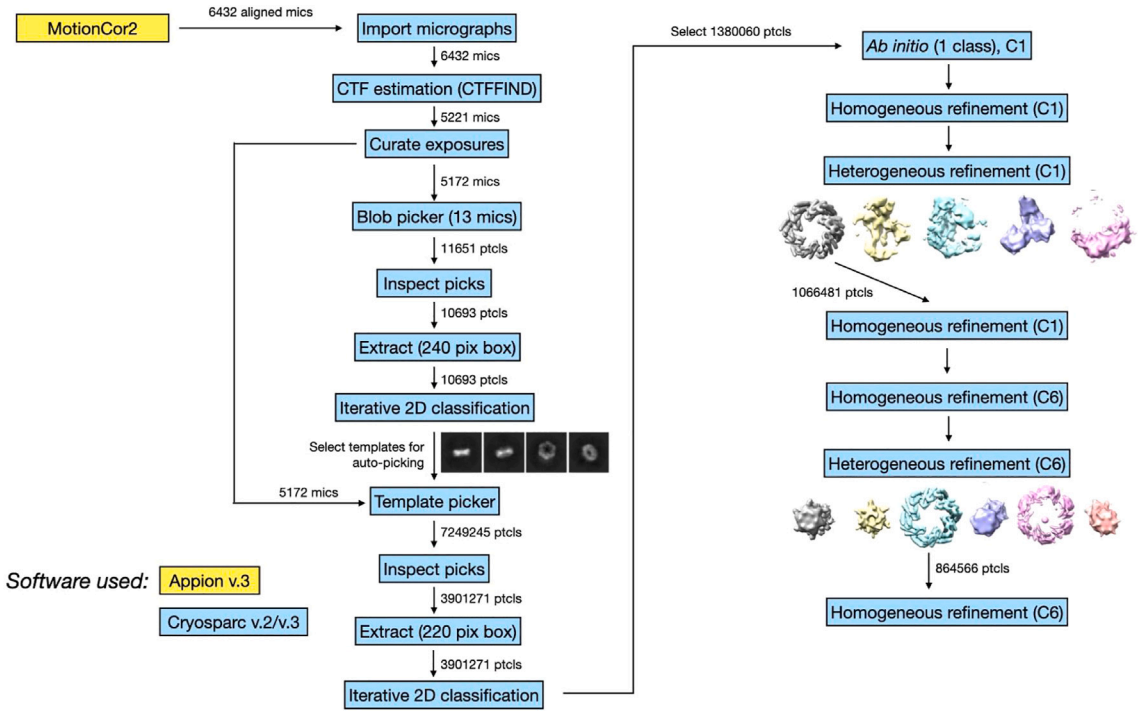

Figure S9. Cryo-EM processing workflow for C6-79, related to Figure 3

Individual steps of the cryo-EM processing workflow are depicted in the diagram to reconstruct the structure of C6-79. In total 6,432 aligned micrographs were used as input for the processing.

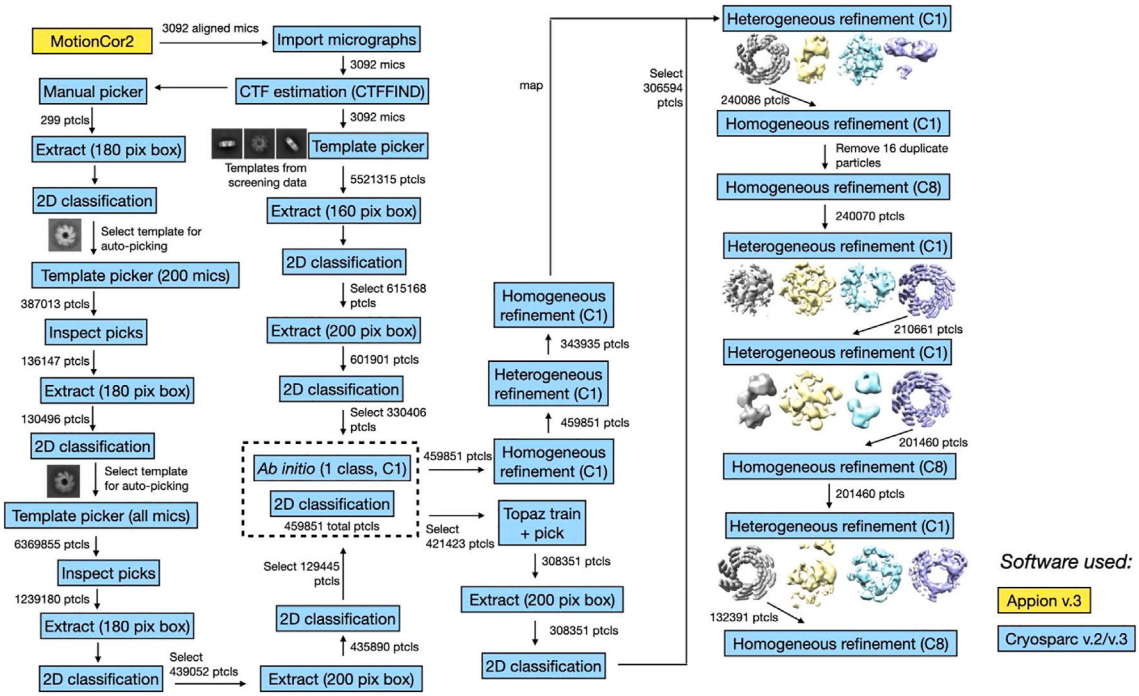

Figure S10. Cryo-EM processing workflow for C8-71, related to Figure 3

Individual steps of the cryo-EM processing workflow are depicted in the diagram to reconstruct the structure of C8-71. In total 3,092 aligned micrographs were used as input for the processing.

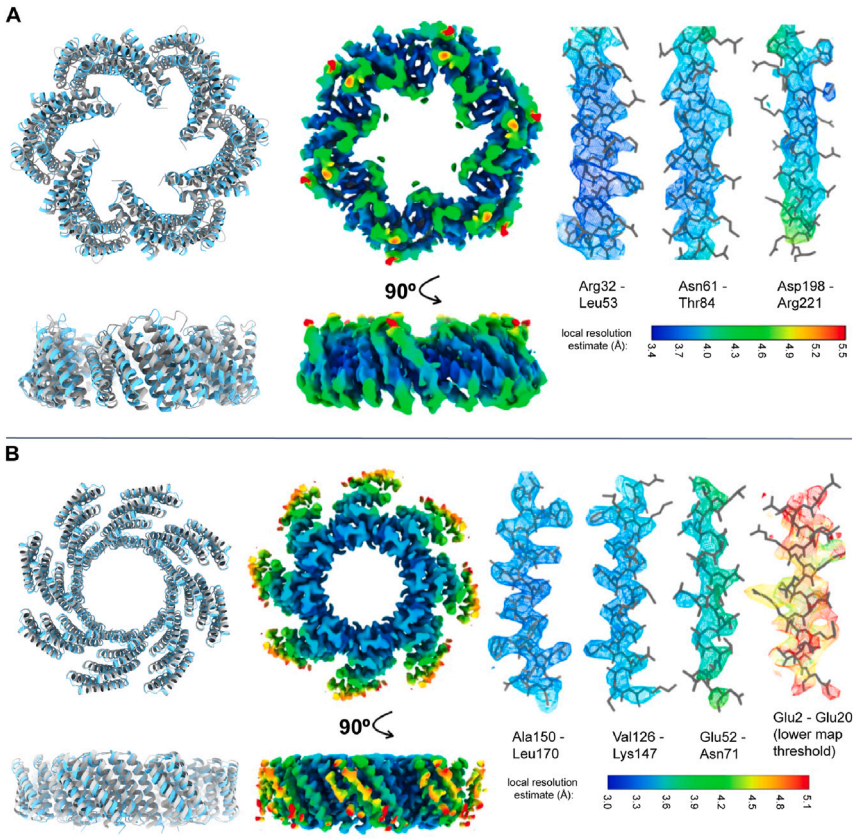

Figure S11. C6-79 and C8-71 cryo-EM models, related to Figure 3

Overview of C6-79 (A) and C8-71 (B) cryo-EM models. Left: alignment of cryo-EM structures (cyan) with design models (gray). Middle: cryo-EM maps colored by local resolution. Right: helices from the cryo-EM models shown within the corresponding map regions, representing areas of the map with different local resolution. With the exception of the Glu2-Glu20 helical region, the map segments for each design are shown at the same threshold.

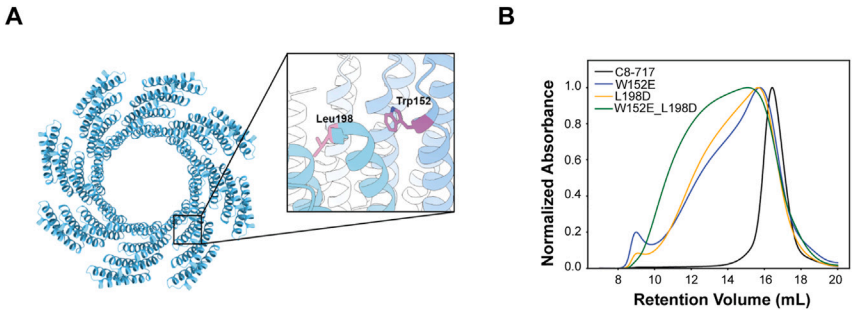

Figure S12. C8-71 mutational analysis, related to Figure 3

(A) C8-71 structure. Inset shows critical residues L198 and W152.

(B) Mutations in interface residues W152 and L198 lead to aggregation of the C8-71 structure manifested by a broadening of the SEC peaks.

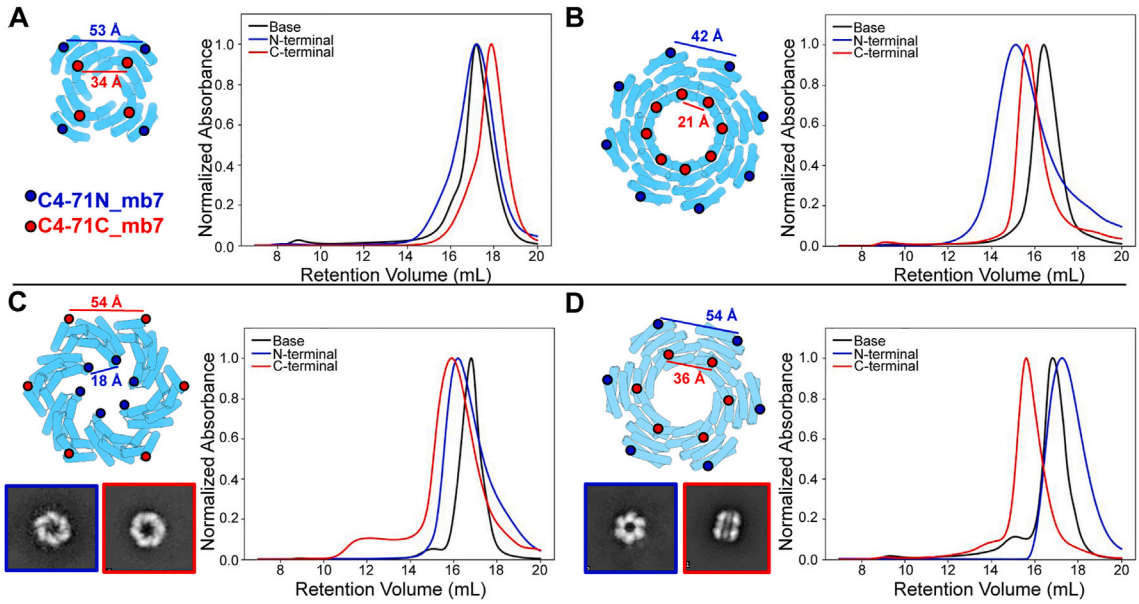

Figure S13. SEC characterization of mb7 presenting oligomers, related to Figure 4

Red and blue circles indicate the N or C termini of the oligomers at which mb7 was flexibly fused to the structure. (A) C4-71, (B) C8-71, and (C) C6-79, including top view class averages of N- (blue) and C-terminal (red) fusions. (D) C6-71, including top view classes of N- (blue) and C-terminal (red) fusions. C-terminal fusion leads to a macaron-like self-associating structure indicated in the class averages and shown by the large shift on SEC (red trace).

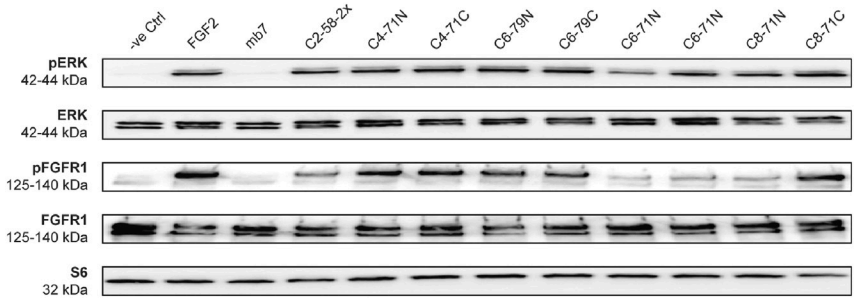

Figure S14. Western blot signaling analysis, related to Figure 4

Western blot analysis of pERK and pFGFR1 levels in CHO-R1c cells after treatment with 10 nM of agonists for 15 min and comparison with corresponding total protein levels. pERK, pFGFR1, and S6 data shown are the same as in Figure 4B and are shown here again for clarity.

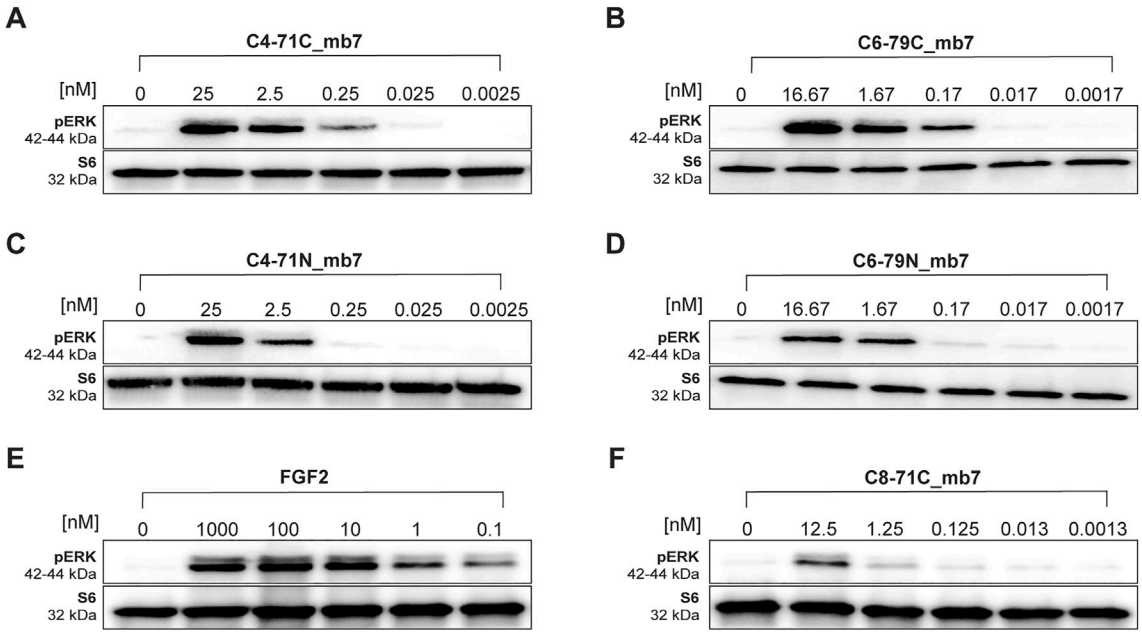

Figure S15. Western blot titration analysis for selected designs, related to Figure 4

hFGFR1c-expressing CHO cells were treated with different concentrations of FGF2 or designed scaffolds for 15 min at 37°C, followed by western blot analysis for phosphorylated ERK. (A) C4-71C_mb7, (B) C6-79C_mb7, (C) C4-71N_mb7, (D) C6-79N_mb7, (E) FGF2, and (F) C8-71C_mb7.

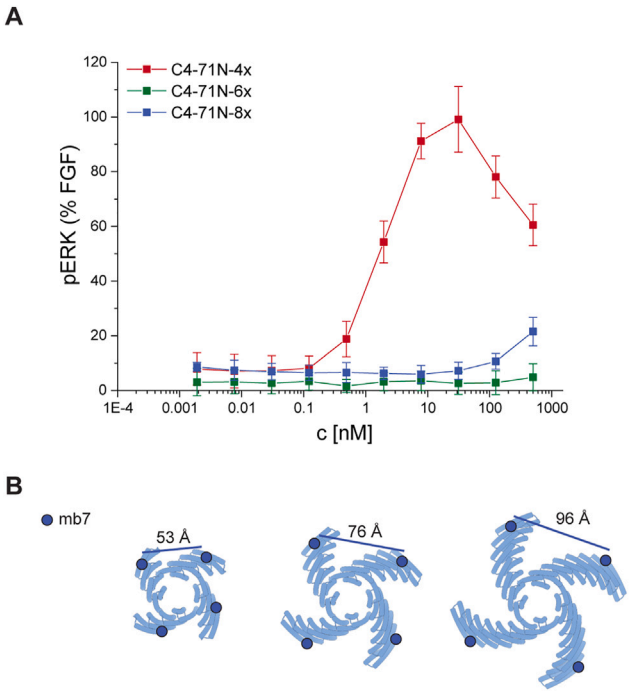

Figure S16. Signaling response of C4-71N_mb7 extension series, related to Figure 4

(A) Phosphoflow measurements of phosphorylated ERK for the C4-71N_mb7 extension series. Error bars represent SEM from three independent biological repeats.

(B) Cartoon models and distance measurements (N terminus indicated with blue circle) of mb7 attachment points for the different extended constructs (C4-71N: 4-repeat, 6-repeat, 8-repeat).

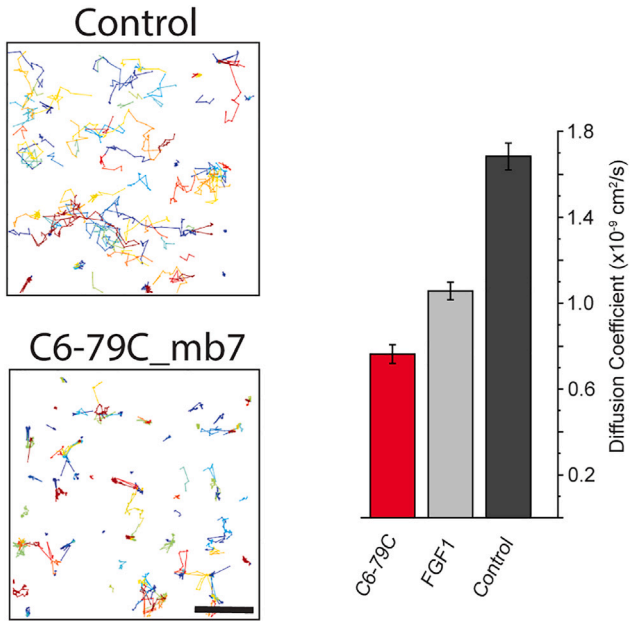

Figure S17. Direct measurement of FGFR diffusion coefficients in the cell membrane, related to Figure 4

CHO-R1c cells were treated with FGF1/heparin or C6-79C_mb7 and fluorescently tagged FGFR1c (HaloTag-R1c) revealed a strong decrease in the diffusion coefficient values in both conditions. The more pronounced effect of C6-79C_mb7 on the diffusion coefficient of FGFR1c may indicate a more robust FGFR1c clustering stimulated by the multivalent cyclic homo-oligomers. Diffusion coefficients were calculated from analyzing the labeled receptor tracks. Error bars represent SEM from three independent biological repeats. Scale bars: 2 μm.

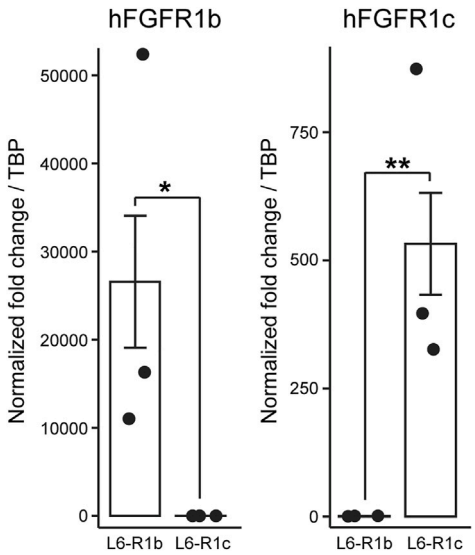

Figure S18. qPCR validation of FGFR isoform overexpression cell lines, related to Figure 4

Comparison of mRNA levels of hFGFR1 isoforms (left: b, right: c) in L6 rat myoblast cells stably transfected with hFGFR1b (L6-R1b) or hFGFR1c (L6-R1c) via RT-qPCR. Error bars represent SEM from three independent biological repeats.

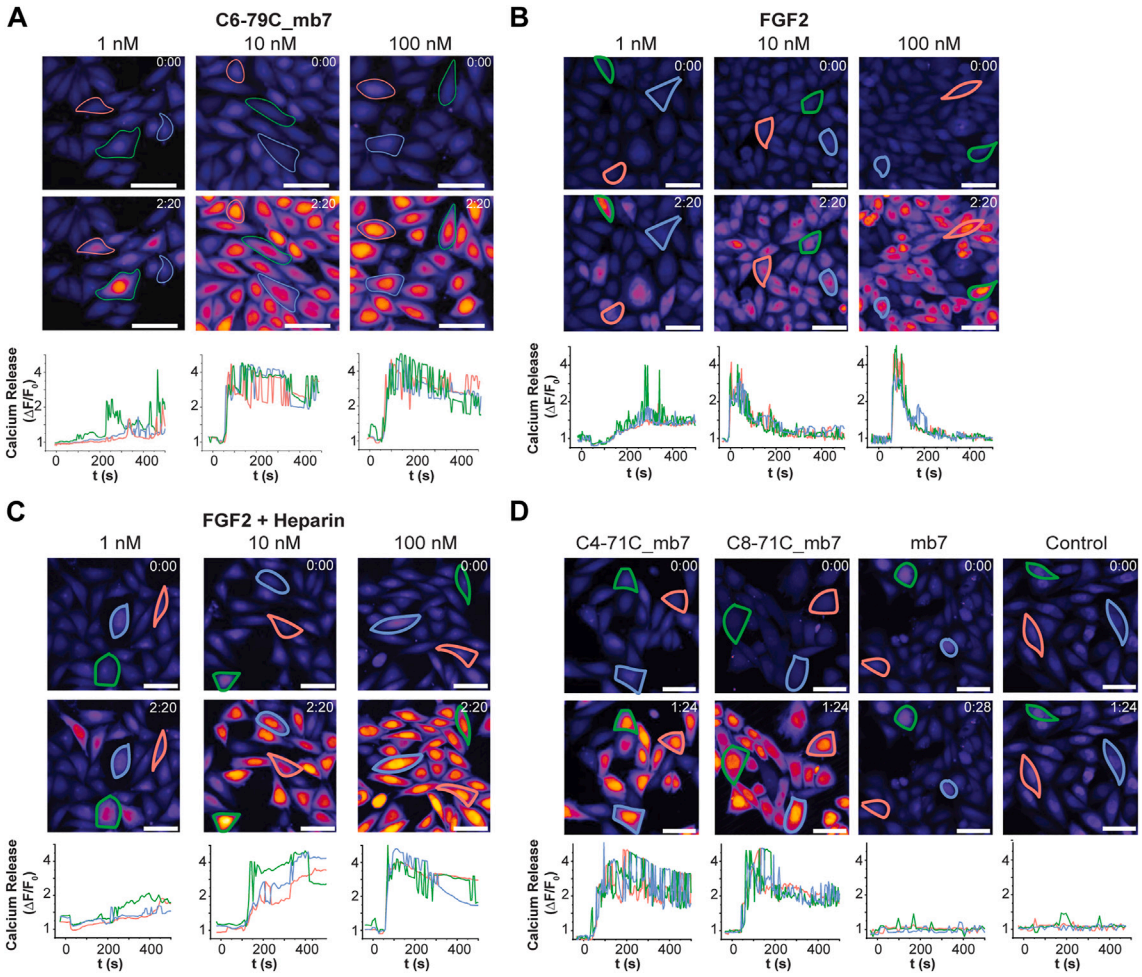

Figure S19. Calcium signaling stimulation, related to Figure 4

(A) Normalized single cell fluorescence intensity measurements for three randomly selected cells tracking calcium release in CHO-R1c cells following treatment with different concentrations of C6-79C_mb7. Images show two different time points. Selected cells are outlined and their fluorescence intensity is tracked underneath.

(B) Normalized single cell fluorescence intensity measurements for three randomly selected cells tracking calcium release in CHO-R1c cells following treatment with different concentrations of native FGF2. Images show two different time points. Selected cells are outlined and their fluorescence intensity is tracked underneath.

(C) Normalized single cell fluorescence intensity measurements for three randomly selected cells tracking calcium release in CHO-R1c cells following treatment with different concentrations of native FGF2, along with 40 μg/mL of heparan sulfate proteoglycans. Images show two different time points. Selected cells are outlined and their fluorescence intensity is tracked underneath.

(D) Normalized single cell fluorescence intensity measurements for three randomly selected cells tracking calcium release in CHO-R1c cells following treatment with 100 nM of C4-71C_mb7, C8-71C_mb7, and mb7 alone. Images show two different time points. Selected cells are outlined and their fluorescence intensity is tracked underneath. Scale bars: 66.3 μm in (A) and (C) and 50 μm in (B) and (D).

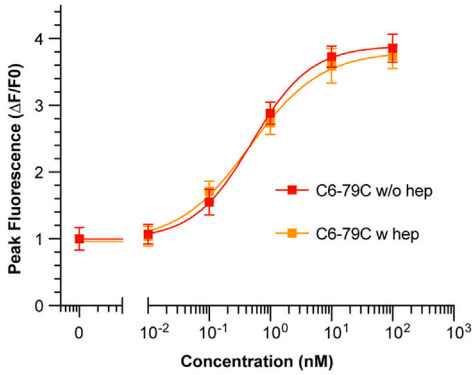

Figure S20. Heparin independent calcium signaling of C6-79C_mb7, related to Figure 4

Titration curve for C6-79C_mb7 with and without heparin shows heparin independent Ca^{2+} signaling of the designed agonist in CHO-R1c cells. 40 μg/mL heparin was supplemented in each condition.

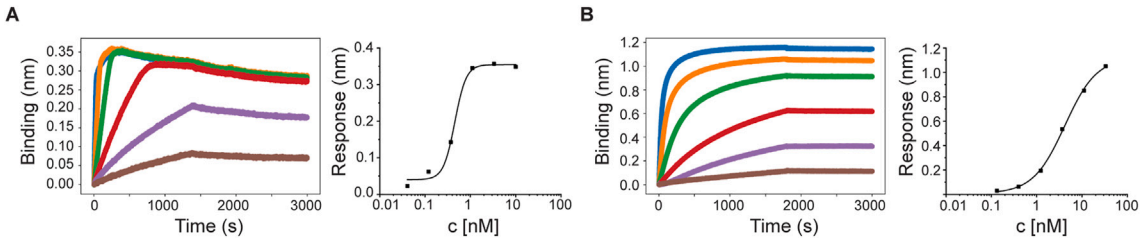

Figure S21. Biolayer-interferometry (BLI) analysis of mb7 and C6-79C_mb7, related to Figure 4

(A) mb7 binding titration with highest concentration of 10 nM and subsequent 3-fold dilution steps (blue: 10 nM, orange: 3.33 nM, green: 1.11 nM, red: 0.37 nM, purple: 0.12 nM, brown: 0.04 nM). Right: steady-state analysis yields a K_d of 453 pM.

(B) C6-79C_mb7 binding titration with highest concentration of 30 nM and 3-fold dilution steps (blue: 30 nM, orange: 10 nM, green: 3.33 nM, red: 1.11 nM, purple: 0.37 nM, brown: 0.12 nM). Right: steady-state analysis yields a K_d of 4.1 nM. Note that fusing the minibinder to the scaffold decreased binding affinity. We did not measure avidity effects with the low density of biotinylated receptors on the Octet tip.

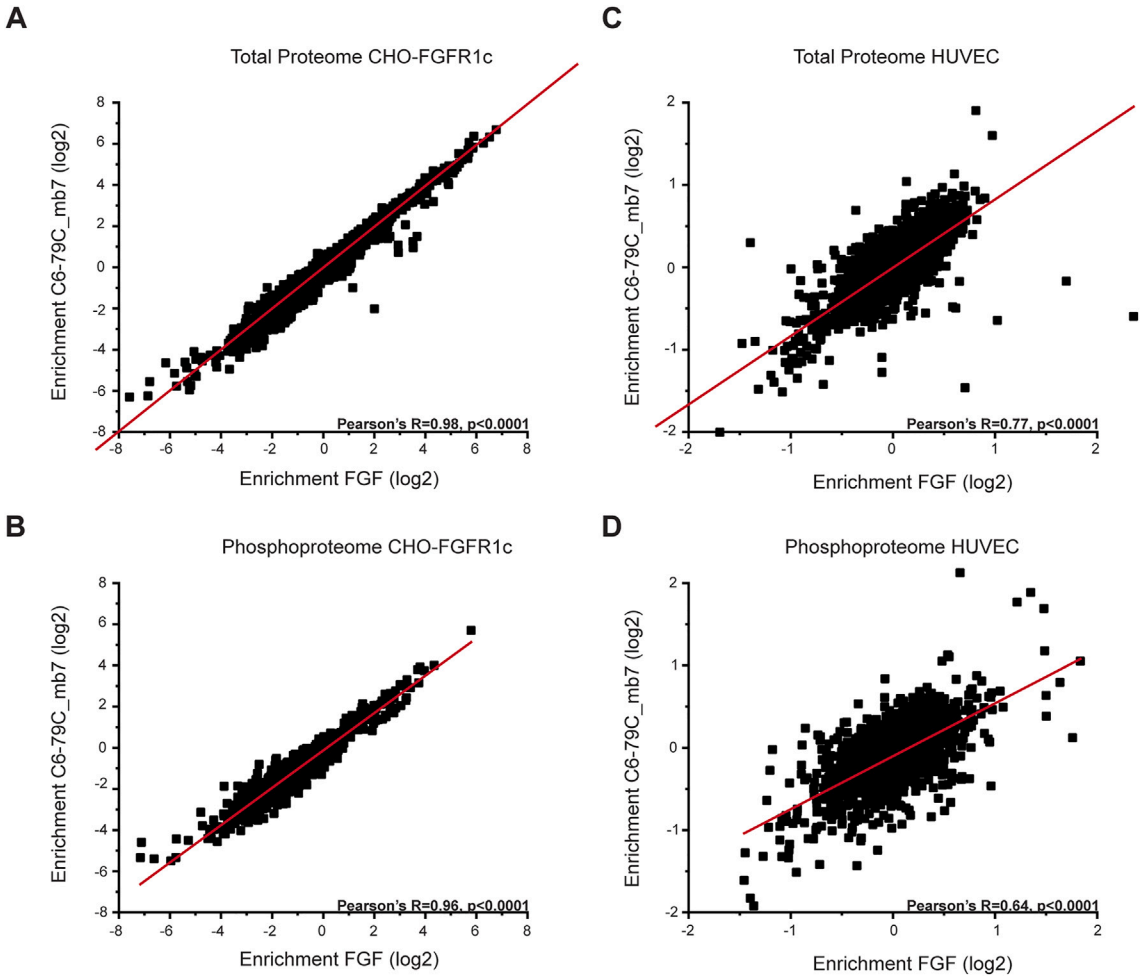

Figure S22. Proteomics analysis after treatment with C6-79C_mb7 agonist or FGF2 in hFGFR1c-expressing CHO and HUVEC cells, related to Figure 4

(A) Correlation of detected protein abundance normalized to control condition (untreated) in the total proteome between C6-79C_mb7 and FGF2 treatment at 100 nM in FGFR1c-expressing CHO cells.

(B) Correlation of detected phosphopeptide abundance normalized to control condition (untreated) in the phosphoproteome between C6-79C_mb7 and FGF2 treatment at 100 nM in FGFR1c-expressing CHO cells.

(C) Correlation of detected protein abundance normalized to control condition (untreated) in the total proteome between C6-79C_mb7 and FGF2 treatment at 100 nM in human umbilical vein endothelial cell (HUVEC) cells.

(D) Correlation of detected phosphopeptide abundance normalized to control condition (untreated) in the phosphoproteome between C6-79C_mb7 and FGF2 treatment at 100 nM in HUVEC cells.

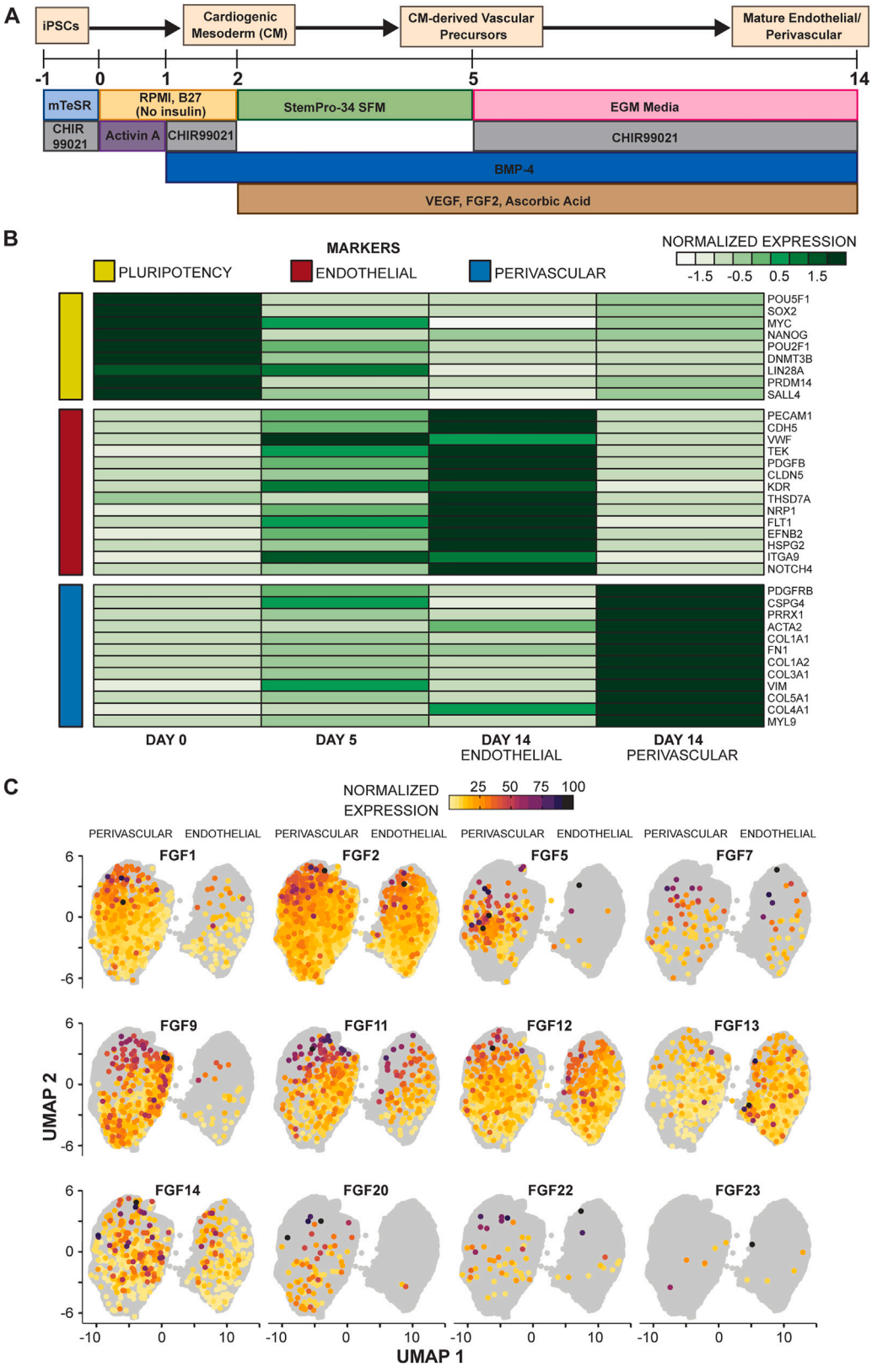

(legend on next page)

Figure S23. Vascular differentiation using designed agonists, related to Figure 5

(A) Schematic for endothelial cell differentiation from iPSCs through a cardiogenic mesoderm intermediate.

(B) Clustered heatmap comparing the normalized expression of selected putative cell markers (iPSCs, endothelial and perivascular) across all obtained clusters along with given annotations.

(C) Gene expression density plots of selected FGFs highlighting endogenous expression in both cell types obtained at day 14.

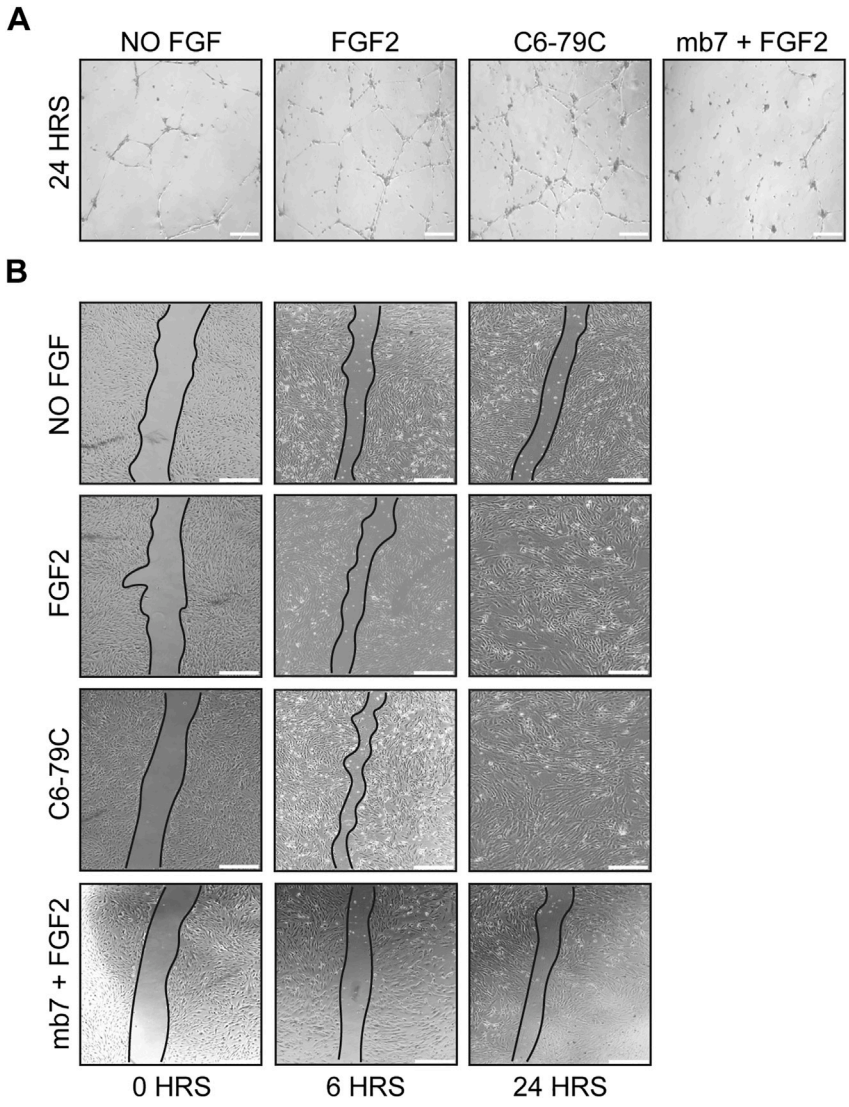

Figure S24. Tube formation and cell migration, related to Figure 5

(A) Representative images showing 2D network forming ability in 24 h of cells derived using No FGF, FGF2, C6-79C, or mb7 + FGF2. Scale bars: 100 μm.
(B) Representative images showing migratory capacity of cells derived using No FGF, FGF2, C6-79C, or mb7 + FGF2. Images are taken at 0, 6, and 24 h after inducing the scratch. Scale bars, 150 μm.

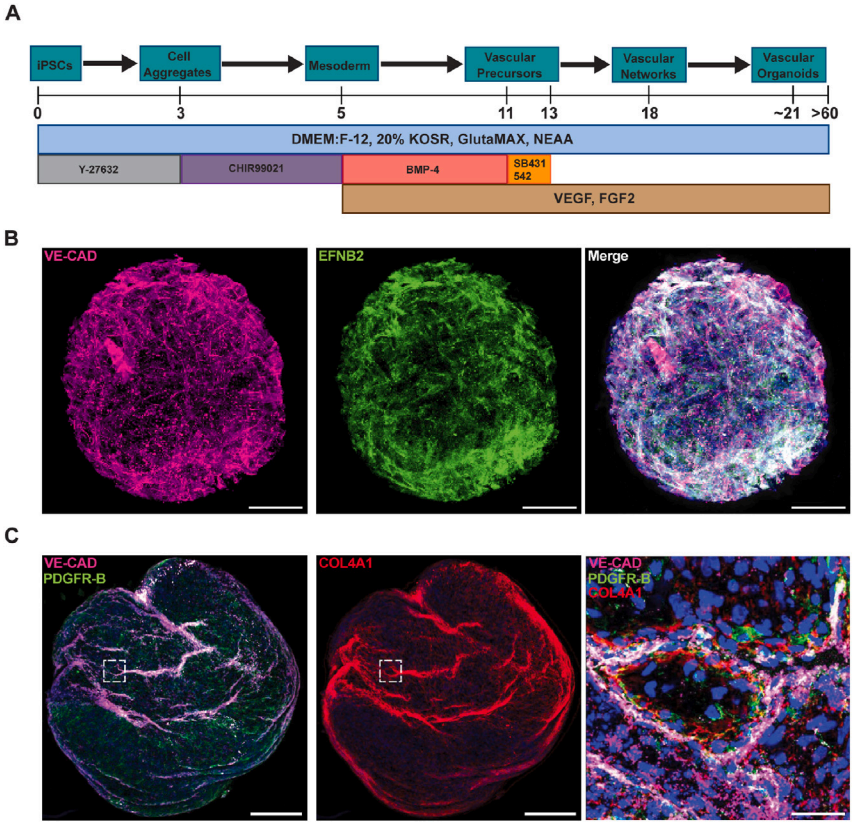

Figure S25. Blood vessel organoids using designed agonists, related to Figure 6

(A) Schematic for generation of 3D blood vessel organoids from iPSCs.

(B) Representative immunofluorescence images of blood vessel organoids generated using C6-79C_mb7. All endothelial cells are marked with VE-cadherin and arterial endothelial cells are marked with EFNB2. Scale bars: 200 μm.

(C) Representative immunofluorescence images of blood vessel organoids. PDGFR-B was used to mark perivascular cells, and COL4A1 was used to mark basement membrane structures. Zoomed image was generated by taking high magnification images of the organoid and then using Imaris software to create a 3D rendering of the organoids and performing orthogonal slicing to clearly separate regions with microvessels, which are obscured in max intensity projections of the whole organoid at high magnification. Scale bars: 200 μm (whole) and 50 μm (inset).

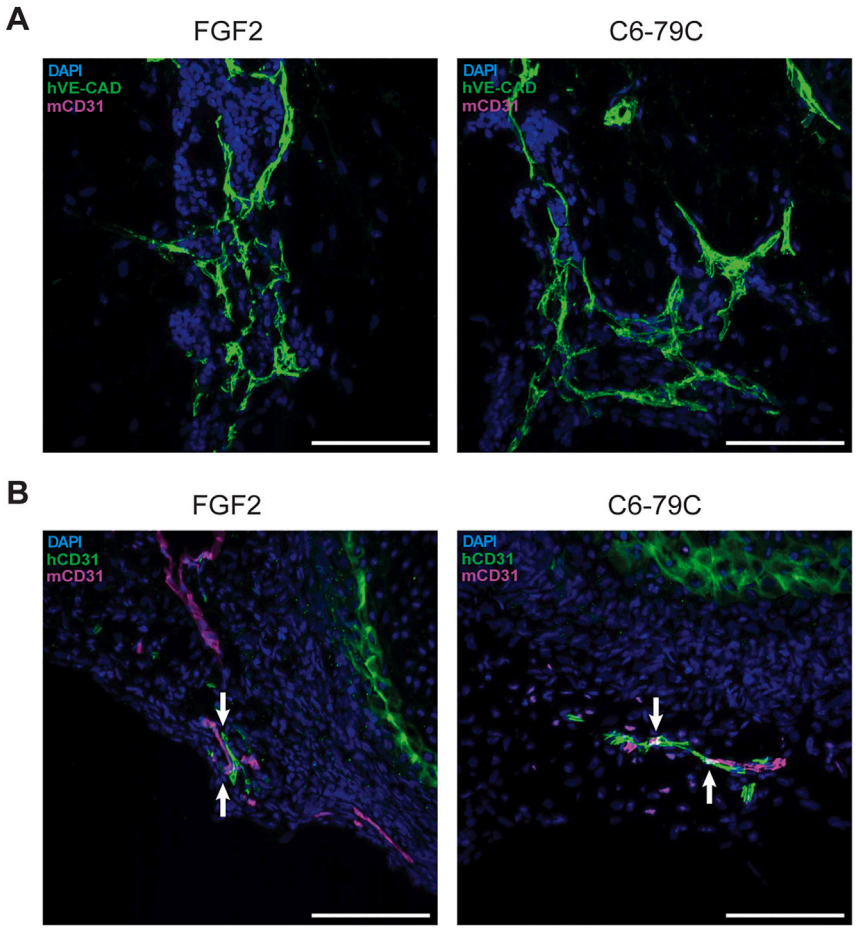

Figure S26. Vascular network formation in immunodeficient mice, related to Figure 6

(A) Immunohistochemical characterization of human (hVE-cadherin+) vascular networks following BVO transplantation under the mouse kidney.

(B) Immunohistochemical characterization of human (hCD31+) vascular outgrowths forming connections with mouse (mCD31+) vascular cells. Scale bars, 100 μm.

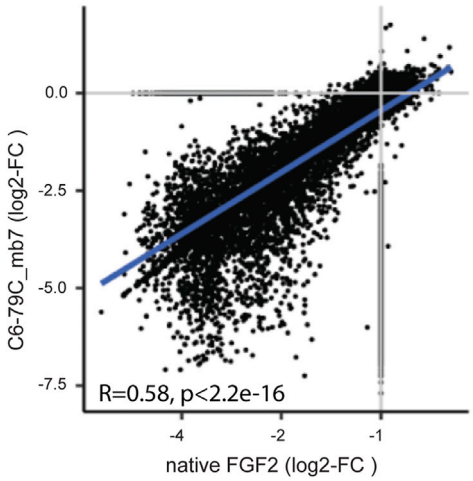

Figure S27. Bulk transcriptomics using designed agonists, related to STAR Methods

Correlation between differentially expressed genes (DEGs) in HUVEC cells treated with either native FGF2 or C6-79C_mb7.